

University of Windsor

## Scholarship at UWindor

---

Electronic Theses and Dissertations

Theses, Dissertations, and Major Papers

---

2019

### Plasma-Assisted Electrolytic Deposition for Synthesizing Porous Flexible Binder-Free Anodes of High-Electrochemical Performance Lithium-Ion Batteries

Tao Li

*University of Windsor*

Follow this and additional works at: <https://scholar.uwindsor.ca/etd>

---

#### Recommended Citation

Li, Tao, "Plasma-Assisted Electrolytic Deposition for Synthesizing Porous Flexible Binder-Free Anodes of High-Electrochemical Performance Lithium-Ion Batteries" (2019). *Electronic Theses and Dissertations*. 7717.

<https://scholar.uwindsor.ca/etd/7717>

This online database contains the full-text of PhD dissertations and Masters' theses of University of Windsor students from 1954 forward. These documents are made available for personal study and research purposes only, in accordance with the Canadian Copyright Act and the Creative Commons license—CC BY-NC-ND (Attribution, Non-Commercial, No Derivative Works). Under this license, works must always be attributed to the copyright holder (original author), cannot be used for any commercial purposes, and may not be altered. Any other use would require the permission of the copyright holder. Students may inquire about withdrawing their dissertation and/or thesis from this database. For additional inquiries, please contact the repository administrator via email ([scholarship@uwindsor.ca](mailto:scholarship@uwindsor.ca)) or by telephone at 519-253-3000ext. 3208.

**Plasma-Assisted Electrolytic Deposition for Synthesizing Porous Flexible Binder-Free Anodes of High-Electrochemical Performance Lithium-Ion Batteries**

By

**Tao Li**

A Thesis  
Submitted to the Faculty of Graduate Studies  
Through the Department of Mechanical, Automotive & Materials Engineering  
In Partial Fulfillment of the Requirements for  
The Degree of Master of Applied Science  
At the University of Windsor

Windsor, Ontario, Canada

2019

© 2019 Tao Li

**Plasma-Assisted Electrolytic Deposition for Synthesizing Porous Flexible Binder-Free Anodes of High-Electrochemical Performance Lithium-Ion Batteries**

by

**Tao Li**

APPROVED BY:

---

J. Wang

Department of Chemistry & Biochemistry

---

H. Hu

Department of Mechanical, Automotive & Materials Engineering

---

X. Nie, Advisor

Department of Mechanical, Automotive & Materials Engineering

April 5, 2019

## DECLARATION OF CO-AUTHORSHIP/PREVIOUS PUBLICATION

### I. Co-Authorship

I hereby certify that this thesis incorporates material that is result of joint research, as follows: Chapter 5 of the thesis was co-authored with Ran Cai and Jimi Tjong under the supervision of Prof. Xueyuan Nie. In all cases, the key ideas, primary contributions, experimental designs, data analysis, interpretation, and writing were performed by me. In Chapter 5, Ran Cai provided helps on experimental section, and Jimi Tjong was involved as an industrial collaborator.

I am aware of the University of Windsor Senate Policy on Authorship and I certify that I have properly acknowledged the contribution of other researchers to my thesis, and have obtained written permission from each of the co-authors to include the above materials in my thesis.

I certify that, with above qualification, this thesis and the research to which it refers, is the product of my own work.

### II. Previous Publication

This thesis includes 2 original papers that have been previously published for publication in peer reviewed journals, as follows:

Thesis Chapter	Publications tile/full citation	Publication status
Chapter 4	<b>Tao Li</b> , and Xueyuan Nie. One-Step Fast-Synthesized Foamlike Amorphous $\text{Co}(\text{OH})_2$ Flexible Film on Ti Foil by Plasma-Assisted Electrolytic Deposition as a Binder-Free Anode of a High-Capacity Lithium-Ion Battery. <i>ACS appl. mater. interfaces</i> 10 (2018): 16943-16946.	Published
Chapter 5	<b>Tao Li</b> , Ran Cai, Xueyuan Nie, and Jimi Tjong. Porous $\text{Ni}_3(\text{PO}_4)_2$ thin film as a binder-free and low-cost anode of a high-capacity lithium-ion battery. <i>J. Electroanal.</i>	Published

	<i>Chem.</i> 835 (2019): 81-85	
--	--------------------------------	--

I certify that I have obtained a written permission from the copyright owners to include the above published materials in my thesis. I certify that the above materials describe work completed during my registration as a graduate student at the University of Windsor.

### III. General

I certify that, to the best of my knowledge, my thesis does not infringe upon anyone's copyright nor violate any proprietary rights and that any ideas, techniques, quotations, or any other material from the work of other people included in my thesis, published or otherwise, are fully acknowledged in accordance with the standard referencing practices. Furthermore, to the extent that I have included copyrighted material that surpasses the bounds of fair dealing within the meaning of the Canada Copyright Act, I certify that I have obtained a written permission from the copyright owner(s) to include such material(s) in my thesis and have included copies of such copyright clearances to my appendix.

I declare that this is a true copy of my thesis, including any final revisions, as approved by my thesis committee and the Graduate Studies office, and that this thesis has not been submitted for a higher degree to any other University or Institution.

## ABSTRACT

In this study, plasma-assisted electrolytic deposition was innovatively applied to rapid construction of binder-free amorphous  $\text{Co}(\text{OH})_2$  and  $\text{Ni}_3(\text{PO}_4)_2$  thin film anodes on Ti for lithium-ion batteries. In the electrochemical testing, both materials showed high-capacity. However, compared with amorphous  $\text{Co}(\text{OH})_2$  coating, the amorphous  $\text{Ni}_3(\text{PO}_4)_2$  coating has the better stability and the lower thickness, which is more hopeful for industrial application. Therefore, it is necessary to further study on  $\text{Ni}_3(\text{PO}_4)_2$  anode. In comparative electrochemical study between the amorphous and crystalline  $\text{Ni}_3(\text{PO}_4)_2$ , the amorphous  $\text{Ni}_3(\text{PO}_4)_2$  showed a lower degradation rate on capacity, while the crystalline one had a higher capacity in the initial several cycles. Nevertheless, both amorphous and crystalline  $\text{Ni}_3(\text{PO}_4)_2$  shows high capacity during cycling due to the high porosity of the films. To further improve the electrochemical performance of amorphous  $\text{Ni}_3(\text{PO}_4)_2$  anodes in lithium-ion batteries, some possible surface modification methods including the Co-doping, sputtering Au coating and carbon coating were explored. The results indicated that the sputtering Au coating and sputtering carbon coating could be the better ways to improve the cycling stability and capacity of amorphous  $\text{Ni}_3(\text{PO}_4)_2$  anodes.

## DEDICATION

To My Fiancée,

Ruixue Dai, *The Hospital for Sick Children, Toronto, Canada*

To My Parents,

Ping Dong and Shuzhong Li (Emeritus), *Sinopec Group, Beijing, China*

For their endless love and devotion

## ACKNOWLEDGEMENTS

Special thanks go to Dr. Xueyuan Nie, for providing me with the opportunity to work on this project under his distinguished supervision. I am grateful to him for his great encouragement and endless support for the research.

I would like to thank the members of my committee Dr. Jichang Wang and Dr. Henry Hu for their invaluable discussions, suggestions and time that helped to improve the final copy of this thesis. I would also like to acknowledge Dr. Tricia Breen Carmichael, Dr. S. Holger Eichhorn and Miss. Yunyun Wu for access to battery packaging and XRD testing.

Sincere thanks are extended to the group members, Mr. Chen Zhao, Mr. Wei Zha and Miss. Ran Cai for their help and advice.



## TABLE OF CONTENTS

DECLARATION OF CO-AUTHORSHIP/PREVIOUS PUBLICATION .....	iii
ABSTRACT.....	v
DEDICATION .....	vi
ACKNOWLEDGEMENTS .....	vii
LIST OF FIGURES .....	xii
LIST OF ABBREVIATIONS/SYMBOLS.....	xvii
CHAPTER 1 Introduction.....	1
<i>1.1 Motivation .....</i>	<i>1</i>
<i>1.2 Objectives of this study.....</i>	<i>4</i>
<i>1.3 Organization of the Thesis .....</i>	<i>5</i>
REFERENCES .....	6
CHAPTER 2 Literature Review on Materials and Surface Coating Technologies for Lithium-Ion Batteries .....	8
<i>2.1 Cathode materials of lithium-ion batteries .....</i>	<i>8</i>
<i>2.1.1 LiCoO<sub>2</sub> cathode .....</i>	<i>8</i>
<i>2.1.2 LiMn<sub>2</sub>O<sub>4</sub> cathode .....</i>	<i>9</i>
<i>2.1.3 LiFePO<sub>4</sub> cathode .....</i>	<i>10</i>
<i>2.2 Anode materials of lithium-ion batteries.....</i>	<i>10</i>
<i>2.2.1 Traditional anode materials .....</i>	<i>11</i>
<i>2.2.2 Alloy anode materials .....</i>	<i>12</i>
<i>2.2.3 Nano-sized transition-metal oxides anode materials .....</i>	<i>13</i>
<i>2.2.4 Graphene and carbon nanotubes anode materials.....</i>	<i>14</i>
<i>2.2.5 Metal hydroxide anode materials .....</i>	<i>16</i>
<i>2.2.6 Oxometallate anode materials.....</i>	<i>17</i>
<i>2.3 Surface coating technologies for binder-free anodes of lithium-ion batteries.....</i>	<i>18</i>

2.3.1 Physical vapor deposition (PVD) .....	18
2.3.2 Chemical vapor deposition (CVD) .....	20
2.3.3 Plasma electrolytic oxidation (PEO).....	22
2.3.4 Electrochemical anodization .....	24
REFERENCES .....	26
CHAPTER 3 Experimental Details .....	28
3.1 Preparation of binder-free anode .....	28
3.2 Characterization of structure and morphology.....	30
3.3 Battery packaging .....	31
3.4 Battery testing .....	33
3.5 Sputtering coating .....	37
3.6 Preparation of metallographic specimens .....	37
CHAPTER 4 One Step Fast Synthesized Foam-like Amorphous $\text{Co}(\text{OH})_2$ Flexible Film on Ti Foil by Plasma Assisted Electrolytic Deposition as a Binder-free Anode of High Capacity Lithium Ion Battery .....	39
4.1 Introduction .....	39
4.2 Experimental section .....	40
4.2.1 Synthesis of amorphous $\text{Co}(\text{OH})_2$ on Ti foil .....	40
4.2.2 Structural Characterization.....	41
4.2.3 Electrochemical Measurements.....	41
4.3 Results and discussions .....	42
4.4 Conclusions .....	47
REFERENCES .....	48
SUPPORTING INFORMATION .....	52
CHAPTER 5 Porous $\text{Ni}_3(\text{PO}_4)_2$ Thin Film as a Binder-free and Low-cost Anode of a High-capacity Lithium-ion Battery .....	53
5.1 Introduction .....	53
5.2 Experimental .....	54
5.2.1 Synthesis of $\text{Ni}_3(\text{PO}_4)_2$ on Ti Foil .....	54
5.2.2 Structural Characterization.....	55

5.2.3 Preparation of coin cell .....	55
5.2.4 Electrochemical testing .....	55
5.3 Results and discussion .....	56
5.4 Conclusion .....	61
REFERENCES .....	63
SUPPORTING INFORMATION .....	66
CHAPTER 6 Plasma-Assisted Electrolytic Deposition Synthesized Porous Ni <sub>3</sub> (PO <sub>4</sub> ) <sub>2</sub> Thin Film: A Comparative Study of Amorphous and Crystalline Ni <sub>3</sub> (PO <sub>4</sub> ) <sub>2</sub> Binder-Free Anodes in Lithium-Ion Batteries .....	67
6.1 Introduction .....	67
6.2 Experimental section .....	68
6.2.1 Preparation of Ni <sub>3</sub> (PO <sub>4</sub> ) <sub>2</sub> on Ti .....	68
6.2.2 Materials characterization .....	69
6.2.3 Electrochemical measurements .....	69
6.3 Results and Discussion .....	69
6.4 Conclusions .....	78
REFERENCES .....	80
SUPPORTING INFORMATION .....	84
CHAPTER 7 Possible Methods to Improve the Electrochemical Performance of Amorphous Ni <sub>3</sub> (PO <sub>4</sub> ) <sub>2</sub> Anode in Lithium-Ion Battery .....	86
7.1 Introduction .....	86
7.2 Experimental Section .....	86
7.2.1 Co-doped Ni <sub>3</sub> (PO <sub>4</sub> ) <sub>2</sub> .....	86
7.2.2 Sputtering Au coated Ni <sub>3</sub> (PO <sub>4</sub> ) <sub>2</sub> .....	87
7.2.3 Dip carbon nanofibers coated Ni <sub>3</sub> (PO <sub>4</sub> ) <sub>2</sub> .....	87
7.2.4 Sputtering carbon coated Ni <sub>3</sub> (PO <sub>4</sub> ) <sub>2</sub> .....	87
7.2.5 Materials characterization .....	87
7.2.6 Electrochemical measurement .....	87
7.3 Results and Discussion .....	88
7.3.1 Co-doped Ni <sub>3</sub> (PO <sub>4</sub> ) <sub>2</sub> .....	88

7.3.2 Sputtering Au coated $Ni_3(PO_4)_2$ .....	90
7.3.3 Dip carbon nanofibers coated $Ni_3(PO_4)_2$ .....	92
7.3.4 Sputtering carbon coated $Ni_3(PO_4)_2$ .....	94
7.4 Conclusions .....	96
REFERENCES .....	97
CHAPTER 8 Conclusions and Future Work .....	98
APPENDICES .....	102
Appendix A .....	102
VITA AUCTORIS .....	104

## LIST OF FIGURES

Figure 1-1. The operation principle of the lithium-ion battery.....	1
Figure 1-2. Some examples of materials in lithium-ion batteries.....	2
Figure 1-3. Growth process of PEO coating on Mg substrate.....	4
Figure 2-1. The cycling performance of $\text{LiCoO}_2$ and $\text{Al}_2\text{O}_3/\text{LiCoO}_2$ cathodes in lithium-ion batteries.....	8
Figure 2-2. The cycling performance of $\text{LiMn}_2\text{O}_4$ (a) and $\text{LiCo}_{0.1}\text{Mn}_{1.9}\text{O}_4$ (b) cathodes in lithium-ion batteries.....	9
Figure 2-3. The cycling performance of $\text{LiFePO}_4$ (a) and $\text{ZrO}_2/\text{LiFePO}_4$ (b) cathodes in lithium-ion batteries.....	10
Figure 2-4. Cycling performance of natural graphite anode (d,e and f).....	11
Figure 2-5. Cycling performance of silicon film anode.....	12
Figure 2-6. Comparison of cycle performance for Sb, Sb/carbon and Sb/carbon/graphite nanocomposites.....	13
Figure 2-7. Capacity of nano-sized transition-metal oxides anode materials.....	14
Figure 2-8. Reversible capacity of CNTs, Sb, $\text{SnSb}_{0.5}$ , CNTs–Sb and CNTs– $\text{SnSb}_{0.5}$ .....	15
Figure 2-9. Comparison of the cycling performance of graphene, $\text{Co}_3\text{O}_4$ , and the $\text{Co}_3\text{O}_4$ /graphene composite.....	16
Figure 2-10. Cycling performance of $\text{Ni}(\text{OH})_2$ and the $\text{Ni}(\text{OH})_2/\text{GO}$ composite...	17
Figure 2-11. Cycling performance of $\text{Co}_2\text{TiO}_4$ and the $\text{Co}_2\text{TiO}_4@\text{C}$ composite...	18
Figure 2-12. preparation method of $\text{Sn}/\text{SnO}_2/\text{MWCNT}$ composites.....	19

Figure 2-13. Specific discharge capacities with cycle number of electrodes.....	20
Figure 2-14. The synthetic process and morphology of Si anode.....	21
Figure 2-15. Reversible discharge capacity and columbic efficiency of the hollow Si spheres anode in comparison with the theoretical capacity of graphite.....	22
Figure 2-16. The morphology of PEO SiO <sub>2</sub> /TiO <sub>2</sub> composite coating.....	23
Figure 2-17. Cycling performance of PEO SiO <sub>2</sub> /TiO <sub>2</sub> anode and other types of TiO <sub>2</sub> anodes in lithium ion batteries.....	23
Figure 2-18. Morphology of TiO <sub>2</sub> nanotubes: (e) on Ti foam; (f) on Ti foil.....	24
Figure 2-19. Cycling performance of TiO <sub>2</sub> nanotubes on Ti substrates anodes in lithium ion batteries.....	25
Figure 3-1. The fixture for single side protection.....	28
Figure 3-2. Schematic drawing of instrument.....	29
Figure 3-3. Vacuum Oven.....	29
Figure 3-4. XRD.....	30
Figure 3-5. SEM and EDS attachments.....	31
Figure 3-6. Cutter and coin cell sealer.....	32
Figure 3-7. All parts in coin cell.....	32
Figure 3-8. Argon gas glove box.....	33
Figure 3-9. LAND Battery Testing System CT2001A.....	34
Figure 3-10. Parameters of cycling performance test.....	34
Figure 3-11. Parameters of rate capability test.....	35
Figure 3-12. Bio-logic electrochemical work-station.....	36

Figure 3-13. Parameters of CV test.....	36
Figure 3-14. Sputtering coater.....	37
Figure 3-15. Microscopy.....	38
Figure 4-1. Schematic illustration of experimental process (a-c), growth of Co(OH) <sub>2</sub> on Ti foil by plasma assisted electrolytic deposition (b <sub>1</sub> -b <sub>3</sub> ).....	40
Figure 4-2. (a) XRD pattern, XPS spectra of (b) Co 2p and (c) O 1s, (d) expanded Co 2p spectrum.....	43
Figure 4-3. The surface SEM images of Co(OH) <sub>2</sub> on Ti substrate, (a-b) surface structure, (c) cross sectional structure and (d) surface structure after 50 charging-discharging process.....	44
Figure 4-4. Electrochemical testing of Co(OH) <sub>2</sub> anode in lithium ion battery, (a) cycling performance (0-3V, 400 $\mu$ A/cm <sup>2</sup> ), (b) galvanostatic cycling profiles (0-3V, 400 $\mu$ A/cm <sup>2</sup> ), (c) rate capability and (d) cyclic voltammetry (0.1mV/s).....	45
Figure S4-1. The SEM images of Co(OH) <sub>2</sub> on Ti substrate (a) surface and (b) cross sectional structure, and corresponding porosity analysis (insert a and b).....	52
Figure 5-1. (a-d) PAED process of formation of Ni <sub>3</sub> (PO <sub>4</sub> ) <sub>2</sub> thin film on Ti Foil...	56
Figure 5-2. (a) X-ray diffraction pattern. (b-d) XPS spectra of (b) Ni2p, (c) P2p and (d) O1s.....	57
Figure 5-3. (a) Flexible Ni <sub>3</sub> (PO <sub>4</sub> ) <sub>2</sub> thin film photo. (b-d) SEM images of (b) surface morphology, (c) cross-sectional structure and (d) magnification of surface morphology.....	58
Figure 5-4. Electrochemical testing of the Ni <sub>3</sub> (PO <sub>4</sub> ) <sub>2</sub> anode in the LIB: (a) cycling performance and coulombic efficiency (0-3V, 400 $\mu$ A/cm <sup>2</sup> ); (b) galvanostatic cycling profiles (0-3V, 400 $\mu$ A/cm <sup>2</sup> ); (c) rate capability (0-3V); (d) CV (0.1 mV/s).....	59

Fig. S5-1. Porosity of porous $\text{Ni}_3(\text{PO}_4)_2$ thin film.....	66
Fig. S5-2. The surface morphology of $\text{Ni}_3(\text{PO}_4)_2$ electrode after 50 cycles.....	66
Figure 6-1. (a-d) PAED growth process of amorphous porous $\text{Ni}_3(\text{PO}_4)_2$ thin film on Ti foil.....	69
Figure 6-2. XRD pattern of (a) amorphous $\text{Ni}_3(\text{PO}_4)_2$ and (b) crystalline $\text{Ni}_3(\text{PO}_4)_2$ .....	70
Figure 6-3. SEM images of $\text{Ni}_3(\text{PO}_4)_2$ coatings: surface morphologies of (a-c) amorphous $\text{Ni}_3(\text{PO}_4)_2$ coating and (d-f) crystalline $\text{Ni}_3(\text{PO}_4)_2$ coating.....	71
Figure 6-4. SEM images of $\text{Ni}_3(\text{PO}_4)_2$ coatings: (a) cross-sectional morphologies of amorphous $\text{Ni}_3(\text{PO}_4)_2$ coating and (b) crystalline $\text{Ni}_3(\text{PO}_4)_2$ coating.....	72
Figure 6-5. Electrochemical testing of the $\text{Ni}_3(\text{PO}_4)_2$ anode in the LIB: (a) cycling performance (0-3V, 400 $\mu\text{A}/\text{cm}^2$ ) of amorphous $\text{Ni}_3(\text{PO}_4)_2$ anode; (b) cycling performance (0-3V, 400 $\mu\text{A}/\text{cm}^2$ ) of crystalline $\text{Ni}_3(\text{PO}_4)_2$ anode; (c) comparison of discharge capacity of amorphous and crystalline $\text{Ni}_3(\text{PO}_4)_2$ anodes (0-3V, 400 $\mu\text{A}/\text{cm}^2$ ); (d) comparison of rate capability of amorphous and crystalline $\text{Ni}_3(\text{PO}_4)_2$ anode (0-3V).....	73
Figure 6-6. SEM images of $\text{Ni}_3(\text{PO}_4)_2$ coatings after 70 cycles: surface morphologies of (a-b) amorphous $\text{Ni}_3(\text{PO}_4)_2$ coating and (c-d) crystalline $\text{Ni}_3(\text{PO}_4)_2$ coating.....	75
Figure 6-7. Cyclic Voltammetry (CV) (0.1mV/s) and derivative plot of 4th scanning: (a-c) amorphous $\text{Ni}_3(\text{PO}_4)_2$ ; (d-f) crystalline $\text{Ni}_3(\text{PO}_4)_2$ .....	77
Figure S6-1. Photo of as prepared $\text{Ni}_3(\text{PO}_4)_2$ anode.....	84
Figure S6-2. XPS spectra of amorphous $\text{Ni}_3(\text{PO}_4)_2$ (b) $\text{Ni}2\text{p}$ , (c) $\text{P}2\text{p}$ and (d) $\text{O}1\text{s}$ .....	84
Figure S6-3. EIS of amorphous and crystalline $\text{Ni}_3(\text{PO}_4)_2$ anodes in lithium-ion batteries.....	85



Figure S6-4. Metallography of Ti foil before (a) and after (b) annealing.....	85
Figure 7-1. SEM characterization of Co-doped $\text{Ni}_3(\text{PO}_4)_2$ : (a) elements mapping; (b) surface morphology; (c) EDS.....	88
Figure 7-2. Cycling performance of Co-doped $\text{Ni}_3(\text{PO}_4)_2$ anode.....	89
Figure 7-3. SEM characterization of $\text{Au}/\text{Ni}_3(\text{PO}_4)_2$ : (a) elements mapping; (b) surface morphology; (c) EDS.....	90
Figure 7-4. (a)Cycling performance of $\text{Au}/\text{Ni}_3(\text{PO}_4)_2$ and $\text{Ni}_3(\text{PO}_4)_2$ ; (b) Surface morphology of $\text{Au}/\text{Ni}_3(\text{PO}_4)_2$ after 50 cycles.....	91
Figure 7-5. SEM characterization of carbon nanofiber/ $\text{Ni}_3(\text{PO}_4)_2$ : (a) elements mapping; (b) surface morphology; (c) cross-section; (d) EDS.....	92
Figure 7-6. Cycling performance of carbon nanofibers/ $\text{Ni}_3(\text{PO}_4)_2$ and $\text{Ni}_3(\text{PO}_4)_2$ ..	93
Figure 7-7. SEM characterization of $\text{C}/\text{Ni}_3(\text{PO}_4)_2$ : (a) elements mapping; (b) surface morphology; (c) EDS.....	94
Figure 7-8. (a) Cycling performance of $\text{C}/\text{Ni}_3(\text{PO}_4)_2$ and $\text{Ni}_3(\text{PO}_4)_2$ ; (b) Surface morphology of $\text{C}/\text{Ni}_3(\text{PO}_4)_2$ after 50 cycles.....	95

## LIST OF ABBREVIATIONS/SYMBOLS

LIB	Lithium-ion battery
PEO	Plasma electrolytic oxidation
PED	Plasma electrolytic deposition
PAED	Plasma assisted-electrolytic deposition
CNT	Carbon nanotube
MWCNT	Multiple walls carbon nanotubes
PVD	Physical vapor deposition
CVD	Chemical vapor deposition
SEM	Scanning electronic microscopy
EDS	Energy-dispersive X-ray spectroscopy
XRD	X-ray diffraction
XPS	X-ray photoelectron spectroscopy
CV	Cyclic voltammetry
EIS	Electrochemical impedance spectroscopy
SEI	Solid electrolytic interface
aq	Aqueous solution
g	Gas
s	Solid
vs	Versus

D	Diameter
PVDF	Polyvinylidene fluoride
NMP	N-Methyl-2-pyrrolidone
GO	Graphene Oxide
PP	Polypropylene
PE	Polyethylene
PS	Polystyrene

## CHAPTER 1

### Introduction

#### *1.1 Motivation*

Recently, along with reduction of fossil fuel and aggravation of air pollutions, scientists tried to find a new environmentally-friendly energy conversion system with low-consumption of natural resource to ensure the sustainable development. The lithium-ion battery (LIB) as an energy storage device which matches these requirements was wildly researched.

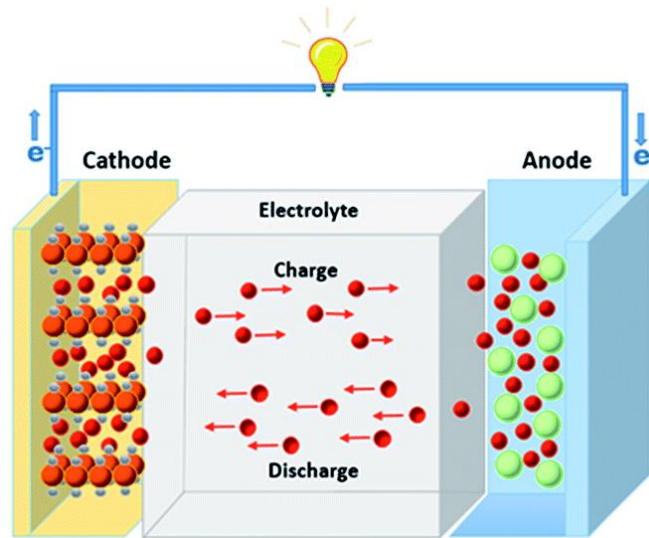


Figure 1-1. The operation principle of the lithium-ion battery.[1]

The working principle of lithium-ion battery has been illustrated in Figure 1-1. The lithium ion battery was mainly composed by the cathode, electrolyte and anode. In the charge process, the lithium ions leave the cathode materials and insert into the anode materials via the electrolyte. In the discharge process, the lithium ions extract from anode and return to the cathode. At the same time, the lithium-ion battery provides electrons to the external circuits.

For the cathode materials, the types of materials are limited. The research and applications of LIB cathodes mainly focus on lithium oxometallate materials such as the  $\text{LiCoO}_2$ ,  $\text{LiMn}_2\text{O}_4$  and  $\text{LiFeO}_4$ . [2-4] For the anode materials, there has a lot of choices of material including the carbon, silicon, metal-oxides, metal hydroxides and alloy. [5-9] Some examples of materials for lithium-ion batteries have been listed in Figure 1-2.

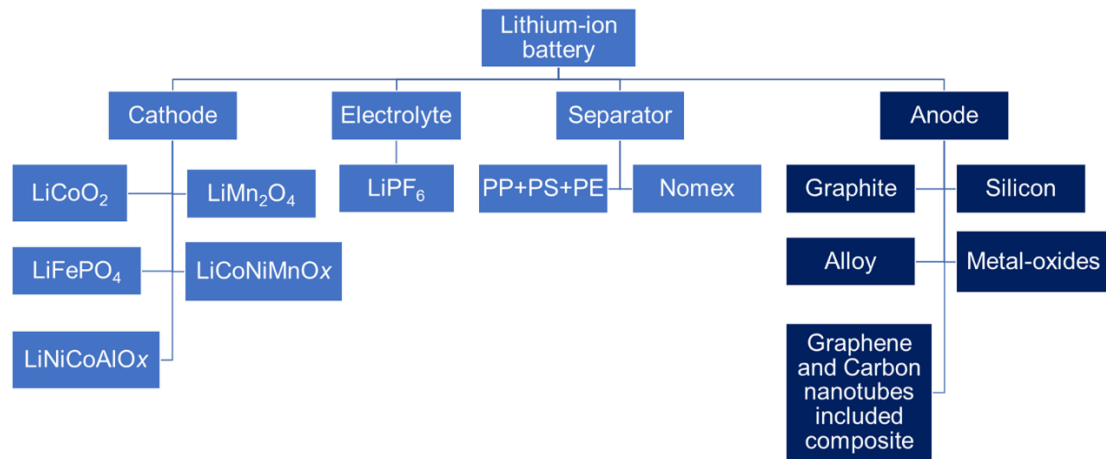


Figure 1-2. Some examples of materials in lithium-ion batteries.

Currently, due to the improvement of chemical research and manufacture technology, lithium-ion batteries have been successfully applied on portable devices such as laptops, mobile phones and watches. Along with the high consumption of petroleum resource, the automobile industry also needed to develop a new power system to replace the traditional motor engines. Lithium-ion battery was recognized as one of the best choices for the new power system. The hybrid and full electric vehicles were started to use lithium-ion battery as the power source. Therefore, the study on high-capacity and low-cost lithium-ion battery is necessary.

Like the information has been mentioned above, the types of cathode materials are

limited, and the theoretical capacity of current cathode materials is very low. It is hopeless to obviously improve the capacity of lithium-ion battery by exploring the cathode materials. Contrarily, there are many types of candidates for anode materials with high theoretical capacity. So, the researchers tend to use new different types of anode materials to replace the traditional anode materials such as graphite and silicon.[10] Most current studies emphasize the nano-sized anode materials for lithium-ion batteries. However, nano-sized materials need a long-time and high-cost manufacture process. Furthermore, nano-sized or powder anode materials need a complex process in electrode fabrication including mixing binder, adding conductive carbon, stirring, coating and drying, which lead to the high cost on lithium-ion batteries. Existence of binder in nano-powder containing anodes also injures the electrochemical performance of lithium-ion battery during cycling.[11] Therefore, it is significant to find a technology to rapid fabricate the low-cost and binder-free anodes of the high-capacity lithium-ion batteries.

Plasma electrolytic oxidation (PEO) was a technology that a porous oxide ceramic coating was deposited on the substrate surface with the help of plasma discharges in the electrolyte. The growth mechanism of PEO coating on Mg substrate has been illustrated in Figure 1-3.[12] The PEO has been widely applied on wearing-resistance and corrosion protection of Mg, Al and Ti alloys,[13] but rarely considered as the fabrication technology for battery electrode. Therefore, in this study, to rapid fabricate the binder-free anode as well as to extend the applications of PEO, the plasma-assisted electrolytic deposition (PAED) as a modified PEO technology was studied to fast manufacture the low-cost and binder-free anodes of the high-capacity lithium-ion batteries. In the PAED process, the  $\text{Co}(\text{OH})_2$  and  $\text{Ni}_3(\text{PO}_4)_2$  actives materials grew directly on Ti foil within 2~3

mins to form binder-free anodes. Compared with powder anode materials, the shorter manufacture time of PAED can obvious reduce the cost of anode materials. The nature of binder-free of PAED synthesized anode materials can also efficiently simply the preparation process of LIB electrode.

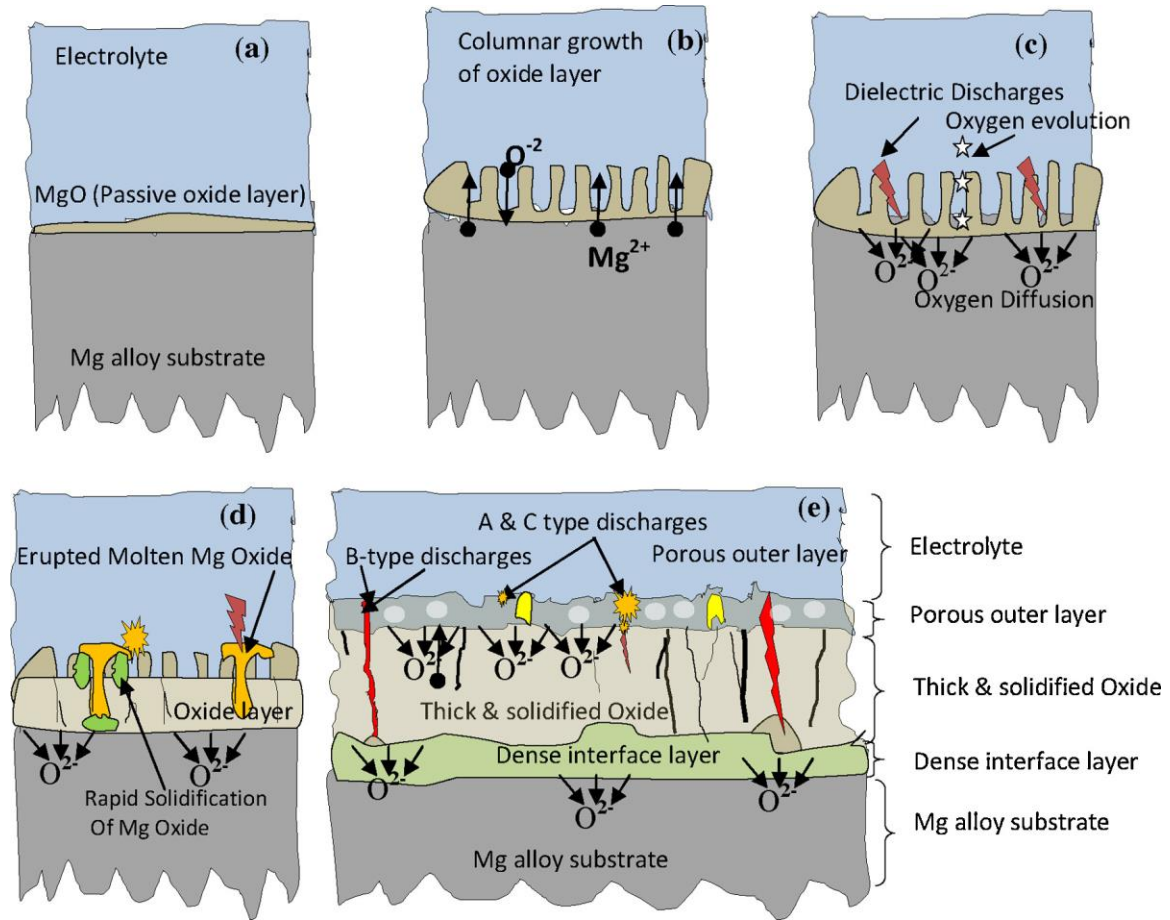


Figure 1-3. Growth process of PEO coating on Mg substrate.[12]

## 1.2 Objectives of this study

The objectives of this study are:

- 1) To use the plasma-assisted electrolytic deposition (PAED) to synthesize amorphous  $Co(OH)_2$  binder-free anode of the high-capacity lithium-ion battery.

- 2) To use the plasma-assisted electrolytic deposition (PAED) to synthesize amorphous  $\text{Ni}_3(\text{PO}_4)_2$  binder-free anode of the high-capacity lithium-ion battery.
- 3) To do a comparative electrochemical study between amorphous  $\text{Ni}_3(\text{PO}_4)_2$  and crystalline  $\text{Ni}_3(\text{PO}_4)_2$  anodes in lithium-ion batteries.
- 4) To explore the possible methods for improving the electrochemical performance of amorphous  $\text{Ni}_3(\text{PO}_4)_2$  anodes in lithium-ion batteries.

### ***1.3 Organization of the Thesis***

This thesis includes seven chapters. The Chapter 1 introduced the motivation and objectives of this research. The chapter 2 is a literature review on anode materials of lithium-ion batteries and the surface coating technologies for manufacturing binder-free anodes materials. The chapter 3 describe the experimental details. The chapter 4 and 5 describes the PAED synthesized  $\text{Co}(\text{OH})_2$  and  $\text{Ni}_3(\text{PO}_4)_2$  binder-free anodes and their electrochemical performance in LIBs. The chapter 6 is a comparative electrochemical study between amorphous  $\text{Ni}_3(\text{PO}_4)_2$  and crystalline  $\text{Ni}_3(\text{PO}_4)_2$  anodes in lithium-ion batteries. In chapter 7, possible methods for improving the electrochemical performance of amorphous  $\text{Ni}_3(\text{PO}_4)_2$  anodes in lithium-ion batteries were explored. Chapter 7 is a conclusion.



## REFERENCES

- [1] Wang, Jingjing, Tingting Xu, Xiao Huang, Huan Li, and Tingli Ma. "Recent progress of silicon composites as anode materials for secondary batteries." *Rsc Advances* 6, no. 90 (2016): 87778-87790.
- [2] Cho, Jaephil, Yong Jeong Kim, and Byungwoo Park. "Novel  $\text{LiCoO}_2$  cathode material with  $\text{Al}_2\text{O}_3$  coating for a Li ion cell." *Chemistry of Materials* 12, no. 12 (2000): 3788-3791.
- [3] Liu, Zhaolin, Aishui Yu, and J. Y. Lee. "Cycle life improvement of  $\text{LiMn}_2\text{O}_4$  cathode in rechargeable lithium batteries." *Journal of power sources* 74, no. 2 (1998): 228-233.
- [4] Liu, Hao, G. X. Wang, David Wexler, J. Z. Wang, and Hua-Kun Liu. "Electrochemical performance of  $\text{LiFePO}_4$  cathode material coated with  $\text{ZrO}_2$  nanolayer." *Electrochemistry communications* 10, no. 1 (2008): 165-169.
- [5] Kim, Sung-Soo, Yoshihiro Kadoma, Hiromasa Ikuta, Yoshiharu Uchimoto, and Masataka Wakihara. "Electrochemical performance of natural graphite by surface modification using aluminum." *Electrochemical and Solid-State Letters* 4, no. 8 (2001): A109-A112.
- [6] Arie, Arenst Andreas, Jin O. Song, and Joong Kee Lee. "Structural and electrochemical properties of fullerene-coated silicon thin film as anode materials for lithium secondary batteries." *Materials Chemistry and Physics* 113, no. 1 (2009): 249-254.
- [7] Poizot, P. L. S. G., S. Laruelle, S. Grugeon, L. Dupont, and J. M. Tarascon. "Nano-sized transition-metal oxides as negative-electrode materials for lithium-ion batteries." *Nature* 407, no. 6803 (2000): 496.
- [8] Zhai, Zhenting, Qiang Liu, Yu Zhu, Jina Cao, and Shaojun Shi. "Synthesis of  $\text{Ni(OH)}_2$ /graphene composite with enhanced electrochemical property by stirring solvothermal method." *Journal of Alloys and Compounds* 775 (2019): 1316-1323.

- [9] Chen, Wei Xiang, Jim Yang Lee, and Zhaolin Liu. "The nanocomposites of carbon nanotube with Sb and SnSb<sub>0.5</sub> as Li-ion battery anodes." *Carbon* 41, no. 5 (2003): 959-966.
- [10] Armand, Michel, and J-M. Tarascon. "Building better batteries." *Nature* 451, no. 7179 (2008): 652-657
- [11] Li, Tao, Ran Cai, Xueyuan Nie, and Jimi Tjong. "Porous Ni<sub>3</sub>(PO<sub>4</sub>)<sub>2</sub> thin film as a binder-free and low-cost anode of a high-capacity lithium-ion battery." *Journal of Electroanalytical Chemistry* (2019): 81-85
- [12] Hussein, R. O., X. Nie, and D. O. Northwood. "An investigation of ceramic coating growth mechanisms in plasma electrolytic oxidation (PEO) processing." *Electrochimica Acta* 112 (2013): 111-119.
- [13] Walsh, F. C., C. T. J. Low, R. J. K. Wood, K. T. Stevens, J. Archer, A. R. Poeton, and A. Ryder. "Plasma electrolytic oxidation (PEO) for production of anodised coatings on lightweight metal (Al, Mg, Ti) alloys." *Transactions of the IMF* 87, no. 3 (2009): 122-135.

## CHAPTER 2

### Literature Review on Materials and Surface Coating Technologies for Lithium-Ion Batteries

#### 2.1 Cathode materials of lithium-ion batteries

For the cathode materials, the choices of materials types are limited. Currently, the research and applications of cathode materials mainly focus on Lithium oxometallate materials such as the  $\text{LiCoO}_2$ ,  $\text{LiMn}_2\text{O}_4$  and  $\text{LiFeO}_4$ . [1-3]

##### 2.1.1 $\text{LiCoO}_2$ cathode

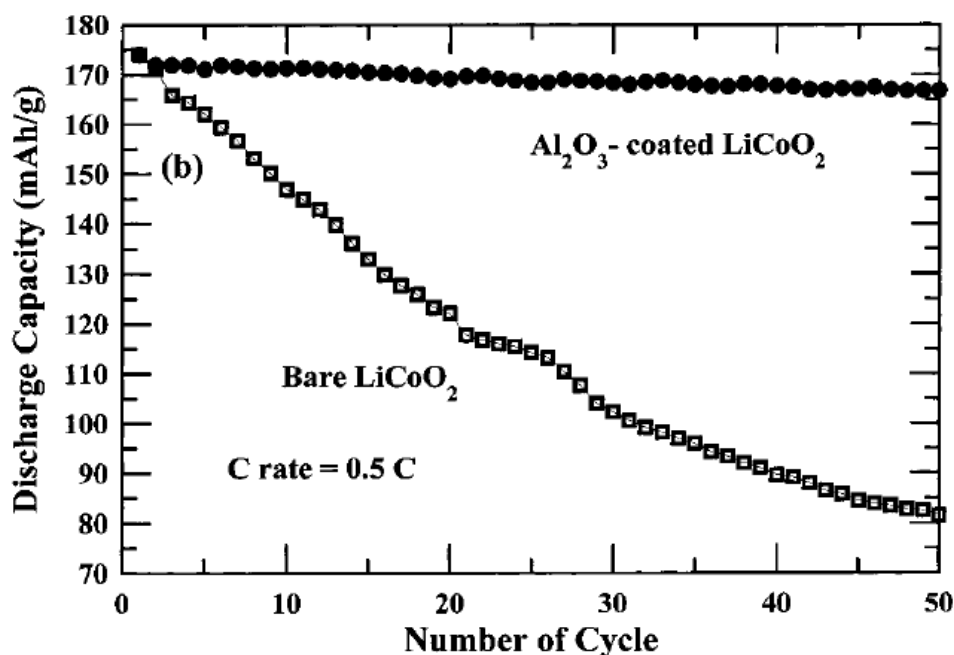


Figure 2-1. The cycling performance of  $\text{LiCoO}_2$  and  $\text{Al}_2\text{O}_3/\text{LiCoO}_2$  cathodes in lithium-ion batteries. [1]

The typical cycling performance of  $\text{LiCoO}_2$  as the cathode material has been shown in Figure 1-2. [1] The degradation rate on capacity of  $\text{LiCoO}_2$  is very high. Even after  $\text{Al}_2\text{O}_3$  protection, the capacity only has 170 mAh/g during 50 cycles.

### 2.1.2 $\text{LiMn}_2\text{O}_4$ cathode

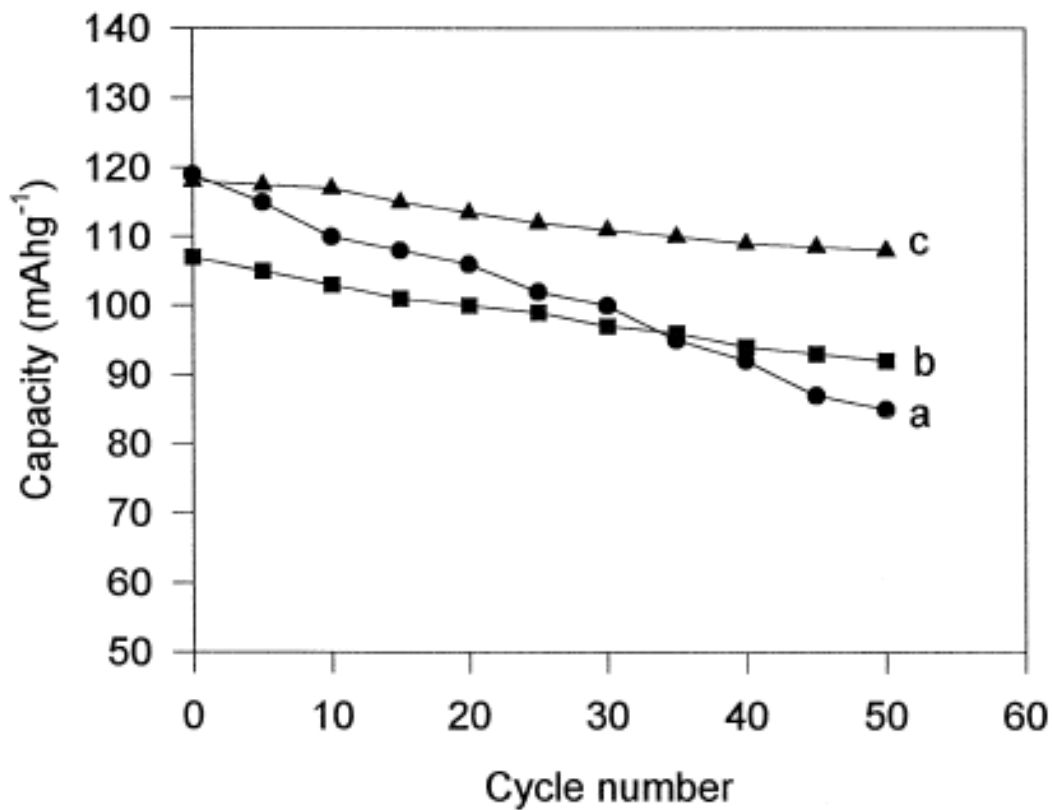


Figure 2-2. The cycling performance of  $\text{LiMn}_2\text{O}_4$  (a) and  $\text{LiCo}_{0.1}\text{Mn}_{1.9}\text{O}_4$  (b) cathodes in lithium-ion batteries.[2]

The typical cycling performance  $\text{LiMn}_2\text{O}_4$  can be found in Figure 2-2a,[2] where the capacity of the  $\text{LiMn}_2\text{O}_4$  only can reach 120 mAh/g during 50 cycles. After the Co compounded (Figure 2-2b), the degradation rate on capacity of  $\text{LiMn}_2\text{O}_4$  was reduced but the capacity still maintains at 90~110 mAh/g during cycling.

### 2.1.3 $\text{LiFePO}_4$ cathode

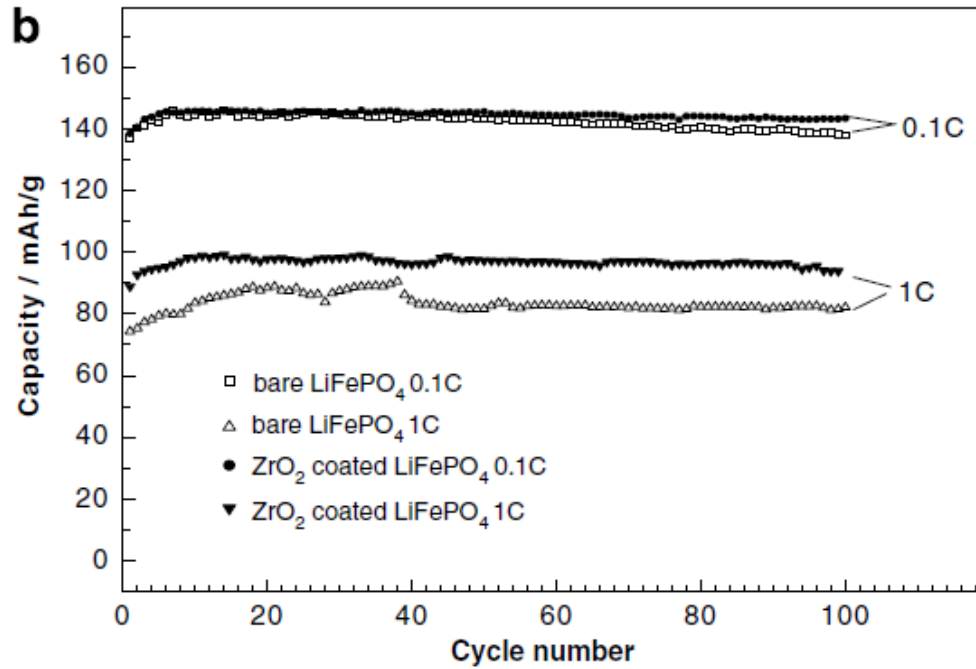


Figure 2-3. The cycling performance of  $\text{LiFePO}_4$  and  $\text{ZrO}_2/\text{LiFePO}_4$  cathodes in lithium-ion batteries.[3]

Figure 2-3 shows the typical cycling performance of  $\text{LiFePO}_4$  cathode in lithium-ion battery.[3] Compared with  $\text{LiCoO}_2$  and  $\text{LiMn}_2\text{O}_4$ , the cycling stability of  $\text{LiFePO}_4$  is the best. However, the capacity of  $\text{LiFePO}_4$  only has about 80 mAh/g during cycling at 1C current density. After  $\text{ZrO}_2$  protection, the capacity of  $\text{LiFePO}_4$  was improved to around 95 mAh/g in 100 cycles

### 2.2 Anode materials of lithium-ion batteries

According to the above brief review on cathode materials of lithium-ion batteries, it can be seen that the choices of materials types for cathode are less and their capacity are low in lithium-ion batteries. Therefore, researchers try to develop the anode materials to further improve the properties of lithium-ion batteries since there has more choices and

higher theoretical capacity for anode materials in comparison with cathode materials. The synthetic methods for anode materials are also more various than that of cathode materials.

### 2.2.1 Traditional anode materials

The main traditional anode materials are graphite and silicon. The advantages of graphite and silicon are their abundant resources and simple manufacture process. However, their performances on cycling stability and capacity are unsatisfied. The cycling performances of graphite and silicon were shown in Figure 2-4 and Figure 2-5,[4-5] respectively.

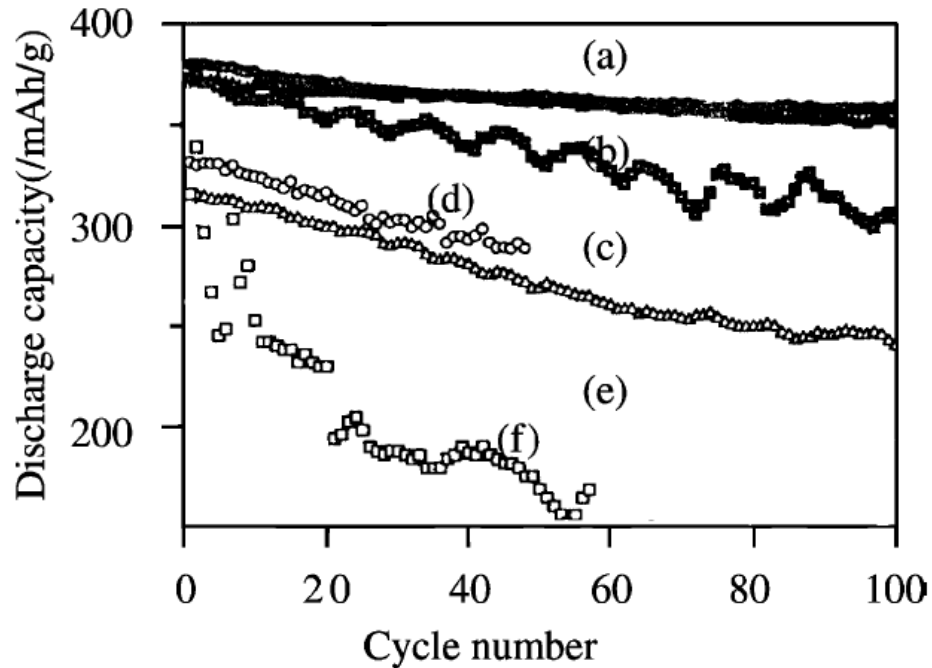


Figure 2-4. Cycling performance of natural graphite anode (d,e and f).[4]

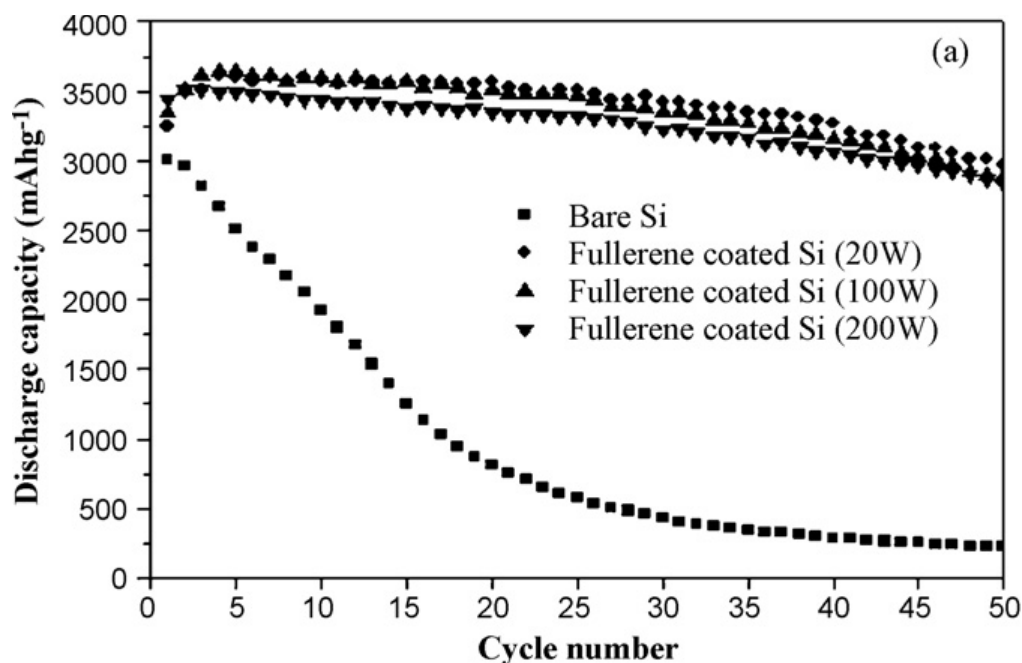


Figure 2-5. Cycling performance of silicon film anode.[5]

According to the Figure 2-4 and Figure 2-5,[4-5] capacity of both graphite and silicon are lower than 300mAh/g in long-term cycling performance. The low capacities of them limited the wide application of current commercial lithium-ion batteries. Therefore, it is necessary to explore other types of anode materials with higher capacity to replace the traditional graphite and silicon anodes.

### 2.2.2 Alloy anode materials

Due to the low capacity of graphite, some researchers try to add the graphite or carbon into metal elements to synthesize alloy anode materials for lithium-ion batteries. In Figure 2-6,[6] carbon and graphite was used to alloy with Sb, and the capacity of these alloy anodes were investigated in lithium-ion batteries.

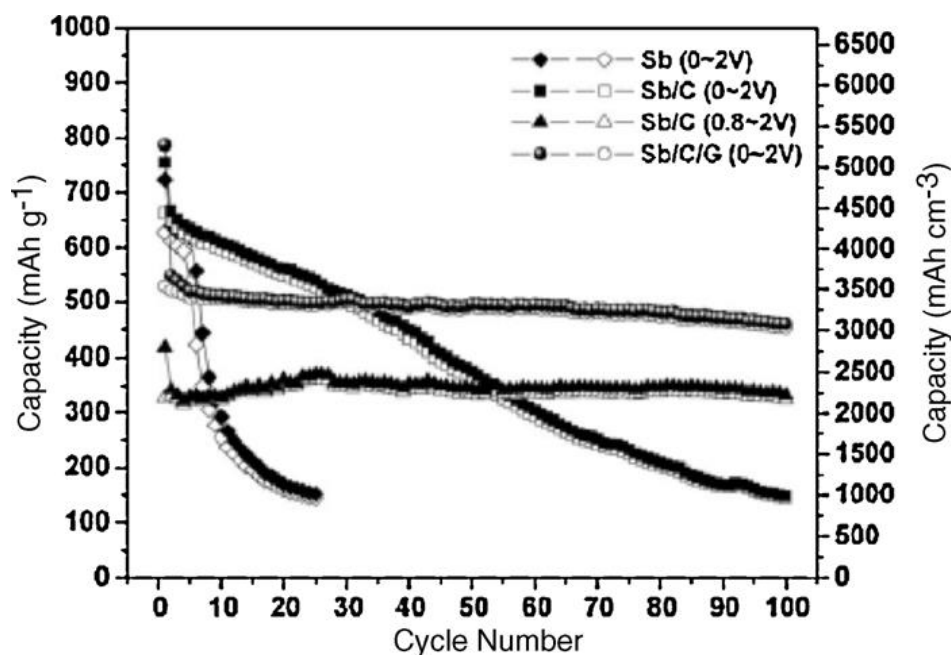


Figure 2-6. Comparison of cycle performance for Sb, Sb/carbon and Sb/carbon/graphite nanocomposites.[6]

In Figure 2-6,[6] it can be seen that the pure Sb anode shows a poor capacity and cycling stability in electrochemical tests. Nevertheless, after Sb was alloyed with carbon, the capacity can reach 650 mAh/g initially and obtain 150 mAh/g at 100th cycle. After Sb was alloyed with both carbon and graphite, the capacity can maintain at 500 mAh/g in 100 cycles. The capacity of alloy anode is higher than that of pure Sb anode and pure graphite anode. After alloying, the cycling stability of was also improved. These results indicate that the alloy is an appropriate anode material for the lithium-ion battery.

### 2.2.3 Nano-sized transition-metal oxides anode materials

Although the electrochemical performance of alloy anode materials is better than traditional silicon and carbon anodes, but the capacity of alloy anodes is still low, which cannot satisfy the demand of batteries in automobile industry. The nano-sized transition-



metal oxides anode materials were recognized as anode materials at initial 20th century. The cycling performance of four metal oxide anode materials are shown in Figure 2-7.[7] The capacity of FeO, NiO and CoO anodes can arrive 600-700 mAh/g. The degradation rate on capacity of FeO and NiO is high during 50 cycles, while the capacity of CoO is able to maintain around 650 mAh/g in cycling. For the  $\text{Co}_3\text{O}_4$  anode, the capacity nearly reached 1000 mAh/g without an obvious degradation on capacity. These results indicated that some nano-sized transition-metal oxides are ideal anode materials for lithium-ion batteries.

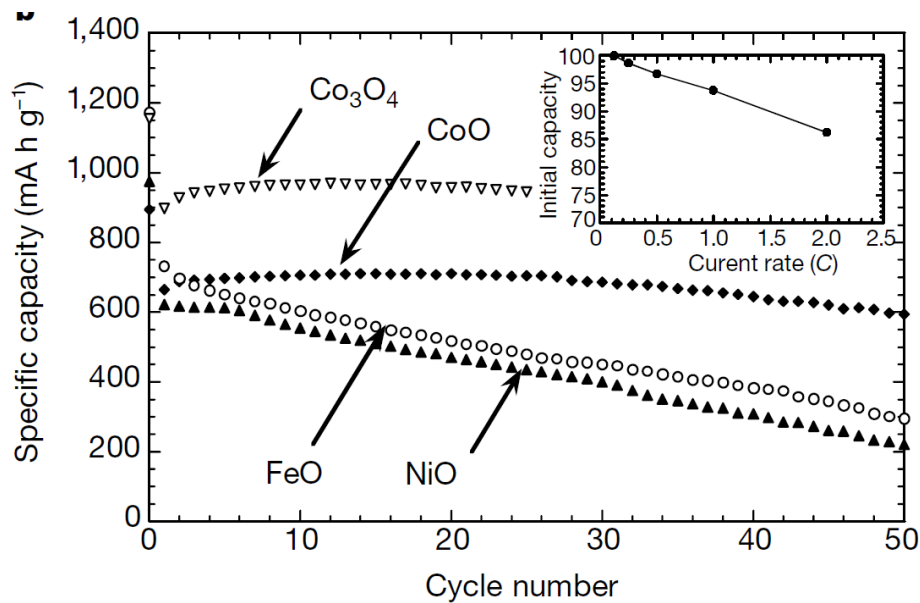


Figure 2-7. Capacity of nano-sized transition-metal oxides anode materials.[7]

#### 2.2.4 Graphene and carbon nanotubes anode materials

The graphene and carbon nanotube as two types of single layer carbon materials were found that they have remarkable electrochemical performance as anodes in lithium ion batteries. Therefore, researchers tried to use carbon nanotubes(CNTs) or graphene to improve the electrochemical performance of alloy and metal oxide anodes in lithium-ion

batteries.[8]

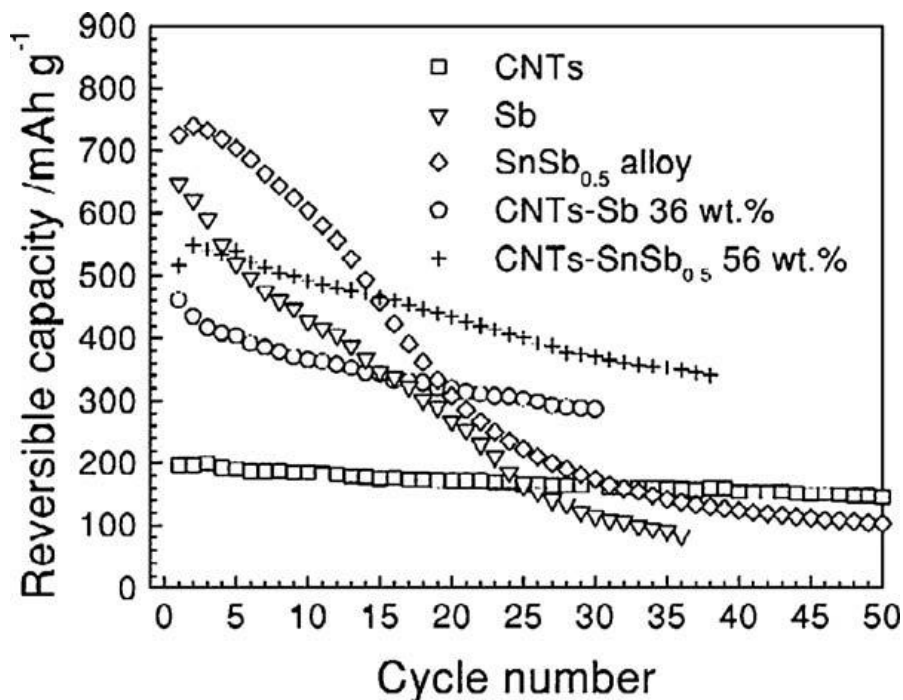


Figure 2-8. Reversible capacity of CNTs, Sb, SnSb<sub>0.5</sub>, CNTs-Sb and CNTs-SnSb<sub>0.5</sub>. [8]

Figure 2-8 shows the cycling performances of SnSb alloy anode and carbon nanotubes modified SnSb alloy anodes.[8] The pure SnSb alloy anode acquires 700 mAh/g capacity but performs very high degradation rate on capacity during cycling. At 50th cycle, the capacity dropped to 100mAh/g. However, after the SnSb alloy was modified by carbon nanotubes, the capacity of SnSb-CNTs anode tends to be stable during cycling. After 40 cycles, the SnSb anode still keeps the capacity of 350 mAh/g. The remarkable conductivity and lithium storage ability of carbon nanotubes contributes to the improvement on cycling performance.[8]

Similarly, some researchers used graphene to modify the metal oxide. The electrochemical performance of metal oxide anodes was also improved due to adding

graphene, such as the  $\text{Co}_3\text{O}_4$ /graphene composite.(Figure 2-9)[9]

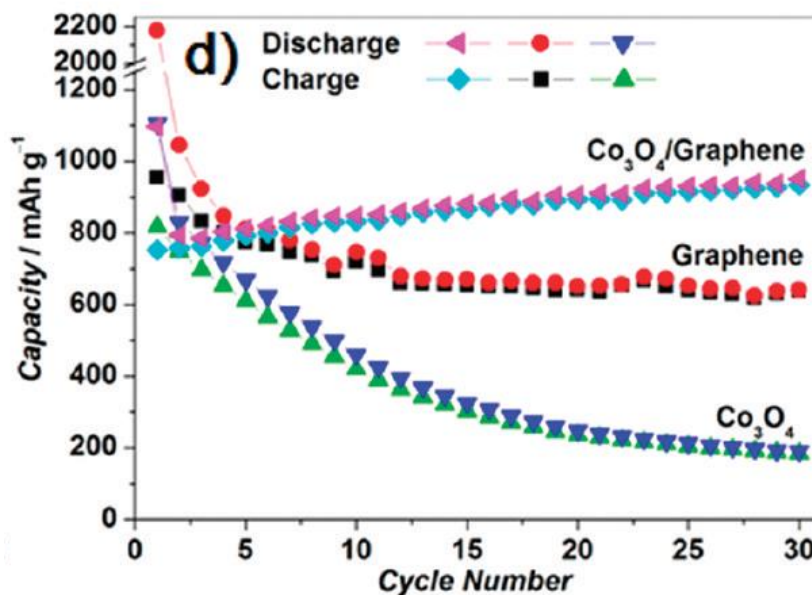


Figure 2-9. Comparison of the cycling performance of graphene,  $\text{Co}_3\text{O}_4$ , and the  $\text{Co}_3\text{O}_4$ /graphene composite.[9]

For the pure  $\text{Co}_3\text{O}_4$  anode, the capacity can reach 800  $\text{mAh/g}$  but drop to 200  $\text{mAh/g}$  after 25 cycles. For the pure graphene anode, the capacity can remain at 700  $\text{mAh/g}$  during 30 cycles without obvious degradation on capacity. After the  $\text{Co}_3\text{O}_4$  was modified by graphene, the capacity of composite anode exhibits a rising trend during cycling, which results from the remarkable electrons conductivity and lithium storage capability of graphene. The capacity of composite anode is higher than that of pure  $\text{Co}_3\text{O}_4$  anode and pure graphene anode since the synergistic effect between  $\text{Co}_3\text{O}_4$  and graphene in the composite.[9]

### 2.2.5 Metal hydroxide anode materials

Metal hydroxide as a candidate for materials of supercapacitor have been recognized to

be use for anode materials of lithium-ion batteries. Some researchers investigated the electrochemical performance of  $\text{Ni}(\text{OH})_2$  anode in lithium-ion battery.[10]

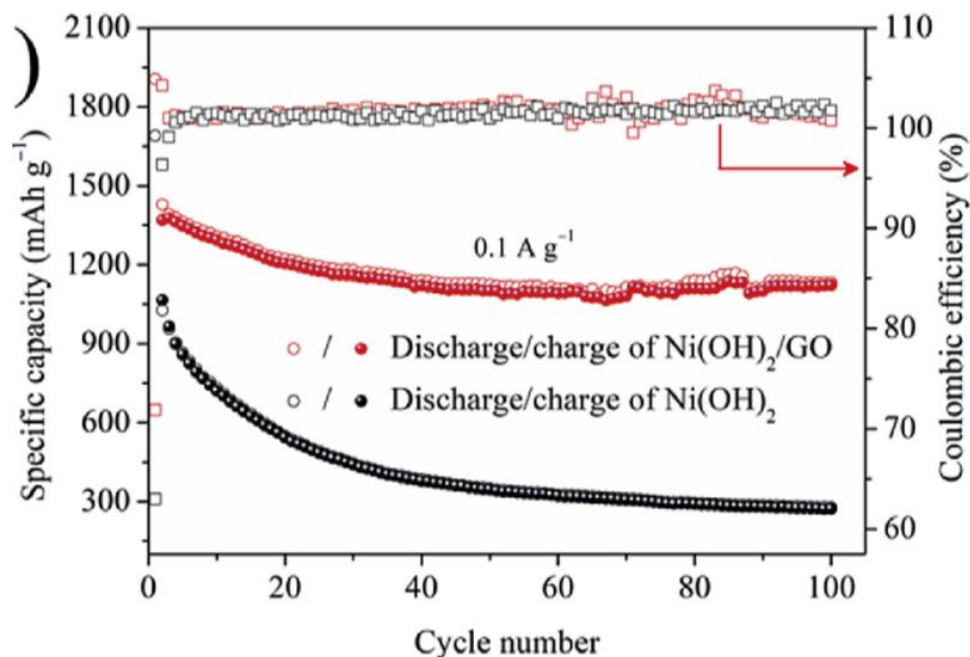


Figure 2-10. Cycling performance of  $\text{Ni}(\text{OH})_2$  and the  $\text{Ni}(\text{OH})_2/\text{GO}$  composite.[10]

As can be seen in Figure 2-10,[10] in the cycling performance, the capacity of  $\text{Ni}(\text{OH})_2$  can reach 1050 mAh/g and remain at 300 mAh/g during 100 cycles. After graphene oxide (GO) composited, the capacity of  $\text{Ni}(\text{OH})_2/\text{GO}$  stabilized at around 1050 mAh/g during cycling. High capacity of  $\text{Ni}(\text{OH})_2$  indicates that metal hydroxide could be a choice for anode material of the lithium-ion battery.

### 2.2.6 Oxometallate anode materials

For the oxometallate, some paper considered them as the anode materials of lithium-ion batteries. According to the report about the  $\text{Co}_2\text{TiO}_4$  and carbon coated  $\text{Co}_2\text{TiO}_4$  (Figure 2-11),[11] the capacity of  $\text{Co}_2\text{TiO}_4$  can stabilize at 150 mAh/g during 50 cycles. After carbon coating, the capacity of  $\text{Co}_2\text{TiO}_4@\text{C}$  was improved to 200 mAh/g, which indicate

that the oxometallate could be used as anode materials after modification with other materials.

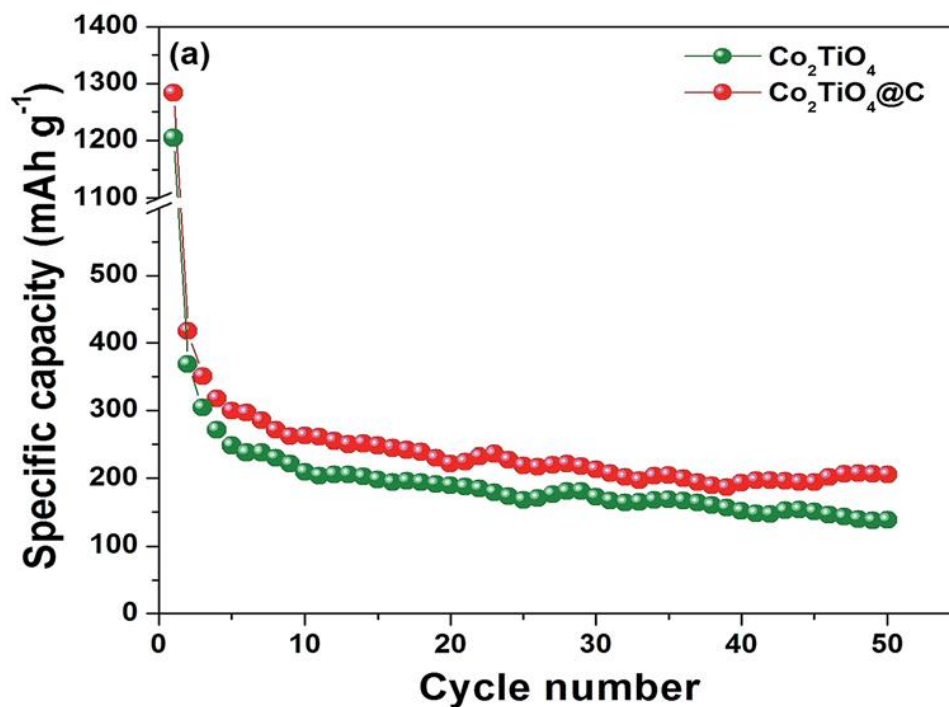


Figure 2-11. Cycling performance of Co<sub>2</sub>TiO<sub>4</sub> and the Co<sub>2</sub>TiO<sub>4</sub>@C composite.[11]

## 2.3 Surface coating technologies for binder-free anodes of lithium-ion batteries

### 2.3.1 Physical vapor deposition (PVD)

Although the nano-powder anode materials make lithium ion batteries obtain the high capacity in electrochemical tests, but long-time preparation will lead to the high-cost in manufacture process. Furthermore, nano-powder anodes are usually mixed with binder in manufacture process, which causes the decrease of electrochemical performance of anodes. Therefore, to fabricate anodes with advantages of low-cost and high electrochemical performance, some thin film synthetic technologies were used to fabricate the binder-free and low-cost anodes of lithium-ion batteries such as physical

vapor deposition (PVD).

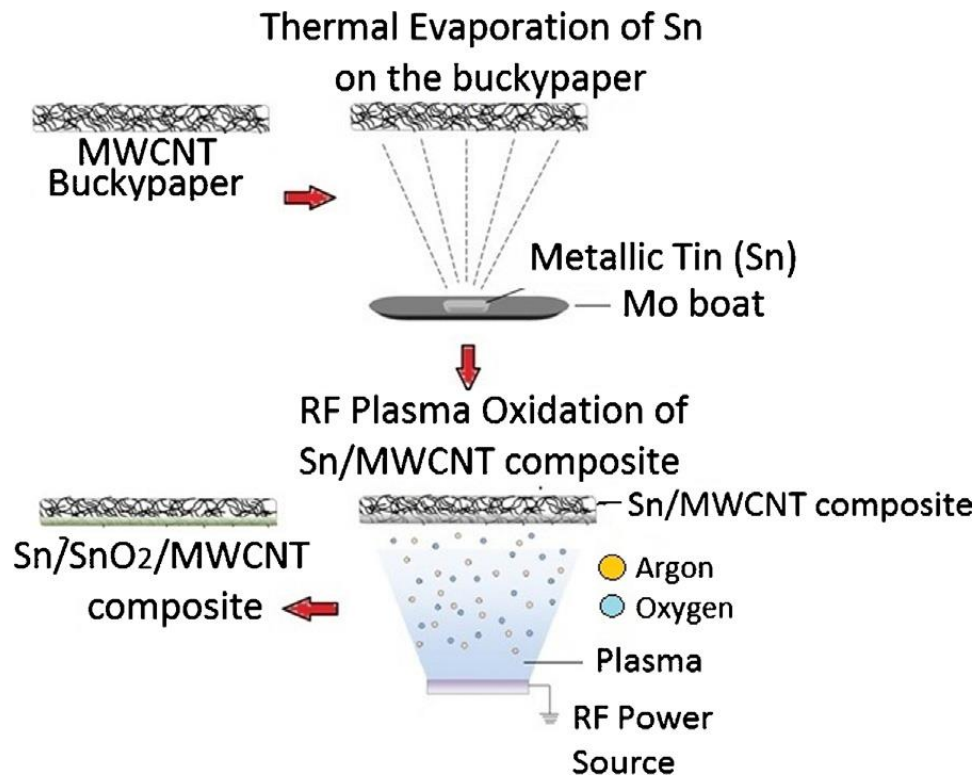


Figure 2-12. preparation method of Sn/SnO<sub>2</sub>/MWCNT composites.[12]

Some researchers used PVD to manufacture binder-free Sn/SnO<sub>2</sub>/multi-walled carbon nanotube (MWCNT) anode papers for Li-ion batteries.[12] In their report, binder-free Sn/SnO<sub>2</sub>/MWCNT nanocomposite anode paper was prepared by thermal evaporation and subsequent plasma oxidation (Figure 2-12).[12] Initially, oxidation of MWCNT was carried out. The next steps are the thermal evaporation of metallic tin on MWCNT and plasma oxidation for tin matrix.[12]

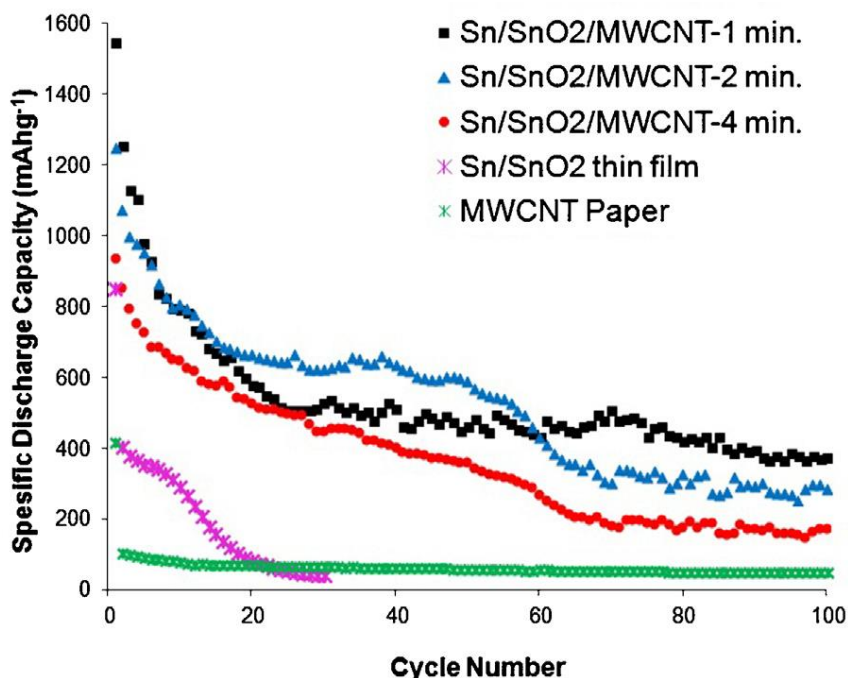


Figure 2-13. Specific discharge capacities with cycle number of electrodes.[12]

The cycling performance of the Sn/SnO<sub>2</sub>/MWCNT electrodes, MWCNT and Sn/SnO<sub>2</sub> binder-free electrodes is investigated in Figure 2-13.[12] The Sn/SnO<sub>2</sub> shows a high degradation rates during 30 cycles. The capacity of MWCNT is approximately 90 mAh/g for long-term cycling. For the Sn/SnO<sub>2</sub>/MWCNT, the cycling performance was improved along with shorter evaporation time. For the Sn/SnO<sub>2</sub>/MWCNT evaporated 1 min, the capacity can reach 1200 mAh/g and remain at 650 mAh/g after 20 cycles. After 60 cycles, the capacity keeps at 300 mAh/g.

### 2.3.2 Chemical vapor deposition (CVD)

The PVD provides us a simple way to manufacture the binder-free anode for lithium ion battery. However, in the cycling performance testing that we mentioned above, the capacity shows an obvious degradation in long-term cycling. Therefore, to try other methods to prepare the binder-free anode is necessary such as the chemical vapor



deposition (CVD). CVD can be used to manufacture the binder-free thin film anodes for lithium ion batteries, such as Si nanoparticles. The silica particles are firstly coated onto a stainless-steel substrate. Then, the Si is CVD deposited on it. Subsequently, the  $\text{SiO}_2$  spheres are removed by etching. Lastly, the Si hollow spheres thin film was obtained on substrate.[13] The CVD synthetic process and morphology of Si anode were illustrated in Figure 2-14.[13]

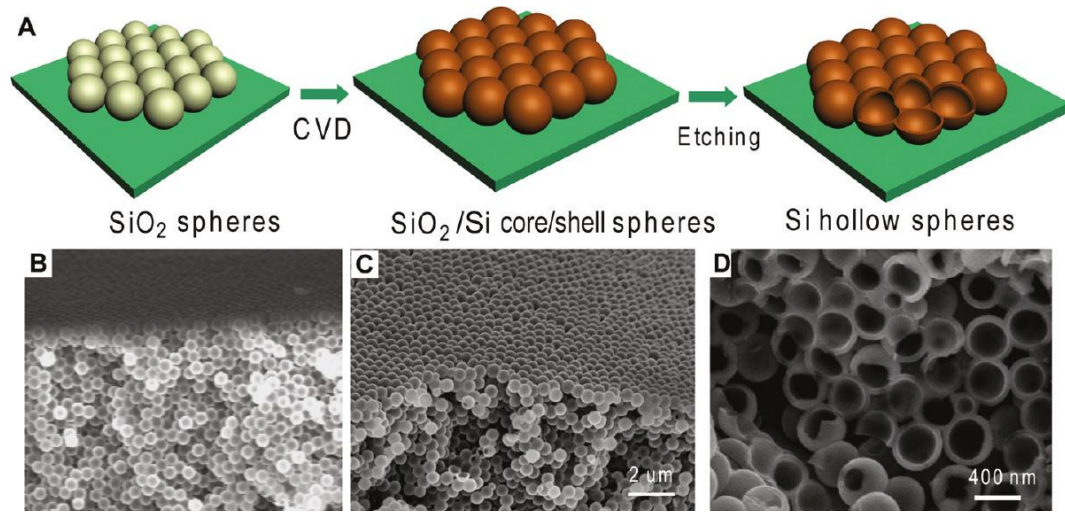


Figure 2-14. The synthetic process and morphology of Si anode.[13]

The cycling performance of Si anode has been shown in Figure 2-15,[13] The Columbic efficiency keeps at around 99.5 % during the cycling. The capacity of Si hollow spheres anodes is very high. After 700 cycles, the discharge capacity still has 1400 mAh/g, which is approximately 4 times of the theoretical capacity of graphite anode (372 mAh/g).



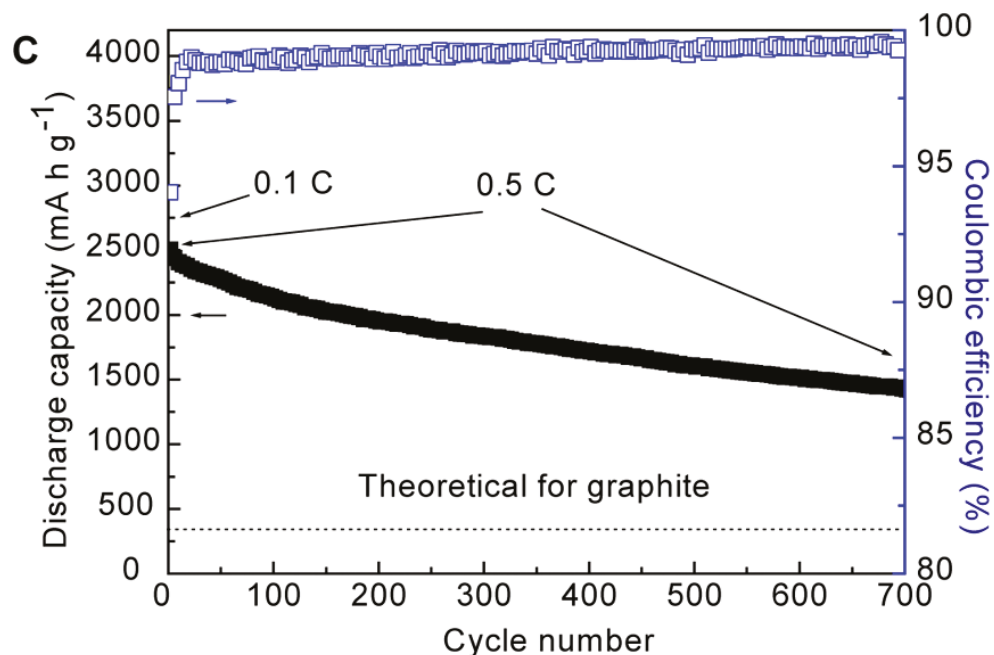


Figure 2-15. Reversible discharge capacity and coulombic efficiency of the hollow Si spheres anode in comparison with the theoretical capacity of graphite.[13]

### 2.3.3 Plasma electrolytic oxidation (PEO)

The plasma electrolytic oxidation (PEO) as a surface coating technology was usually used on wearing resistance and corrosion prevention of Mg, Al, Ti and their alloys. Recently, some researchers used the PEO to fabricate the porous SiO<sub>2</sub>/TiO<sub>2</sub> composite thin film as the binder-free anode of lithium-ion battery.[14] Ti foil was used as the substrate. The morphology of PEO SiO<sub>2</sub>/TiO<sub>2</sub> composite coating was performed in Figure 2-16.[11] And the cycling performance of PEO SiO<sub>2</sub>/TiO<sub>2</sub> anode and other types of TiO<sub>2</sub> anodes in lithium ion batteries was investigated in Figure 2-17.[14]

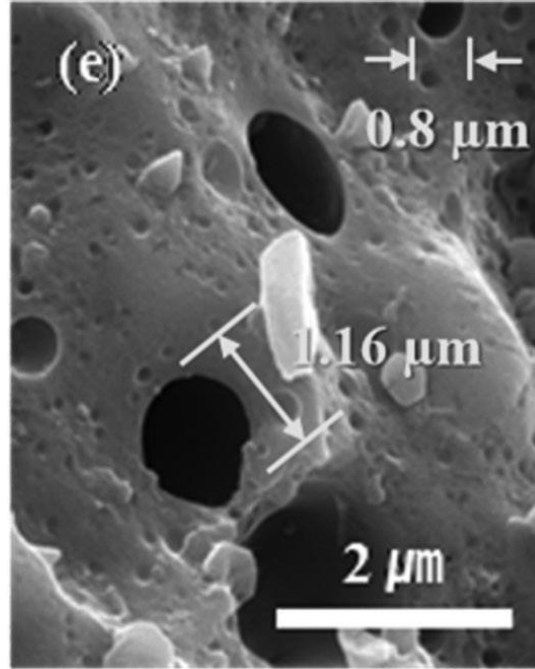


Figure 2-16. The morphology of PEO SiO<sub>2</sub>/TiO<sub>2</sub> composite coating.[14]

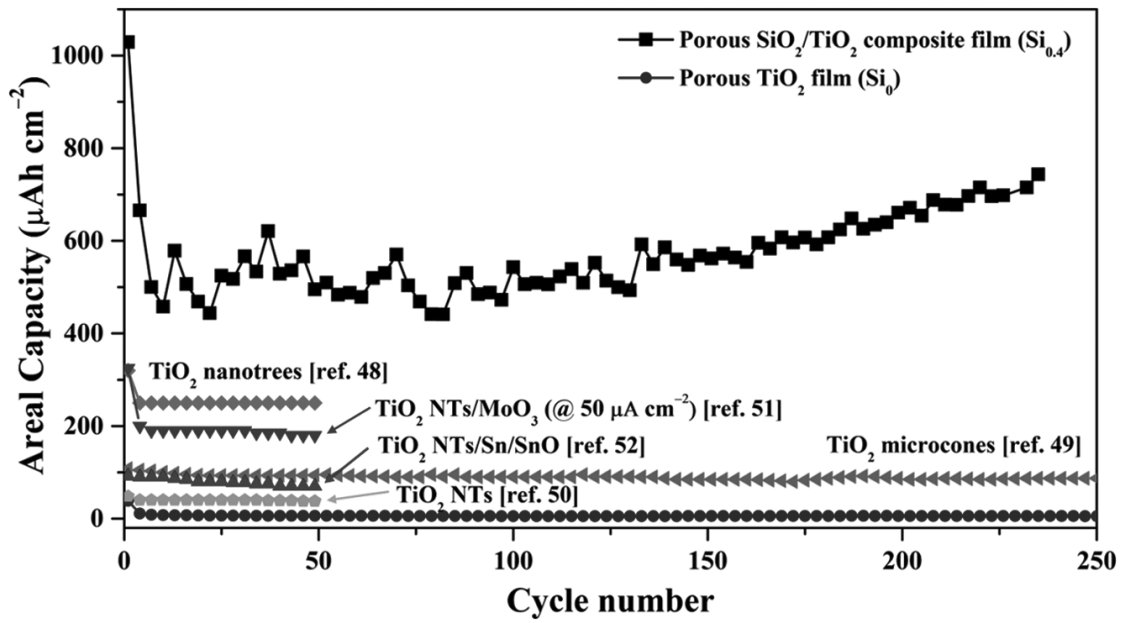


Figure 2-17. Cycling performance of PEO SiO<sub>2</sub>/TiO<sub>2</sub> anode and other types of TiO<sub>2</sub> anodes in lithium ion batteries.[14]

In Figure 2-17,[14] the PEO SiO<sub>2</sub>/TiO<sub>2</sub> anode obtained a higher capacity than that of the other types TiO<sub>2</sub> electrodes including the TiO<sub>2</sub> nanotrees, TiO<sub>2</sub> microcones, TiO<sub>2</sub> NTs, TiO<sub>2</sub>, TiO<sub>2</sub> NTs/Sn/SnO and NTs/MoO<sub>3</sub>. The areal capacity of the PEO SiO<sub>2</sub>/TiO<sub>2</sub> anode can reach 1000  $\mu\text{Ah}/\text{cm}^2$  and keep a remarkable cycling stability during 200 cycles. The high electrochemical performance should be attributed to the pores structure in Figure 2-16,[14] which provides efficient Li<sup>+</sup> diffusion paths during charge/discharge process.[14]

### 2.3.4 Electrochemical anodization

The electrochemical anodization is a technology to oxide the metal or alloy surface by applying current or voltage. Some researchers tried to use electrochemical anodization to prepare the binder-free anode materials for lithium ion batteries. According to the report,[15] TiO<sub>2</sub> nanotubes binder-free anode can be prepared by electrochemical anodization on Ti substrate. The SEM (Figure 2-18) shows that the morphology of TiO<sub>2</sub> nanotubes that were fabricated by electrochemical anodization on Ti substrate.[15]

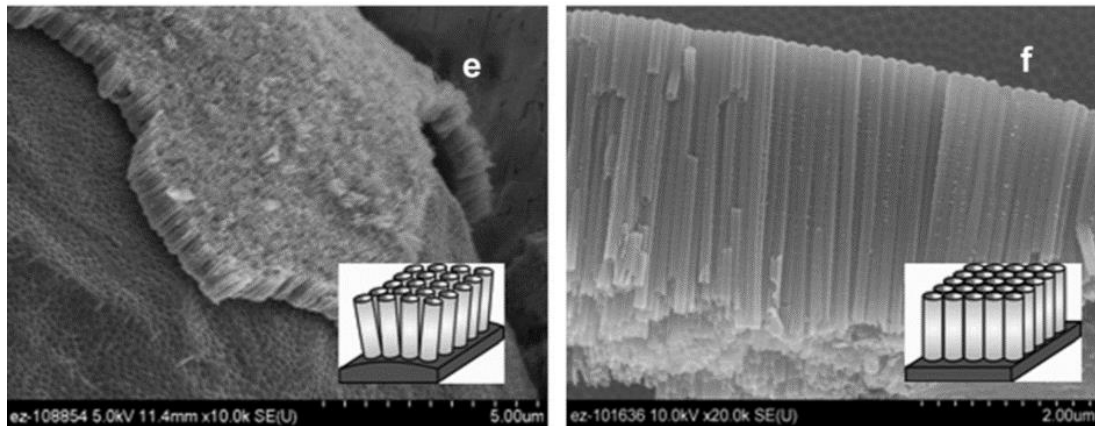


Figure 2-18. Morphology of TiO<sub>2</sub> nanotubes: (e) on Ti foam; (f) on Ti foil.[15]

The cycling performance of TiO<sub>2</sub> nanotubes on Ti foil and Ti foam has been show in Figure 2-19.[15] The capacity of TiO<sub>2</sub> nanotubes on Ti foil can stabilize at about 40

$\mu\text{Ah}/\text{cm}^2$  during 100 cycles. The capacity of  $\text{TiO}_2$  nanotubes on Ti foam can stabilize at around  $100 \mu\text{Ah}/\text{cm}^2$  during cycling. Therefore, the electrochemical anodization could be a great method to synthesize the binder-free anodes of lithium-ion batteries.

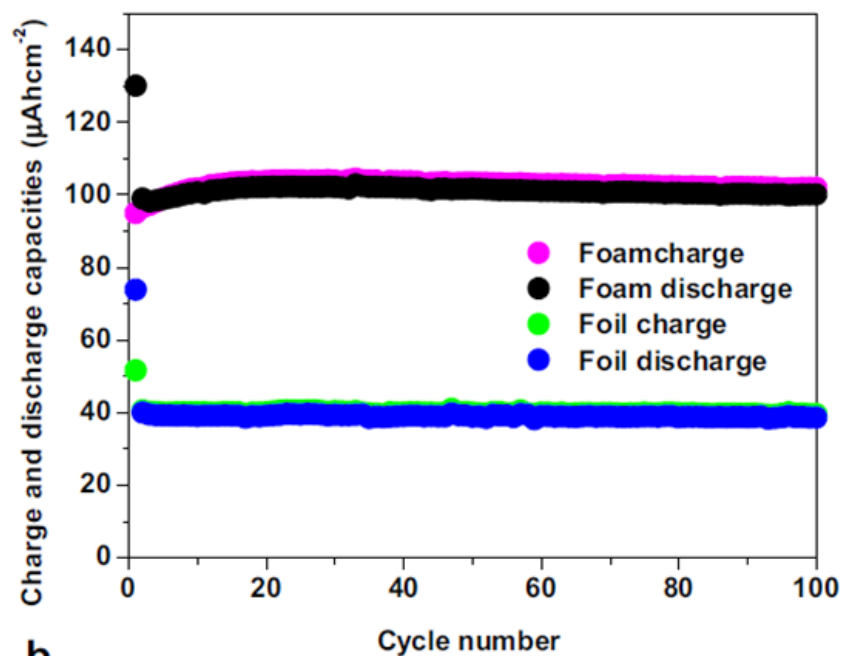


Figure 2-19. Cycling performance of  $\text{TiO}_2$  nanotubes on Ti substrates anodes in lithium ion batteries.[15]

## REFERENCES

- [1] Cho, Jaephil, Yong Jeong Kim, and Byungwoo Park. "Novel  $\text{LiCoO}_2$  cathode material with  $\text{Al}_2\text{O}_3$  coating for a Li ion cell." *Chemistry of Materials* 12, no. 12 (2000): 3788-3791.
- [2] Liu, Zhaolin, Aishui Yu, and J. Y. Lee. "Cycle life improvement of  $\text{LiMn}_2\text{O}_4$  cathode in rechargeable lithium batteries." *Journal of power sources* 74, no. 2 (1998): 228-233.
- [3] Liu, Hao, G. X. Wang, David Wexler, J. Z. Wang, and Hua-Kun Liu. "Electrochemical performance of  $\text{LiFePO}_4$  cathode material coated with  $\text{ZrO}_2$  nanolayer." *Electrochemistry communications* 10, no. 1 (2008): 165-169.
- [4] Kim, Sung-Soo, Yoshihiro Kadoma, Hiromasa Ikuta, Yoshiharu Uchimoto, and Masataka Wakihara. "Electrochemical performance of natural graphite by surface modification using aluminum." *Electrochemical and Solid-State Letters* 4, no. 8 (2001): A109-A112.
- [5] Arie, Arenst Andreas, Jin O. Song, and Joong Kee Lee. "Structural and electrochemical properties of fullerene-coated silicon thin film as anode materials for lithium secondary batteries." *Materials Chemistry and Physics* 113, no. 1 (2009): 249-254.
- [6] Park, Cheol-Min, Sukeun Yoon, Sung-Il Lee, Jae-Hun Kim, Jin-Ho Jung, and Hun-Joon Sohn. "High-rate capability and enhanced cyclability of antimony-based composites for lithium rechargeable batteries." *Journal of The Electrochemical Society* 154, no. 10 (2007): A917-A920.
- [7] Poizot, P. L. S. G., S. Laruelle, S. Grugeon, L. Dupont, and J. M. Tarascon. "Nano-sized transition-metal oxides as negative-electrode materials for lithium-ion batteries." *Nature* 407, no. 6803 (2000): 496.

- [8] Chen, Wei Xiang, Jim Yang Lee, and Zhaolin Liu. "The nanocomposites of carbon nanotube with Sb and SnSb<sub>0.5</sub> as Li-ion battery anodes." *Carbon* 41, no. 5 (2003): 959-966.
- [9] Wu, Zhong-Shuai, Wencai Ren, Lei Wen, Libo Gao, Jinping Zhao, Zongping Chen, Guangmin Zhou, Feng Li, and Hui-Ming Cheng. "Graphene anchored with Co<sub>3</sub>O<sub>4</sub> nanoparticles as anode of lithium ion batteries with enhanced reversible capacity and cyclic performance." *ACS nano* 4, no. 6 (2010): 3187-3194.
- [10] Zhai, Zhenting, Qiang Liu, Yu Zhu, Jina Cao, and Shaojun Shi. "Synthesis of Ni(OH)<sub>2</sub>/graphene composite with enhanced electrochemical property by stirring solvothermal method." *Journal of Alloys and Compounds* 775 (2019): 1316-1323.
- [11] Yuvaraj, S., R. Hari Vignesh, L. Vasylechko, Y. S. Lee, and R. Kalai Selvan. "Synthesis and electrochemical performance of Co<sub>2</sub>TiO<sub>4</sub> and its core-shell structure of Co<sub>2</sub>TiO<sub>4</sub>@C as negative electrodes for Li-ion batteries." *RSC Advances* 6, no. 73 (2016): 69016-69026.
- [12] Alaf, M., D. Gultekin, and H. Akbulut. "Electrochemical properties of free-standing Sn/SnO<sub>2</sub>/multi-walled carbon nano tube anode papers for Li-ion batteries." *Applied Surface Science* 275 (2013): 244-251.
- [13] Yao, Yan, Matthew T. McDowell, Ill Ryu, Hui Wu, Nian Liu, Liangbing Hu, William D. Nix, and Yi Cui. "Interconnected silicon hollow nanospheres for lithium-ion battery anodes with long cycle life." *Nano letters* 11, no. 7 (2011): 2949-2954.
- [14] Lee, Gibaek, Sudeok Kim, Sunkyu Kim, and Jinsub Choi. "SiO<sub>2</sub>/TiO<sub>2</sub> Composite Film for High Capacity and Excellent Cycling Stability in Lithium-Ion Battery Anodes." *Advanced Functional Materials* 27, no. 39 (2017): 1703538.
- [15] Bi, Zhonghe, M. Parans Paranthaman, Paul A. Menchhofer, Ryan R. Dehoff, Craig A. Bridges, Miaofang Chi, Bingkun Guo, Xiao-Guang Sun, and Sheng Dai. "Self-organized amorphous TiO<sub>2</sub> nanotube arrays on porous Ti foam for rechargeable lithium and sodium ion batteries." *Journal of Power Sources* 222 (2013): 461-466.

## CHAPTER 3

### Experimental Details

#### ***3.1 Preparation of binder-free anode***

A Ti foil (Sigma Aldrich, thickness: 0.127mm) was immersed in an electrolyte in a stainless-steel vessel. One side of the Ti foil was protected by the special fixture (Figure 3-1). Then the Ti foil and stainless-steel vessel were connected with positive and negative terminals of a DC power supply, respectively. Lastly, 3A current were applied for 2-3 mins to obtain an amorphous film on Ti.(Figure 3-2) Sample was dried under 60 °C in Vacuum Oven.(Figure 3-3)

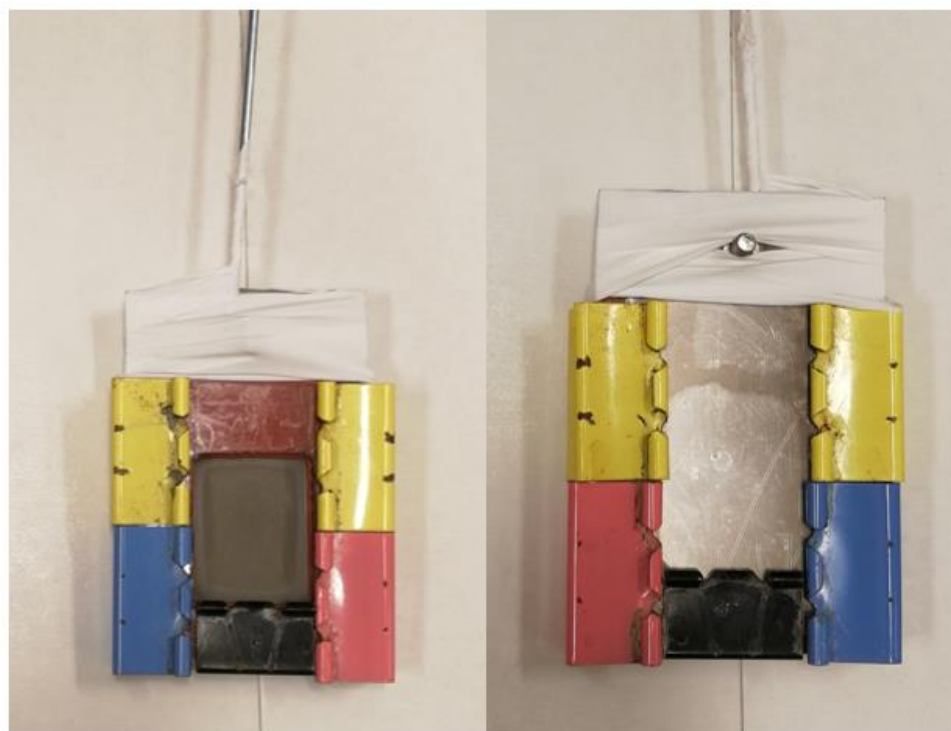


Figure 3-1. The fixture for single side protection.

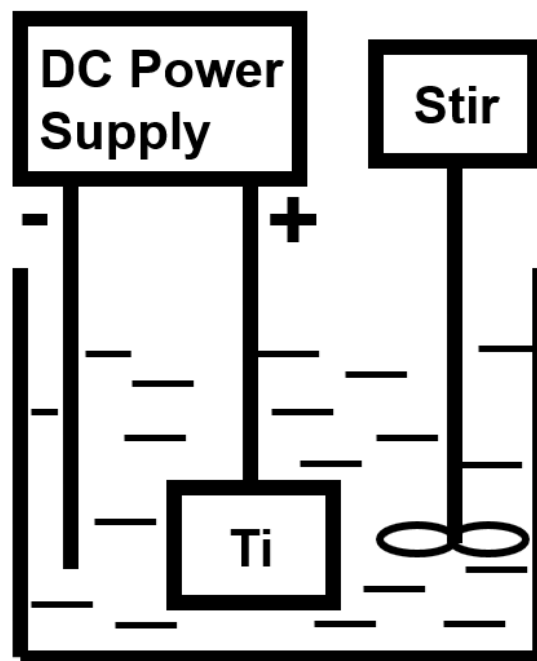


Figure 3-2. Schematic drawing of instrument.



Figure 3-3. Vacuum Oven.



### 3.2 Characterization of structure and morphology

Phases of the films were determined by X-ray diffraction (XRD, PROTO AXRD) (Figure 3-4) and X-ray photoelectron spectroscopy (XPS, Kratos Axis Nova). The XRD was set to detect samples from 10-70 or 20-80 2 theta degree. The microstructure observation was performed by scanning electron microscopy (SEM, Hitachi, TM 3030) (Figure 3-5). The EDS attachments can be seen on the right side of SEM in Figure 3-5.



Figure 3-4. XRD.



Figure 3-5. SEM and EDS attachments.

### ***3.3 Battery packaging***

The sample was cut to 16mm diameter disc which served as the working electrode. The lithium ribbon (Sigma Aldrich) and separator was cut to 16mm and 19mm diameter discs by the special cutter, respectively. (Figure 3-6) (MTI Crop.) The lithium is the counter electrode. Then, they were sealed into a CR2032 coin cell case with spring and steel disc by a coin cell sealer (Figure 3-6 and Figure 3-7) (MTI Crop.). The placement sequence of different parts in coin cell from bottom to top is: bottom shell (“+” mark), Cu, anode, separator, lithium, steel disc, spring and top shell. The  $\text{LiPF}_6$  is the electrolyte (Sigma

Aldrich, EC: DMC 1: 1), which should be added 4-5 drops on the anode surface before placing the separator. All the operations were completed in an Argon gas glove box (LABmaster 130) (Figure 3-8).

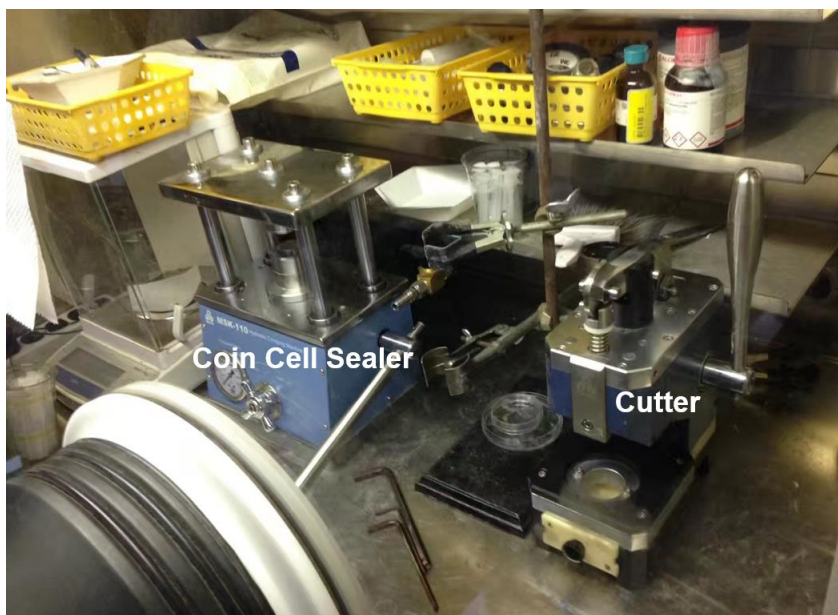


Figure 3-6. Cutter and coin cell sealer.



Figure 3-7. All parts in coin cell.



Figure 3-8. Argon gas glove box.

### ***3.4 Battery testing***

The cycling performance and rate capability of batteries were tested by LAND battery testing system CT2001A (Figure 3-9). The parameters of cycling performance test can be found in Figure 3-10. The parameters of rate capability test can be found in Figure 3-11. All the tests on battery testing system start from the discharge program.





Figure 3-9. LAND Battery Testing System CT2001A.

[illegible]

Figure 3-10. Parameters of cycling performance test.

Test Name		Parameter Setup		Safety Protection		
Stp	Variables	Mode	End Cond1	(And) End Cond2	GOTO	Log Cond
1		Discharge CC: 0.8 mA	Voltage <= 0.01 V		Next Step	01:00, 0.1V
2		Charge CC: 0.8 mA	Voltage >= 3 V		Next Step	01:00, 0.1V
3		<IF>	Cycle <= 10 Times		1	
		<OR>			Next Step	
4		Discharge CC: 1.2 mA	Voltage <= 0.01 V		Next Step	01:00, 0.1V
5		Charge CC: 1.2 mA	Voltage >= 3 V		Next Step	01:00, 0.1V
6		<IF>	Cycle <= 20 Times		4	
		<OR>			Next Step	
7		Discharge CC: 1.6 mA	Voltage <= 0.01 V		Next Step	01:00, 0.1V
8		Charge CC: 1.6 mA	Voltage >= 3 V		Next Step	01:00, 0.1V
9		<IF>	Cycle <= 30 Times		7	
		<OR>			Next Step	
10		Discharge CC: 2 mA	Voltage <= 0.01 V		Next Step	01:00, 0.1V
11		Charge CC: 2 mA	Voltage >= 3 V		Next Step	01:00, 0.1V
12		<IF>	Cycle <= 40 Times		10	
		<OR>			Next Step	
13		Discharge CC: 2.4 mA	Voltage <= 0.01 V		Next Step	01:00, 0.1V
14		Charge CC: 2.4 mA	Voltage >= 3 V		Next Step	01:00, 0.1V
15		<IF>	Cycle <= 50 Times		13	
		<OR>			Next Step	
16		Discharge CC: 0.8 mA	Voltage <= 0.01 V		Next Step	01:00, 0.1V
17		Charge CC: 0.8 mA	Voltage >= 3 V		Next Step	01:00, 0.1V
18		<IF>	Cycle <= 70 Times		16	
		<OR>			End_OK	
		New...				

Guide for typical test setup(old version)...

Unit Scheme: **Base on "mA"**

Figure 3-11. Parameters of rate capability test.

The cyclic voltammetry (CV) was tested by the electrochemical work-station (Biologic).(Figure 3-12) The corresponding parameters of testing can be found in Figure 3-13.

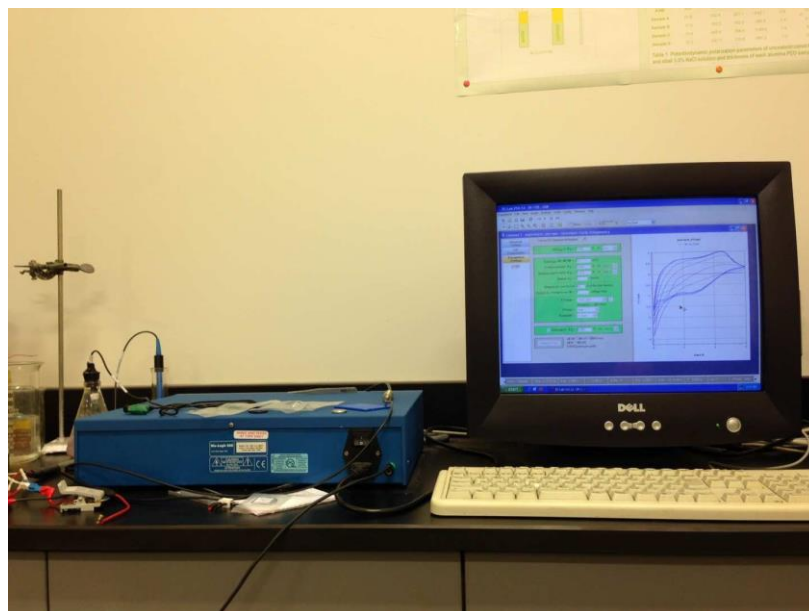


Figure 3-12. Bio-logic electrochemical work-station.

```

EC-Lab ASCII FILE
Nb header lines : 48

cyclic voltammetry
Run on channel : 1 (SN 3949)
Grouped channel(s) : 1
User :
CE vs. WE compliance from -10 v to 10 v
Electrode connection : standard
Ewe ctrl range : min = -10.00 v, max = 10.00 v
Acquisition started on : 10/03/2018 13:50:56

Ei (v)                0.000
vs.                   Eoc
dE/dt (mv/s)          0.100
E1 (v)                3.000
vs.                   Ref
Step percent          50
N                     10
E range min (v)       -10.000
E range max (v)       10.000
I Range               Auto
Bandwidth              5
E2 (v)                0.000
vs.                   Ref
nc cycles              5
Reverse Scan           1
Ef (v)                0.000
vs.                   Eoc

```

Figure 3-13. Parameters of CV test.

### ***3.5 Sputtering coating***

The sputtering coating was carried out in a sputtering coater with 10 times running (Quorum Q150R S) (Figure 3-14).



Figure 3-14. Sputtering coater.

### ***3.6 Preparation of metallographic specimens***

The Ti foil was hot mounted and then polished. The polished surface was etched by the solution with 2ml HF and 4ml HNO<sub>3</sub> in 100ml deionized water. The etching time was 12s. Lastly, the metallography was performed by microscopy (Olympus BX51M) (Figure 3-15).



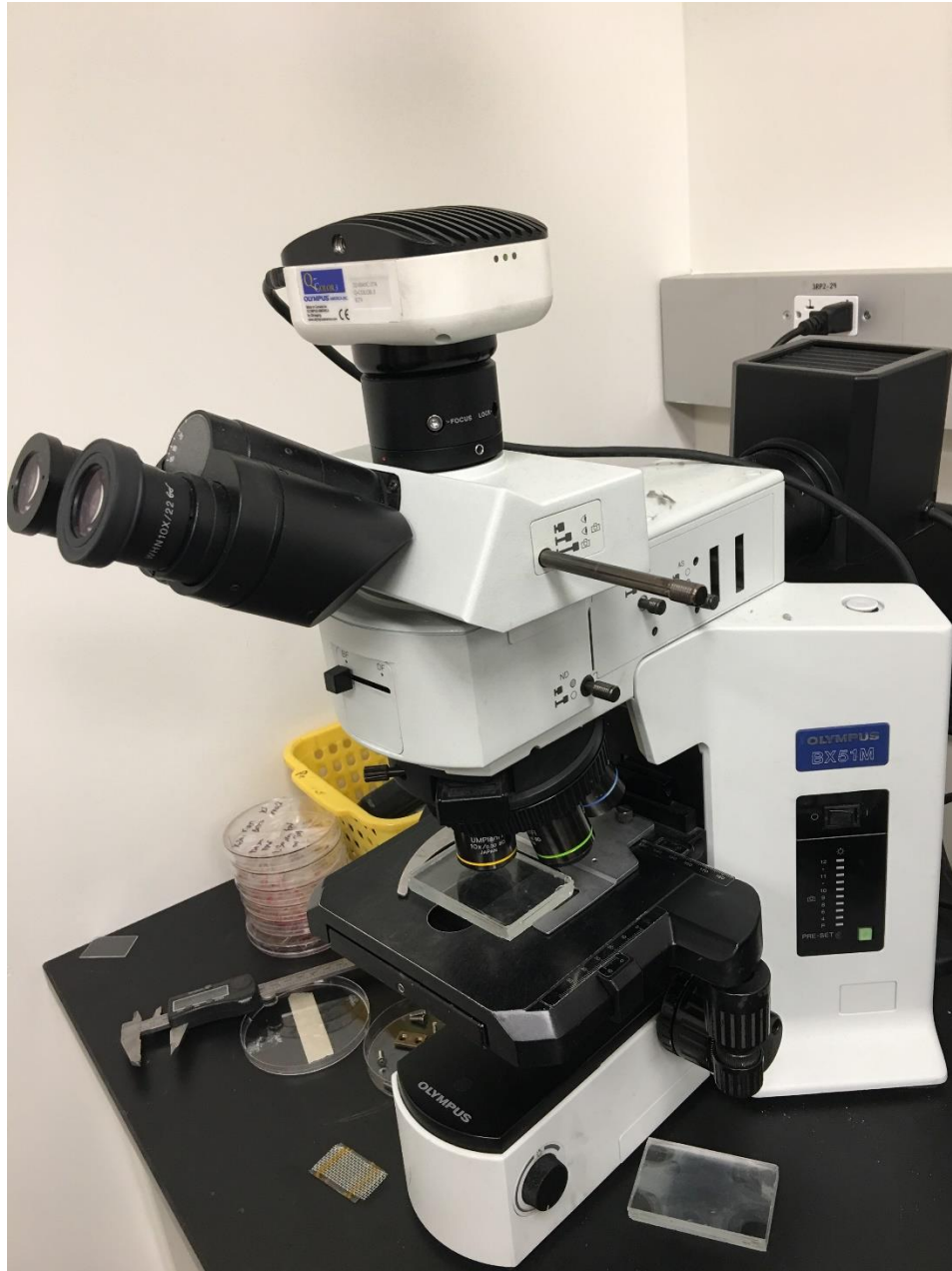


Figure 3-15. Microscopy.

## CHAPTER 4

### One Step Fast Synthesized Foam-like Amorphous $\text{Co}(\text{OH})_2$ Flexible Film on Ti Foil by Plasma Assisted Electrolytic Deposition as a Binder-free Anode of High Capacity Lithium Ion Battery

#### ***4.1 Introduction***

Lithium ion battery (LIB) as an energy storage system for portable devices and automobile industry has attracted huge research interest.[1] To achieve high lithium ion storage, researchers started focusing on developing anode materials of LIB by nanotechnologies; for instance, anode nanomaterials such as  $\text{Co}_3\text{O}_4$ ,  $\text{CoO}$  with different structures (nanowire and nanoparticles) have been prepared or combined with graphene.[2-4] Although those nanomaterials exhibited high capacity, the lengthy manufacture time and high cost likely limit their commercial applications, and they have to be mixed with binder and adhesive in LIB manufacture.<sup>3</sup> Besides their extra cost, the binder may decompose in long term and weaken ion diffusion and thus depreciate the capacity of LIB.[5] Therefore, development of binder-free low-cost flexible electrode is desirable.[6]

The  $\text{Co}(\text{OH})_2$  which was previously studied for supercapacitor applications,[7] was recently discovered to be a good candidate of anode materials for LIB.[8] As for phase structures, amorphous active materials are found beneficial to improve specific capacities over a wide potential window of LIB because of short-range structural ordering and ability to accommodate lattice distortions without phase transitions.[9]

The plasma electrolytic deposition (PED) as a surface coating technology has been used to grow oxide ceramic coatings on Mg, Al and Ti for wear resistance and corrosion prevention.[10] In this research, the plasma assisted electrolytic deposition as a modified

PED was innovatively used for one step preparation of an amorphous  $\text{Co(OH)}_2$  flexible film on a Ti foil (Figure 4-1c) as an inexpensive active anode material, where a Ti foil (Figure 4-1a) was immersed in a Co-containing aqueous solution and applied with high current and voltage (Figure 4-1b) to generate plasma discharges, leading to the formation of amorphous  $\text{Co(OH)}_2$  on Ti surface.

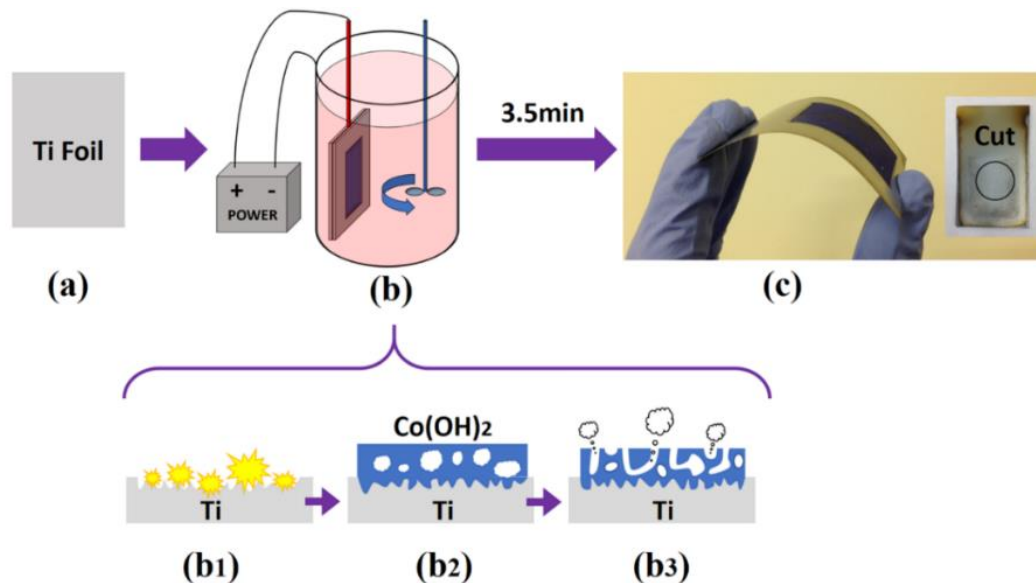


Figure 4-1. Schematic illustration of experimental process (a-c), growth of  $\text{Co(OH)}_2$  on Ti foil by plasma assisted electrolytic deposition (b<sub>1</sub>-b<sub>3</sub>).

## 4.2 Experimental section

### 4.2.1 Synthesis of amorphous $\text{Co(OH)}_2$ on Ti foil

20g/L  $(\text{CH}_3\text{COO})_2\text{Co}$  (Sigma Aldrich, 98%) was dissolved in deionized water as an electrolyte used for plasma assisted electrolytic deposition process, and then  $\text{H}_3\text{PO}_4$  (Sigma Aldrich, 85%) was added into the electrolyte to adjust PH around 5. A titanium foil (Sigma Aldrich, 0.0127mm) (Figure 1a) was cut to fit the size of fixture that makes sure only one side of the Ti foil was exposed to the electrolyte. The fixture with the Ti sample was dipped into the electrolyte contained in a stainless-steel tank. The Ti sample

and the tank were connected to a DC power supplier to its positive terminal and negative terminal, respectively (Figure 1b). When a 3A current was applied, the plasma discharging was generated on the Ti foil surface where the plasma assisted electrolytic deposition process took place. During the process, the electrolyte was stirred for even solution temperature distribution. The plasma assisted electrolytic deposition was conducted for 3.5min, leading to form a flexible  $\text{Co(OH)}_2$  film on the Ti foil (Figure 1c). The sample was subsequently washed by 1L deionized water and vacuum dried at 50 °C.

#### ***4.2.2 Structural Characterization***

Structural determination was performed using X-ray diffraction (XRD, PROTO AXRD) and X-ray photoelectron spectroscopy (XPS, Kratos Axis Nova), and the microstructures were analyzed using scanning electron microscopy (SEM, FEI Quanta 200 Environmental SEM).

#### ***4.2.3 Electrochemical Measurements***

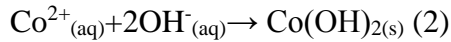
For the preparation of coin half-cell sample, a lithium chip (Sigma Aldrich, thickness-0.75mm) used as the counter electrode (D-16mm), a porous composite of polypropylene (PP) and polyethylene (PE) (MTI Crop) as the separator (D-19mm), the  $\text{Co(OH)}_2$  on the Ti foil as the working electrode (D-16mm), a copper foil (Sigma Aldrich, thickness-25 $\mu\text{m}$ ) as current collector (D-16mm), and  $\text{LiPF}_6$  as electrolyte (Sigma Aldrich, EC:DMC 1:1) were sealed into a CR2032 coin cell case (MTI Crop) with the operation in an Argon gas glove box (LABmaster 130). For the electrochemical testing, cycling performance, galvanostatic cycling profiles and rate capability were measured using a LAND battery testing system (CT2001A), and the cyclic voltammetry (CV) test was performed by an electrochemical work-station (Bio-logic).

### ***4.3 Results and discussions***

The growth process of Co(OH)<sub>2</sub> on Ti foil by the plasma assisted electrolytic deposition is schematically shown in Figure 4-1b<sub>1</sub>-b<sub>3</sub>. As the Figure 1b<sub>1</sub> shows, when the current (voltage up to 500V) is introduced, numerous plasma discharging sparks with core temperature 5000-6000K formed on the Ti surface would melt the Ti surface spot by spot,[11] and dissociate the H<sub>2</sub>O.[10]



Although in the weak acidic electrolyte, this reaction still can be carried out because the anode reaction in plasma assisted electrolytic deposition is different with normal electrolysis of water. In plasma reaction, the formation of OH<sup>-</sup> is due to the high temperature plasma discharging-induced H<sub>2</sub>O decomposition.[12,13] The OH<sup>-</sup> will combine with Co<sup>2+</sup> by high temperature plasma, and the reaction is:[14]



Subsequently, the Co(OH)<sub>2</sub> starts growing on the Ti substrate, and some gas vapor formed in the plasma can be trapped in the Co(OH)<sub>2</sub> melt (Figure 4-1b<sub>2</sub>), and then these small gas mass spits out to cause the formation of pores and channels in the Co(OH)<sub>2</sub> coating (Figure 4-1b<sub>3</sub>).[13]

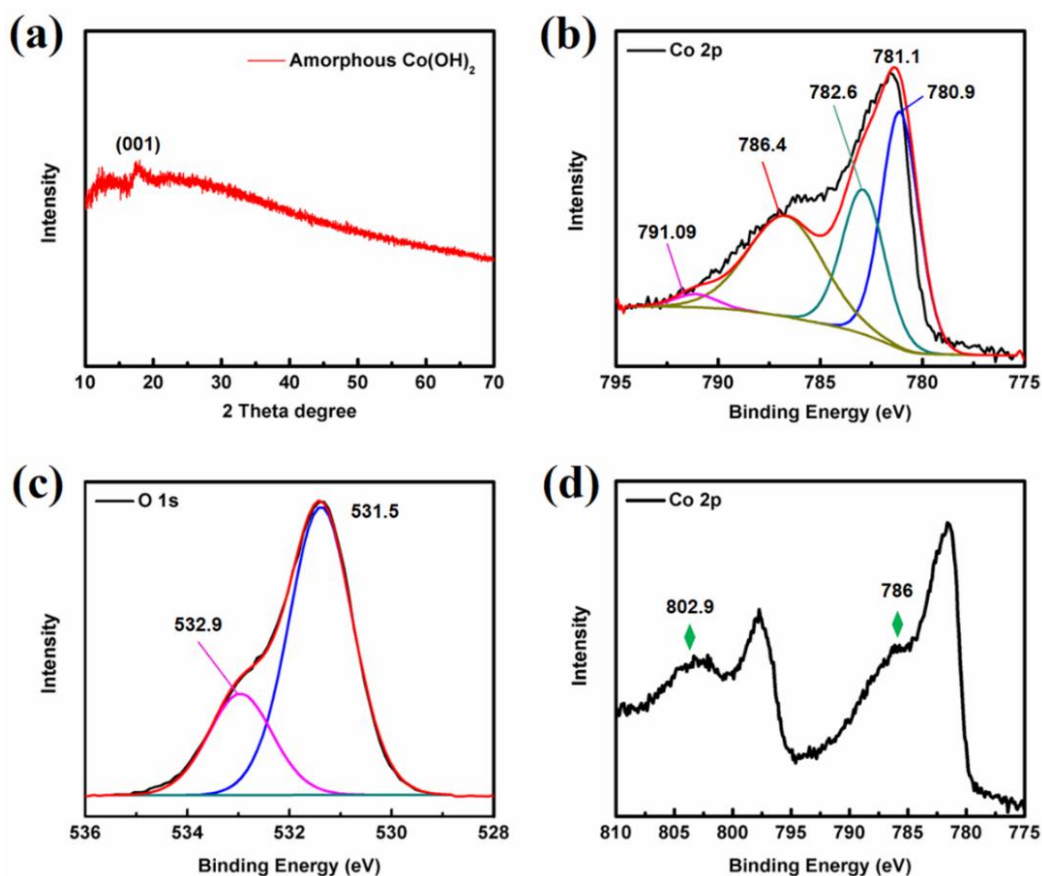


Figure 4-2. (a) XRD pattern, XPS spectra of (b) Co 2p and (c) O 1s, (d) expanded Co 2p spectrum.

From the XRD pattern (Figure 4-2a), it seems that the  $\text{Co(OH)}_2$  on Ti foil is amorphous structure, and only one weak peak at 19 two theta degrees might be attributed to the (001) crystal plane of  $\beta\text{-Co(OH)}_2$ .<sup>[15]</sup> To further determine the structure, it is necessary to analyze it by XPS. The XPS data has been shown in Figure 4-2b-c. In Figure 4-2b, the peak on 781.1 eV can be attributed to Co 2p<sub>3/2</sub> of  $\text{Co(OH)}_2$ .<sup>[14]</sup> In Figure 4-2c, two peaks at 531.5 eV and 532.9 eV observed in O 1s spectrum represent the bound hydroxide groups and the structural water in  $\text{Co(OH)}_2$ .<sup>[14,16]</sup> The peaks at 786 eV and 802.9 eV in expanded Co 2p spectrum (Figure 4-2d) are the satellite peaks of  $\text{Co(OH)}_2$  that are the certification of presence of  $\text{Co}^{2+}$  oxidation state.<sup>[14,17]</sup> Therefore, according

to the analysis of XPS data, it has clearly indicated that our flexible film on Ti substrate is  $\text{Co}(\text{OH})_2$ , and the formation of amorphous phase can be explained as the quenching process that the high temperature plasma spark would melt  $\text{Co}(\text{OH})_2$  which is then fast cooled by electrolyte without enough time for crystallization. Similar phenomena can be seen in fast solidification for preparation of an amorphous alloy in metal casting.<sup>18</sup>

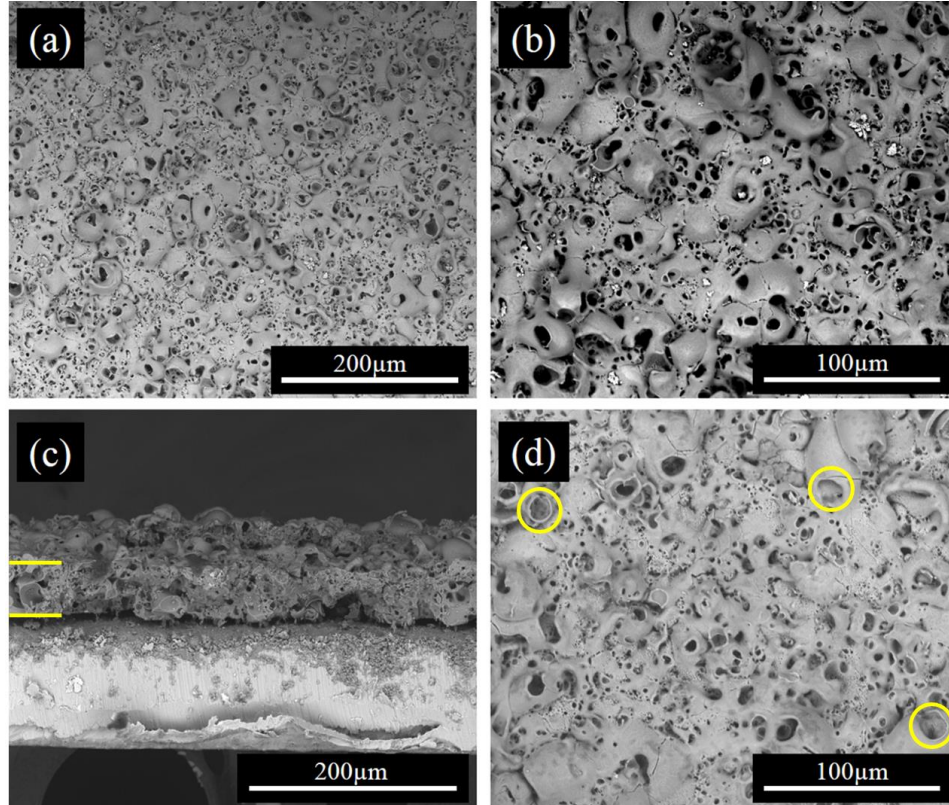


Figure 4-3. The surface SEM images of  $\text{Co}(\text{OH})_2$  on Ti substrate, (a-b) surface structure, (c) cross sectional structure and (d) surface structure after 50 charging-discharging process.

Morphologies of  $\text{Co}(\text{OH})_2$  are shown by SEM images in Figure 4-3. Figure 4-3a indicates that the  $\text{Co}(\text{OH})_2$  film contains high density of porous structures. Under a higher magnification (Figure 4-3b), some volcanic vent liked pores can be obviously seen. This is because the squirting process of gas mass brings out the  $\text{Co}(\text{OH})_2$  melt which deposit



around pores in plasma assisted electrolytic deposition process.[13] Cross-sectional image (Figure 4-3c) shows the thickness of  $\text{Co(OH)}_2$  film on Ti substrate (bright area) is 50  $\mu\text{m}$ , and the cross-section has pores and multiple channels with foam-like structure. The porosity of  $\text{Co(OH)}_2$  film is around 36.5% (Figure S4-1). After 50 charge-discharge cycles, the pores in Figure 4-3d turn to be smaller and shallower than those in Figure 4-3b, however, the general porous structure has unobvious change and the integrated film is also kept porous structure without exfoliation.

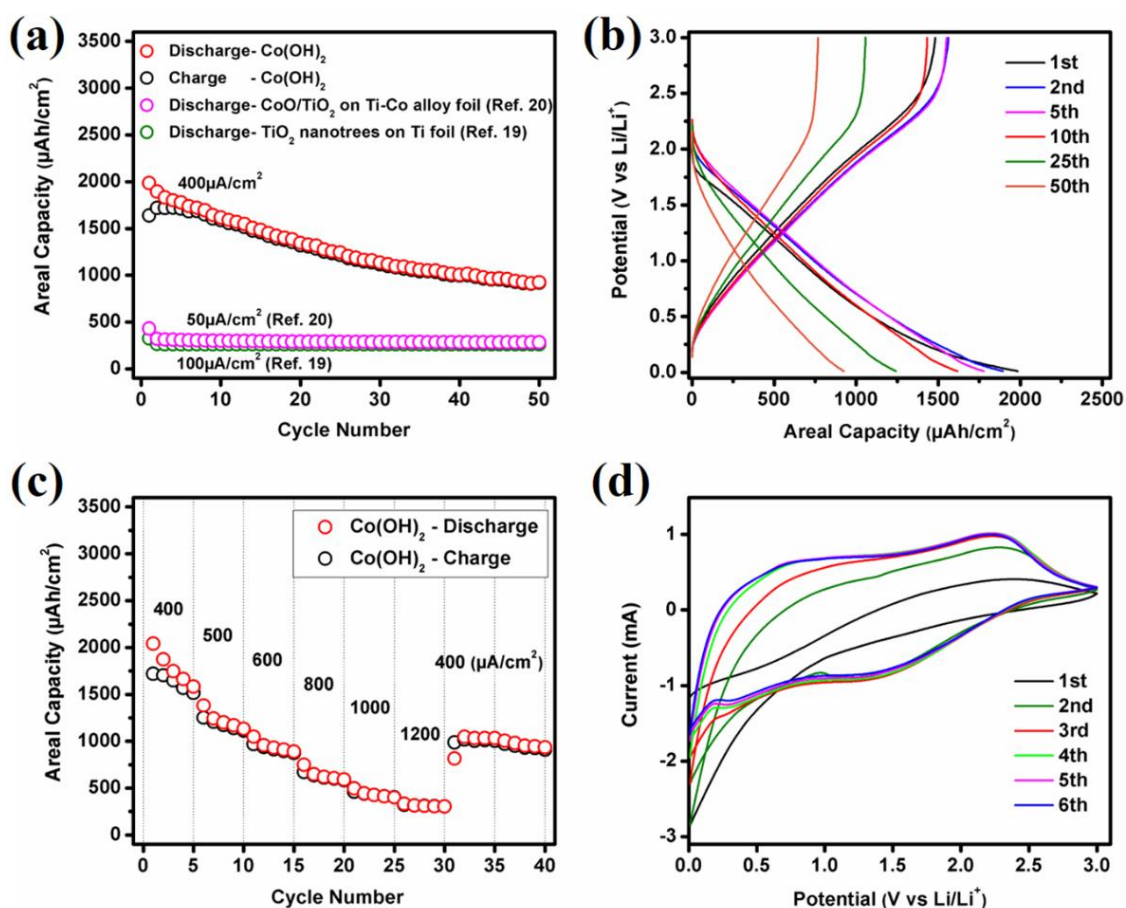
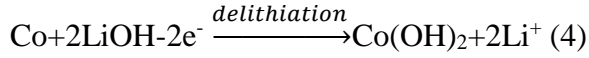
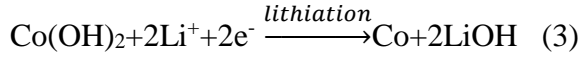


Figure 4-4. Electrochemical testing of  $\text{Co(OH)}_2$  anode in lithium ion battery, (a) cycling performance (0-3V, 400  $\mu\text{A}/\text{cm}^2$ ), (b) galvanostatic cycling profiles (0-3V, 400  $\mu\text{A}/\text{cm}^2$ ), (c) rate capability and (d) cyclic voltammetry (0.1mV/s).



The electrochemical testing results are shown in Figure 4-4a-d. In Figure 4-4a, the cycling performance at current density  $400 \mu\text{A}/\text{cm}^2$  indicates that initial discharge capacity arrived to  $2000 \mu\text{Ah}/\text{cm}^2$ , and at the last 5 cycles of the test, the capacity still kept at  $930 \mu\text{Ah}/\text{cm}^2$ . This result is higher than other reported areal discharge capacity of binder free  $\text{TiO}_2$  nanotree and  $\text{TiO}_2/\text{CoO}$  nanotube anode materials on Ti and Ti-Co alloy foil.[19,20] The high areal capacity can be explained as the large area of pores connected to numerous internal channels in the  $\text{Co}(\text{OH})_2$  film (Figure 4-3b-c), which provides enough lithium ion diffusion paths in the charge-discharge process that warrants the lithium ions to effectively react with  $\text{Co}(\text{OH})_2$ . The degradation of capacity at late stage might be due to the partially blocking to ion diffusion path in pores (Figure 4-3d) during intercalation and deintercalation of lithium ion. The galvanostatic cycling profiles (Figure 4-4b) show that the initial discharge capacity is higher than initial charge capacity by  $350 \mu\text{Ah}/\text{cm}^2$ , which is due to formation of solid electrolyte interface (SEI).[21] After 10 cycles, the columbic efficiency kept at 98%. In Figure 4-4c, the rate capability shows that even if the testing current density is  $1200 \mu\text{A}/\text{cm}^2$ , the discharge capacity still kept at  $250 \mu\text{Ah}/\text{cm}^2$ . The discharge capacity of the last 10 cycles under  $400 \mu\text{A}/\text{cm}^2$  came back to  $1000 \mu\text{Ah}/\text{cm}^2$  that is coincident with the result in Figure 4a. Such a result indicates that our  $\text{Co}(\text{OH})_2$  film anode has a good rate capability. The cyclic voltammetry (CV) curve is exhibited by Figure 4-4d where the CV curve started to overlap after two cycles. The enlarged scanning area in subsequent cycles compared with first two cycles can be explained by the activation process.[22] After two cycles, the peak at 2.15V in the anodic process is corresponding to reaction of Co to  $\text{Co}(\text{OH})_2$ , and 1.1V in the cathodic process

is corresponding to reaction of  $\text{Co(OH)}_2$  to  $\text{Co}$ . [23] Therefore, the conversion reactions of  $\text{Co(OH)}_2$  in the lithium ion battery can be written as follows: [8]



It is noted that the CV curve shape of amorphous  $\text{Co(OH)}_2$  is not very similar to the crystalline  $\text{Co(OH)}_2$  CV shape. [23] The slight changes of position of anodic and cathodic peaks of amorphous  $\text{Co(OH)}_2$  compared with crystalline  $\text{Co(OH)}_2$  is because the long term disorder of amorphous  $\text{Co(OH)}_2$  is more flexible for lithiation and delithiation. [24] The broadened anodic and cathodic peaks are attributed to amorphous  $\text{Co(OH)}_2$  that can sustain a higher stress/strain than crystalline  $\text{Co(OH)}_2$  in charging-discharging process. [25] This is also beneficial to the high areal capacity.

#### **4.4 Conclusions**

In this research work, the  $\text{Co(OH)}_2$  film was prepared on a Ti foil using a plasma assisted electrolytic deposition technique within only 3.5 min. The XRD and XPS analyses suggest that the active materials film is amorphous  $\text{Co(OH)}_2$ . SEM observations identify the foam-like structure with large number of pores and internal channels. This type of structure offered enormous surface areas and lithium ion diffusion paths and thus high cycling capacity. The results indicate that our fast manufacturing process can produce a porous amorphous  $\text{Co(OH)}_2$  flexible film on a Ti foil, which can be used as a binder and adhesive free anode material for a low-cost and high-performance lithium ion battery. However, the degradation of cycling capacity needs to be addressed in future research.

## REFERENCES

- [1] Armand, Michel, and J-M. Tarascon. "Building better batteries." *Nature* 451, no. 7179 (2008): 652.
- [2] Li, Yanguang, Bing Tan, and Yiyang Wu. "Mesoporous  $\text{Co}_3\text{O}_4$  nanowire arrays for lithium ion batteries with high capacity and rate capability." *Nano letters* 8, no. 1 (2008): 265-270.
- [3] Sun, Xiaolei, Guang-Ping Hao, Xueyi Lu, Lixia Xi, Bo Liu, Wenping Si, Chuansheng Ma et al. "High-defect hydrophilic carbon cuboids anchored with Co/CoO nanoparticles as highly efficient and ultra-stable lithium-ion battery anodes." *Journal of Materials Chemistry A* 4, no. 26 (2016): 10166-10173.
- [4] Wu, Zhong-Shuai, Wencai Ren, Lei Wen, Libo Gao, Jinping Zhao, Zongping Chen, Guangmin Zhou, Feng Li, and Hui-Ming Cheng. "Graphene anchored with  $\text{Co}_3\text{O}_4$  nanoparticles as anode of lithium ion batteries with enhanced reversible capacity and cyclic performance." *ACS nano* 4, no. 6 (2010): 3187-3194.
- [5] Tang, Xuan, Feilong Yan, Yuehua Wei, Ming Zhang, Taihong Wang, and Tianfang Zhang. "Encapsulating  $\text{Sn}_x\text{Sb}$  nanoparticles in multichannel graphene-carbon fibers as flexible anodes to store lithium ions with high capacities." *ACS applied materials & interfaces* 7, no. 39 (2015): 21890-21897.
- [6] Zhang, Ming, Feilong Yan, Xuan Tang, Qiuhong Li, Taihong Wang, and Guozhong Cao. "Flexible CoO-graphene-carbon nanofiber mats as binder-free anodes for lithium-ion batteries with superior rate capacity and cyclic stability." *Journal of Materials Chemistry A* 2, no. 16 (2014): 5890-5897.
- [7] Bao, Lin, Tao Li, Shu Chen, Yikuan He, Chang Peng, Ling Li, Qian Xu, Encai Ou, and Weijian Xu. "Electronic channel in 3D flowery  $\text{Co}(\text{OH})_2/\text{N}$ -doped graphene composites with Enhanced Electrochemistry Performance." *Materials Letters* 185 (2016): 72-76.

- [8] He, Yu-Shi, Da-Wei Bai, Xiaowei Yang, Jun Chen, Xiao-Zhen Liao, and Zi-Feng Ma. "A  $\text{Co}(\text{OH})_2$ -graphene nanosheets composite as a high performance anode material for rechargeable lithium batteries." *Electrochemistry Communications* 12, no. 4 (2010): 570-573.
- [9] Mathew, Vinod, Sungjin Kim, Jungwon Kang, Jihyeon Gim, Jinju Song, Joseph Paul Baboo, Wangeun Park et al. "Amorphous iron phosphate: potential host for various charge carrier ions." *NPG Asia Materials* 6, no. 10 (2014): e138.
- [10] Walsh, F. C., C. T. J. Low, R. J. K. Wood, K. T. Stevens, J. Archer, A. R. Poeton, and A. Ryder. "Plasma electrolytic oxidation (PEO) for production of anodised coatings on lightweight metal (Al, Mg, Ti) alloys." *Transactions of the IMF* 87, no. 3 (2009): 122-135.
- [11] Hussein, R. O., D. O. Northwood, and X. Nie. "Coating growth behavior during the plasma electrolytic oxidation process." *Journal of Vacuum Science & Technology A: Vacuum, Surfaces, and Films* 28, no. 4 (2010): 766-773.
- [12] Hussein, R. O., X. Nie, and D. O. Northwood. "An investigation of ceramic coating growth mechanisms in plasma electrolytic oxidation (PEO) processing." *Electrochimica Acta* 112 (2013): 111-119.
- [13] Hussein, Riyadh Omran. "Plasma Process Control for Improved PEO Coatings on Magnesium Alloys." (2015).
- [14] Sayeed, Md Abu, Tenille Herd, and Anthony P. O'Mullane. "Direct electrochemical formation of nanostructured amorphous  $\text{Co}(\text{OH})_2$  on gold electrodes with enhanced activity for the oxygen evolution reaction." *Journal of Materials Chemistry A* 4, no. 3 (2016): 991-999.
- [15] Sampanthar, Jeyagowry T., and Hua Chun Zeng. "Arresting butterfly-like intermediate nanocrystals of  $\beta\text{-Co}(\text{OH})_2$  via ethylenediamine-mediated synthesis." *Journal of the American Chemical Society* 124, no. 23 (2002): 6668-6675.

- [16] Xue, Tong, Xin Wang, and Jong-Min Lee. "Dual-template synthesis of  $\text{Co}(\text{OH})_2$  with mesoporous nanowire structure and its application in supercapacitor." *Journal of Power Sources* 201 (2012): 382-386.
- [17] Biesinger, Mark C., Brad P. Payne, Andrew P. Grosvenor, Leo WM Lau, Andrea R. Gerson, and Roger St C. Smart. "Resolving surface chemical states in XPS analysis of first row transition metals, oxides and hydroxides: Cr, Mn, Fe, Co and Ni." *Applied Surface Science* 257, no. 7 (2011): 2717-2730.
- [18] Inoue, Akihisa. "Stabilization of metallic supercooled liquid and bulk amorphous alloys." *Acta materialia* 48, no. 1 (2000): 279-306.
- [19] Wen, Wei, Jin-Ming Wu, Yin-Zhu Jiang, Jun-Qiang Bai, and Lu-Lu Lai. "Titanium dioxide nanotrees for high-capacity lithium-ion microbatteries." *Journal of Materials Chemistry A* 4, no. 27 (2016): 10593-10600.
- [20] Madian, M., L. Giebeler, M. Klose, T. Jaumann, M. Uhlemann, A. Gebert, S. Oswald, N. Ismail, A. Eychmuller, and J. Eckert. "Self-organized  $\text{TiO}_2/\text{CoO}$  nanotubes as potential anode materials for lithium ion batteries." *ACS Sustainable Chemistry & Engineering* 3, no. 5 (2015): 909-919.
- [21] Ni, Shibing, Xiaohu Lv, Tao Li, Xuelin Yang, and Lulu Zhang. "The investigation of  $\text{Ni}(\text{OH})_2/\text{Ni}$  as anodes for high performance Li-ion batteries." *Journal of Materials Chemistry A* 1, no. 5 (2013): 1544-1547.
- [22] Zhou, Min, Yang Xu, Chengliang Wang, Qianwen Li, Junxiang Xiang, Liying Liang, Minghong Wu, Huaping Zhao, and Yong Lei. "Amorphous  $\text{TiO}_2$  inverse opal anode for high-rate sodium ion batteries." *Nano Energy* 31 (2017): 514-524.
- [23] Bai, Yulin, Wenxiu Liu, Chunhui Yu, Ting Wang, Jinkui Feng, and Shenglin Xiong. "One-Pot Solvothermal Synthesis of  $\text{ZnO}@ \alpha\text{-Co}(\text{OH})_2$  Core-Shell Hierarchical Microspheres with Superior Lithium Storage Properties." *The Journal of Physical Chemistry C* 120, no. 5 (2016): 2984-2992.

[24] Jiang, Yinzhu, Dan Zhang, Yong Li, Tianzhi Yuan, Naoufal Bahlawane, Chu Liang, Wenping Sun, Yunhao Lu, and Mi Yan. "Amorphous  $\text{Fe}_2\text{O}_3$  as a high-capacity, high-rate and long-life anode material for lithium ion batteries." *Nano Energy* 4 (2014): 23-30.

[25] Guo, Juchen, Qing Liu, Chunsheng Wang, and Michael R. Zachariah. "Interdispersed amorphous  $\text{MnO}_x$ -carbon nanocomposites with superior electrochemical performance as lithium-storage material." *Advanced Functional Materials* 22, no. 4 (2012): 803-811.

## SUPPORTING INFORMATION

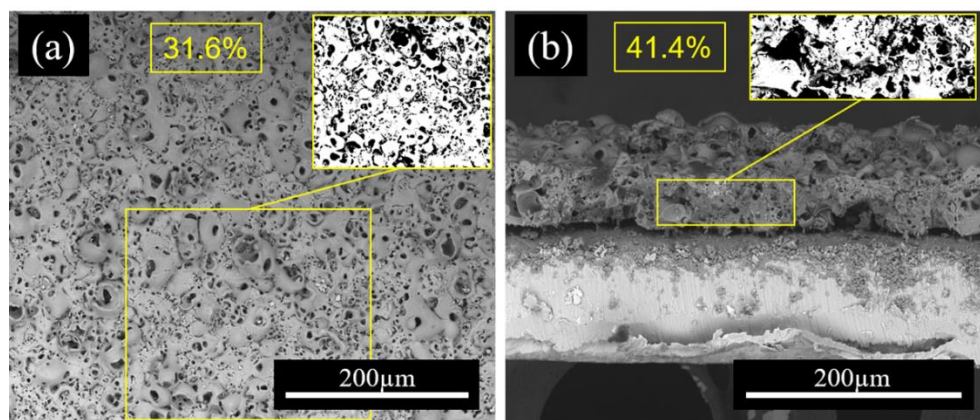


Figure S4-1. The SEM images of  $\text{Co(OH)}_2$  on Ti substrate (a) surface and (b) cross sectional structure, and corresponding porosity analysis (insert a and b).

The porosity analysis was carried out by an Image Software as shown in Figure S1a-b, insert. The dark area represents the area of pores. The porosity of surface area is around 31.6%, and the porosity of cross-sectional area is around 41.4%. Therefore, the porosity of  $\text{Co(OH)}_2$  can be estimated as the average 36.5%.

## CHAPTER 5

### Porous $\text{Ni}_3(\text{PO}_4)_2$ Thin Film as a Binder-free and Low-cost Anode of a High-capacity Lithium-ion Battery

#### **5.1 Introduction**

The lithium ion battery (LIB) needs further improvement in its electrochemical performance as an energy storage system to be built in future portable electronic devices and electrical vehicles [1]. Beyond the conventional graphite anodes, the development of nanotechnology makes it possible to obtain the nanostructured high-capacity anode materials, such as NiO nanotubes,  $\text{Co}_3\text{O}_4$  nanowire and Si nanowire [2-4]. However, the commonly-used methods of synthesizing nanomaterials, including the sol-gel process, the hydrothermal process and the chemical vapor deposition, require tedious preparation of raw materials, a long reaction time and a long product-washing process. With the limitation of productivity of nanomaterials, a high cost could not be avoided. Additionally, it is hard to control the size, purity and repeatability of nano-materials in the preparation process, causing the quality of products inconsistent. The mixing of binders and adhesives with powder-nanomaterials could lead to the disconnection between the active materials units in the charge/discharge cycles within a LIB [5]. These constraints restrict the wide applications of LIB when applied in automobile industries. Therefore, the objective of this study is to discover a simple and fast way to manufacture a low-cost and binder-free thin film anode for high capacity LIBs.

The plasma electrolytic deposition (PED) process, used as a surface coating technology, is utilized to grow a ceramic metal oxide coating for wear-resistance and corrosion prevention of an alloy [6-8]. In our previous report, plasma assisted electrolytic deposition (PAED), a modified PED, was initially used to obtain a  $\text{Co}(\text{OH})_2$  thin film



binder-free anode of LIB [9]. However, the Cobalt-containing substance requires rare Cobalt resources, and there is a great need of making Cobalt-free electrodes for LIBs.

Metal phosphate was considered as an anode material for LIB due to the presence of spectator atom “P” which can prevent the aggregation of metal atoms during the cycling [10]. In this work, the  $\text{Ni}_3(\text{PO}_4)_2$ , a former candidate of supercapacitor material [11], was proposed to be the anode material of LIB. A porous  $\text{Ni}_3(\text{PO}_4)_2$  thin film was thus prepared as a binder-free anode on a Ti foil via PAED, and the total process time was two minutes. In contrast to our previous report on  $\text{Co}(\text{OH})_2$  [9], the thickness of  $\text{Ni}_3(\text{PO}_4)_2$  flexible thin film was one fifth the thickness of the  $\text{Co}(\text{OH})_2$  film. However, the capacity reached 50% of that of the  $\text{Co}(\text{OH})_2$ . The preparation time was 40% shorter than the preparation time of  $\text{Co}(\text{OH})_2$  (2 min vs 3.5 min). Those imply that the  $\text{Ni}_3(\text{PO}_4)_2$  film has a lighter weight, a higher mass loading capacity, a lower manufacture cost and better flexibility. XRD, XPS and SEM were used to characterize the  $\text{Ni}_3(\text{PO}_4)_2$  thin film. The electrochemical performance was investigated by an electrochemical workstation and a battery testing system.

## ***5.2 Experimental***

### ***5.2.1 Synthesis of $\text{Ni}_3(\text{PO}_4)_2$ on Ti Foil***

15-20g/L  $(\text{CH}_3\text{COO})_2\text{Ni}$  (Sigma Aldrich) and 15-20g/L  $\text{H}_3\text{PO}_4$  (Sigma Aldrich) were dissolved in deionized water as an electrolyte. A Ti Foil with thickness 0.127mm (Sigma Aldrich) was masked by a fixture to ensure that only one side was exposed to the electrolyte. Then, the fixture was dipped into the electrolyte and connected with a positive terminal of pulsed DC power supply. The negative terminal was connected to a small stainless-steel plate immersed in the electrolyte. Next, a 3A current was applied and

remained for 2 minutes, forming a the deep yellow  $\text{Ni}_3(\text{PO}_4)_2$  thin film on the Ti foil. Subsequently, the coated Ti foil was taken out from the fixture and then was washed by deionized water. Lastly, the sample was dried under a temperature of 60°C.

### ***5.2.2 Structural Characterization***

The structural determination was conducted with X-ray diffraction (XRD, PROTO AXRD) and X-ray photoelectron spectroscopy (XPS, Kratos Axis Nova). The microstructure was observed using scanning electron microscopy (SEM, FEI Quanta 200 Environmental SEM).

### ***5.2.3 Preparation of coin cell***

A lithium chip (Sigma Aldrich, 0.75mm thickness) was used as the counter electrode (D-16mm), a composite film of polypropylene (PP) and polyethylene (PE) (MTI Crop.) as the separator (D-19mm), the  $\text{Ni}_3(\text{PO}_4)_2$  on the Ti foil as the working electrode (D-16mm), a copper foil (Sigma Aldrich, 25 $\mu\text{m}$  thickness) as the current collector (D-16mm), and  $\text{LiPF}_6$  as the electrolyte (Sigma Aldrich, EC:DMC 1:1) were all sealed into a CR2032 coin cell case (MTI Crop.) with the operation completed in an Argon gas glove box (LABmaster 130).

### ***5.2.4 Electrochemical testing***

Cycling performance, galvanostatic cycling profiles and rate capability were investigated by a LAND battery testing system (CT2001A), and the cyclic voltammetry (CV) was performed by an electrochemical workstation (Bio-logic).

### 5.3 Results and discussion

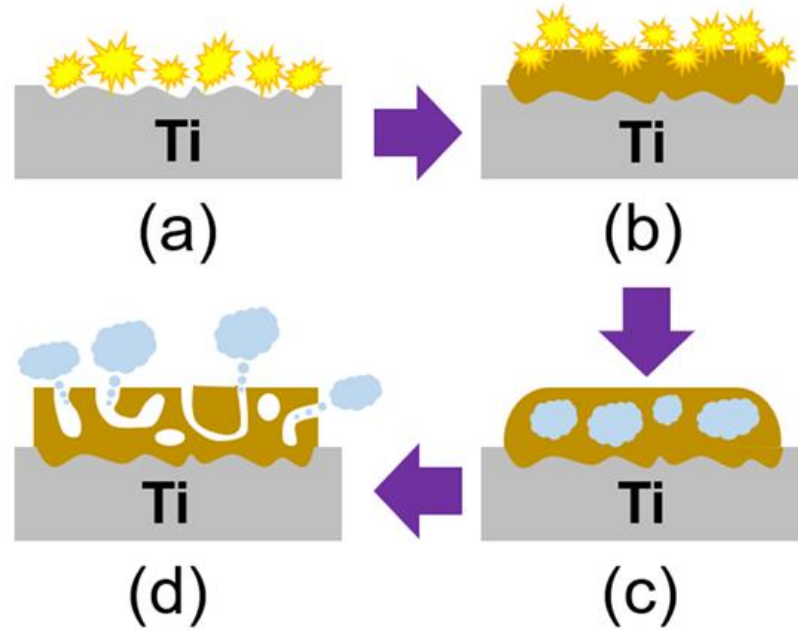


Figure 5-1. (a-d) PAED process of formation of  $\text{Ni}_3(\text{PO}_4)_2$  thin film on Ti Foil.

In the PAED process, plasma sparks were first generated on the surface of Ti foil in the Nickel-containing electrolyte under a pulse DC current, which started to melt the Ti substrate (Figure 5-1a). At the same time, the  $\text{Ni}^{2+}$  and  $(\text{PO}_4)^{3-}$  were attracted to the surface of the Ti foil via the bipolar pulse current and sintered under high temperatures of the plasma discharging (Figure 5-1b). Simultaneously, small gas mass can be sealed in the  $\text{Ni}_3(\text{PO}_4)_2$  melt (Figure 5-1c). Subsequently, some gas vapor would spit out, leaving connected pore systems on the  $\text{Ni}_3(\text{PO}_4)_2$  thin film after its solidification (Figure 4-1d).

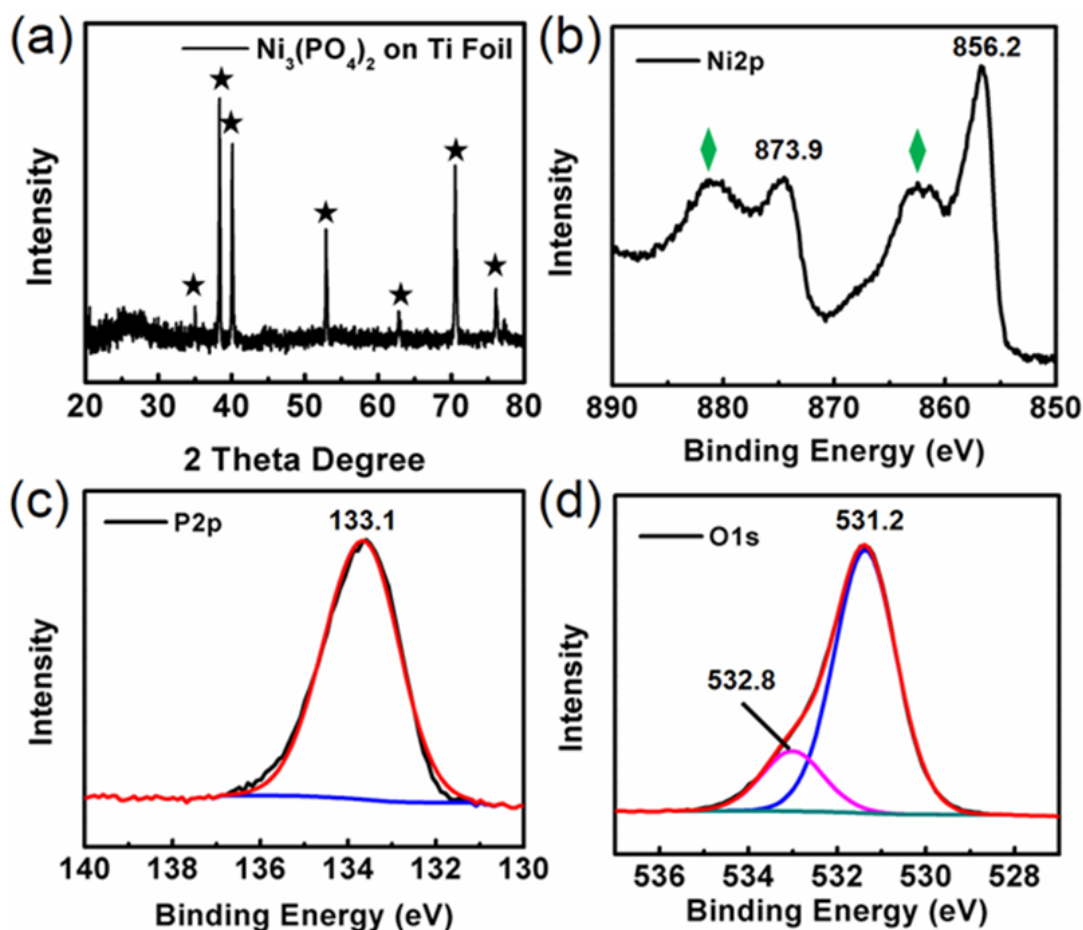


Figure 5-2. (a) X-ray diffraction pattern. (b-d) XPS spectra of (b) Ni2p, (c) P2p and (d) O1s.

According to the results of the XRD (Figure 5-2a), all peaks marked by stars can be attributed to the Ti substrate [12], and there are no peaks for the  $\text{Ni}_3(\text{PO}_4)_2$ , which reveals that the  $\text{Ni}_3(\text{PO}_4)_2$  thin film is an amorphous phase. The formation of an amorphous phase can be explained as the  $\text{Ni}_3(\text{PO}_4)_2$  film that did not have enough time to undergo crystallization under a fast cooling rate in an electrolyte [9]. The XPS was used to further identify the structure of the thin film. In Figure 5-2b, two peaks at 856.2 eV and 873.9 eV can be explained as the  $2p_{3/2}$  and  $2p_{1/2}$  splitting of  $\text{Ni}^{2+}$ , and the other two green marked satellite peaks at 862.2 eV and 880.2 eV further identify the presence of  $\text{Ni}^{2+}$ . The peak at

133.1eV in Figure 5-2c reveals P-O interactions in  $\text{Ni}_3(\text{PO}_4)_2$ . In Figure 5-2d, the strong peak at 531.2eV represents the Ni-O and P-O bounding, and the peak at 532.8eV is correspondent to structural water. These results match well with XPS of Nickel phosphate [11], indicating that the thin film on the Ti foil is indeed  $\text{Ni}_3(\text{PO}_4)_2$ .

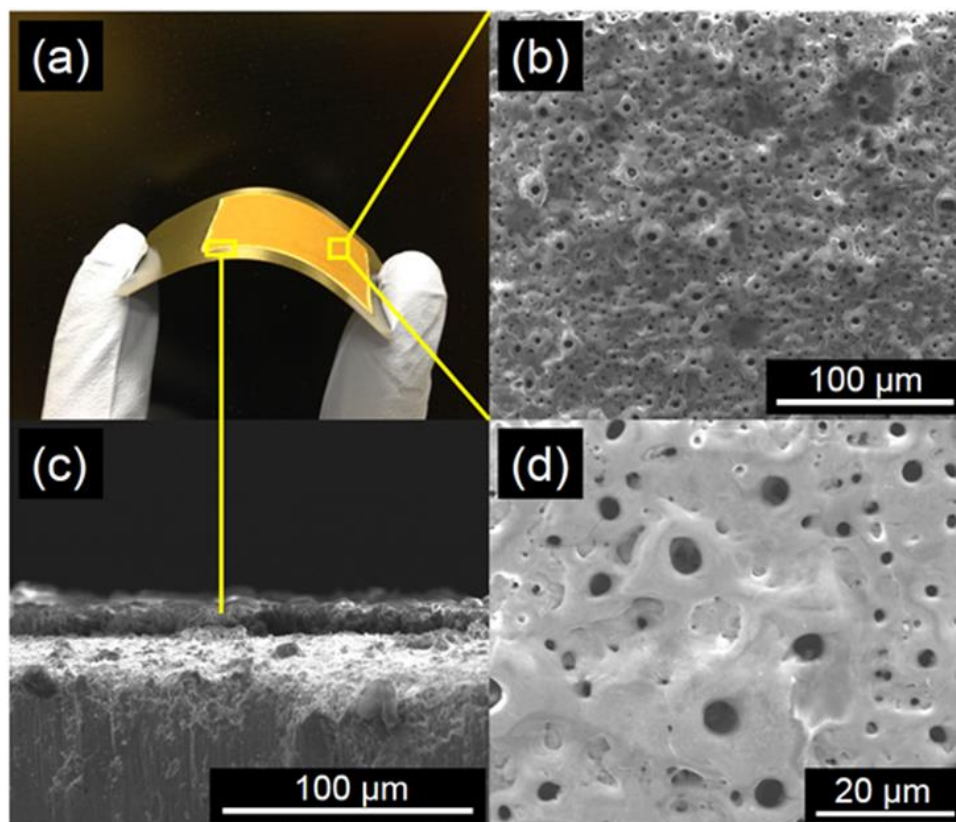


Figure 5-3. (a) Flexible  $\text{Ni}_3(\text{PO}_4)_2$  thin film photo. (b-d) SEM images of (b) surface morphology, (c) cross-sectional structure and (d) magnification of surface morphology.

Figure 5-3a is a photo which exhibits the flexibility of the binder-free  $\text{Ni}_3(\text{PO}_4)_2$  thin film anode (yellow region) on the Ti foil, where the color again suggests that the thin film is  $\text{Ni}_3(\text{PO}_4)_2$ . The surface morphology of a  $\text{Ni}_3(\text{PO}_4)_2$  thin film is shown in a SEM image in Figure 5-3b where obvious and abundant pores can be observed (Porosity: 20.54%, Figure S5-1.). The porous structure is significant for the subsequent explanation of the

high areal capacity of the  $\text{Ni}_3(\text{PO}_4)_2$  anode in LIB. In the image with a high magnification of the film's surface (Figure 5-3d), a volcanic vent-like structure can be seen around pores. This resulted from the fact that the gas mass spat out during the PEAD process which also brought the melted  $\text{Ni}_3(\text{PO}_4)_2$  out. The melted  $\text{Ni}_3(\text{PO}_4)_2$  then deposited around the pores after it cooled and solidified [9]. The thickness of the  $\text{Ni}_3(\text{PO}_4)_2$  film is around  $13\mu\text{m}$  (Figure 5-3c).

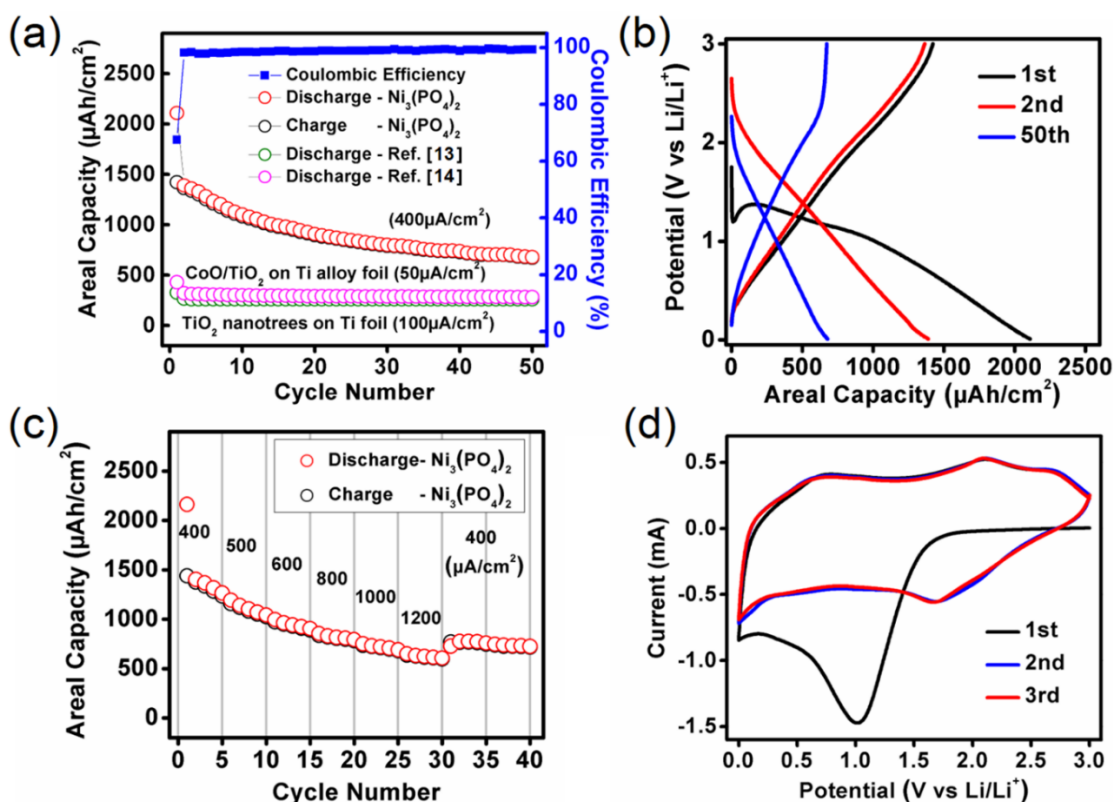


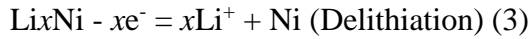
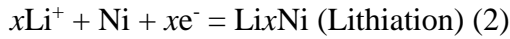
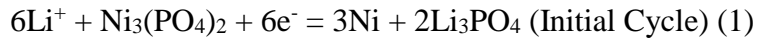
Figure 5-4. Electrochemical testing of the  $\text{Ni}_3(\text{PO}_4)_2$  anode in the LIB: (a) cycling performance and coulombic efficiency (0-3V,  $400\mu\text{A}/\text{cm}^2$ ); (b) galvanostatic cycling profiles (0-3V,  $400\mu\text{A}/\text{cm}^2$ ); (c) rate capability (0-3V); (d) CV (0.1 mV/s).

Figure 5-4a shows the cycling performance and coulombic efficiency of a  $\text{Ni}_3(\text{PO}_4)_2$  thin film anode in LIB. The reversible areal capacity reaches  $1400\mu\text{Ah}/\text{cm}^2$  (i.e.,  $310\text{mAh/g}$ ,

or 2.8 mAh for the single coin cell) and remains steady at  $750 \mu\text{Ah}/\text{cm}^2$  (i.e., 165 mAh/g, or 1.5 mAh for the cell) after 40 cycles, when the test current density is  $400 \mu\text{A}/\text{cm}^2$  (i.e., 90 mA/g, or 0.8 mA for the cell). The areal capacity performance is significantly improved, compared with the other binder-free anodes on Ti substrate as shown by the bottom two curves ( $\text{CoC}/\text{TiO}_2$  and  $\text{TiO}_2$  nanotrees) in Figure 5-4a [13, 14]. The gravimetric capacity of  $\text{Ni}_3(\text{PO}_4)_2$  is also higher than that of carbon nanotubes anode [15]. The high capacity can be attributed to the porous structure which provides sufficient diffusion paths for lithium ions during the charge/discharge process [9]. The coulombic efficiency after the initial cycle is almost 99%. Figure 5-4b shows that the initial discharge capacity can reach  $2100 \mu\text{Ah}/\text{cm}^2$ . The  $700 \mu\text{Ah}/\text{cm}^2$  loss in capacity at the first cycle can be explained through the formations of  $\text{Li}_3\text{PO}_4$  and solid electrolyte interface (SEI) [16-18]. After 50 cycles, the reduction of pore size (Figure S5-2.) was occurred to some of pores (Figure S5-2 vs. Figure 5-3d). The decreased pores partially retarded diffusions of the lithium ions in the charge/discharge process, which led to the degradation of capacity. The decrease of pore sizes was likely due to insertion-extraction of lithium ions which could cause damage to the internal structure of  $\text{Ni}_3(\text{PO}_4)_2$ .

It seems that the  $\text{Ni}_3(\text{PO}_4)_2$  thin film was robust to high current charge/discharge processes. High charge/discharge current densities (e.g.,  $500 \mu\text{A}/\text{cm}^2$  -  $1200 \mu\text{A}/\text{cm}^2$ ) did not cause obvious degradation in capacity of the  $\text{Ni}_3(\text{PO}_4)_2$  thin film, as demonstrated in Figure 5-4c vs. Figure 5-4a. Even a current density of  $1200 \mu\text{A}/\text{cm}^2$  is applied, the areal capacity can still reach  $600 \mu\text{Ah}/\text{cm}^2$ . In the last 10 cycles of the test under  $400 \mu\text{A}/\text{cm}^2$  (Figure 5-4c), the capacity returns to  $750 \mu\text{Ah}/\text{cm}^2$  which matches the data shown in Figure 5-4a. This remarkable rate capability can be explained by the long-term disordered

structure of amorphous  $\text{Ni}_3(\text{PO}_4)_2$ , which is more flexible for shuttles of lithium ions during the lithiation and delithiation under a high current density [19]. According to the CV curves in Figure 5-4d, the peak on cathodic process at 1.0V was formed due to the formation of  $\text{Li}_3\text{PO}_4$  in the irreversible reaction at the initial cycle, as well as the formation of SEI [20]. In the subsequent scan, the anodic peak at 2.1V and the cathodic peak at 1.75V can be attributed to the lithiation and delithiation associated with the reversible Li-Ni alloy reaction [21]. Based on similarity of anode reactions of Tin phosphate and  $\text{Pb}_3(\text{PO}_4)_2$  in a LIB, the electrode reactions of  $\text{Ni}_3(\text{PO}_4)_2$  in a LIB should be written as follows [21, 22]:



The broadened CV peaks of  $\text{Ni}_3(\text{PO}_4)_2$  further reveals the presence of the amorphous phase [23], and the large scanning area of the CV curve also reflects the high capacity of the  $\text{Ni}_3(\text{PO}_4)_2$  anode.

#### **5.4 Conclusion**

A porous  $\text{Ni}_3(\text{PO}_4)_2$  thin film anode was successfully fabricated using a PAED process which only needed 2 minutes as the fabricating time. The SEM observations confirm that the  $\text{Ni}_3(\text{PO}_4)_2$  thin film has a porous structure with 13 $\mu\text{m}$  film thickness and more than 20% porosity. The electrochemical testing results show that the reversible areal capacity can reach 1400  $\mu\text{Ah}/\text{cm}^2$  and remains steady at 750  $\mu\text{Ah}/\text{cm}^2$  after 40 cycles. Even a current density of 1200  $\mu\text{A}/\text{cm}^2$  is applied, the areal capacity still reaches 600  $\mu\text{Ah}/\text{cm}^2$ ,



which is higher than that of most anodes reported. The porous structure and the amorphous phase of a  $\text{Ni}_3(\text{PO}_4)_2$  film provide abundant diffusion paths for lithium ions and internal spaces for lithiation and delithiation. This work illustrates that our  $\text{Ni}_3(\text{PO}_4)_2$  film can be used as a potential binder-free, high-capacity anode material for a low-cost, rapidly manufactured lithium ion battery. However, the degradation of capacity in the early stage of cycling still need to be resolved in future research.

## REFERENCES

- [1] Armand, Michel, and J-M. Tarascon. "Building better batteries." *Nature* 451, no. 7179 (2008): 652.
- [2] Needham, Scott A., G. X. Wang, and Hua-Kun Liu. "Synthesis of NiO nanotubes for use as negative electrodes in lithium ion batteries." *Journal of Power Sources* 159, no. 1 (2006): 254-257.
- [3] Li, Yanguang, Bing Tan, and Yiyang Wu. "Mesoporous Co<sub>3</sub>O<sub>4</sub> nanowire arrays for lithium ion batteries with high capacity and rate capability." *Nano letters* 8, no. 1 (2008): 265-270.
- [4] Chan, Candace K., Riccardo Ruffo, Seung Sae Hong, and Yi Cui. "Surface chemistry and morphology of the solid electrolyte interphase on silicon nanowire lithium-ion battery anodes." *Journal of Power Sources* 189, no. 2 (2009): 1132-1140.
- [5] Wang, Zhongqi, Ming Zhang, and Ji Zhou. "Flexible NiO–Graphene–Carbon Fiber Mats Containing Multifunctional Graphene for High Stability and High Specific Capacity Lithium-Ion Storage." *ACS applied materials & interfaces* 8, no. 18 (2016): 11507-11515.
- [6] Walsh, F. C., C. T. J. Low, R. J. K. Wood, K. T. Stevens, J. Archer, A. R. Poeton, and A. Ryder. "Plasma electrolytic oxidation (PEO) for production of anodised coatings on lightweight metal (Al, Mg, Ti) alloys." *Transactions of the IMF* 87, no. 3 (2009): 122-135.
- [7] Yerokhin, A. L., X. Nie, A. Leyland, A. Matthews, and S. J. Dowey. "Plasma electrolysis for surface engineering." *Surface and coatings technology* 122, no. 2-3 (1999): 73-93.
- [8] Clyne, Trevor William, and Samuel Christopher Troughton. "A review of recent work on discharge characteristics during plasma electrolytic oxidation of various metals." *International Materials Reviews* 64, no. 3 (2019): 127-162.

- [9] Li, Tao, and Xueyuan Nie. "One-Step Fast-Synthesized Foamlike Amorphous  $\text{Co}(\text{OH})_2$  Flexible Film on Ti Foil by Plasma-Assisted Electrolytic Deposition as a Binder-Free Anode of a High-Capacity Lithium-Ion Battery." *ACS applied materials & interfaces* 10, no. 20 (2018): 16943-16946.
- [10] Kim, Eunjin, Dongyeon Son, Tae-Gon Kim, Jaephil Cho, Byungwoo Park, Kwang-Sun Ryu, and Soon-Ho Chang. "A Mesoporous/Crystalline Composite Material Containing Tin Phosphate for Use as the Anode in Lithium-Ion Batteries." *Angewandte Chemie International Edition* 43, no. 44 (2004): 5987-5990.
- [11] Padmanathan, N., Han Shao, and Kafil M. Razeeb. "Multifunctional nickel phosphate nano/microflakes 3D electrode for electrochemical energy storage, nonenzymatic glucose, and sweat pH sensors." *ACS applied materials & interfaces* 10, no. 10 (2018): 8599-8610.
- [12] Song, Yuqing, Shanshan Qin, Yangwei Zhang, Wanqin Gao, and Jinping Liu. "Large-scale porous hematite nanorod arrays: direct growth on titanium foil and reversible lithium storage." *The Journal of Physical Chemistry C* 114, no. 49 (2010): 21158-21164.
- [13] Wen, Wei, Jin-Ming Wu, Yin-Zhu Jiang, Jun-Qiang Bai, and Lu-Lu Lai. "Titanium dioxide nanotrees for high-capacity lithium-ion microbatteries." *Journal of Materials Chemistry A* 4, no. 27 (2016): 10593-10600.
- [14] Madian, M., L. Giebeler, M. Klose, T. Jaumann, M. Uhlemann, A. Gebert, S. Oswald, N. Ismail, A. Eychmuller, and J. Eckert. "Self-organized  $\text{TiO}_2/\text{CoO}$  nanotubes as potential anode materials for lithium ion batteries." *ACS Sustainable Chemistry & Engineering* 3, no. 5 (2015): 909-919.
- [15] Chen, Wei Xiang, Jim Yang Lee, and Zhaolin Liu. "The nanocomposites of carbon nanotube with Sb and  $\text{SnSb}_{0.5}$  as Li-ion battery anodes." *Carbon* 41, no. 5 (2003): 959-966.
- [16] Agubra, Victor A., Luis Zuniga, David Flores, Howard Campos, Jahaziel Villarreal, and Mataz Alcoutlabi. "A comparative study on the performance of binary  $\text{SnO}_2/\text{NiO}/\text{C}$

and Sn/C composite nanofibers as alternative anode materials for lithium ion batteries." *Electrochimica Acta* 224 (2017): 608-621.

[17] Ji, Liwen, Praveen Meduri, Victor Agubra, Xingcheng Xiao, and Mataz Alcoutlabi. "Graphene-based nanocomposites for energy storage." *Advanced Energy Materials* 6, no. 16 (2016): 1502159.

[18] Sun, Xuejiao, Changzhen Shao, Feng Zhang, Yi Li, Qi-Hui Wu, and Yonggang Yang. "SiC nanofibers as long-life lithium-ion battery anode materials." *Frontiers in chemistry* 6 (2018).

[19] Jiang, Yin Zhu, Dan Zhang, Yong Li, Tianzhi Yuan, Naoufal Bahlawane, Chu Liang, Wenping Sun, Yunhao Lu, and Mi Yan. "Amorphous Fe<sub>2</sub>O<sub>3</sub> as a high-capacity, high-rate and long-life anode material for lithium ion batteries." *Nano Energy* 4 (2014): 23-30.

[20] Sun, Xiaolei, Chenglin Yan, Yao Chen, Wenping Si, Junwen Deng, Steffen Oswald, Lifeng Liu, and Oliver G. Schmidt. "Three-Dimensionally "Curved" NiO Nanomembranes as Ultrahigh Rate Capability Anodes for Li-Ion Batteries with Long Cycle Lifetimes." *Advanced Energy Materials* 4, no. 4 (2014): 1300912.

[21] Xiao, Y. W., J. Y. Lee, A. S. Yu, and Z. L. Liu. "Electrochemical Performance of Amorphous and Crystalline Sn<sub>2</sub>P<sub>2</sub>O<sub>7</sub> Anodes in Secondary Lithium Batteries." *Journal of The Electrochemical Society* 146, no. 10 (1999): 3623-3629.

[22] Liu, Zhaolin, and Jim Yang Lee. "Electrochemical performance of Pb<sub>3</sub>(PO<sub>4</sub>)<sub>2</sub> anodes in rechargeable lithium batteries." *Journal of power sources* 97 (2001): 247-250.

[23] Guo, Juchen, Qing Liu, Chunsheng Wang, and Michael R. Zachariah. "Interdispersed amorphous MnO<sub>x</sub>-carbon nanocomposites with superior electrochemical performance as lithium - storage material." *Advanced Functional Materials* 22, no. 4 (2012): 803-811.

## SUPPORTING INFORMATION

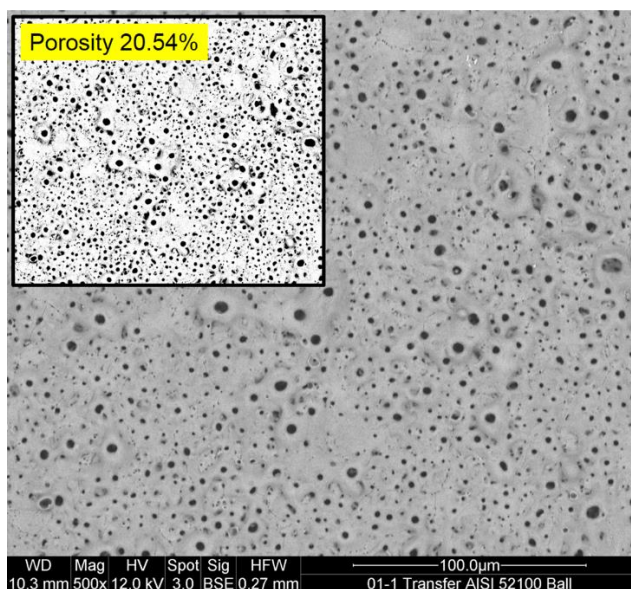


Figure S5-1. Porosity of porous  $\text{Ni}_3(\text{PO}_4)_2$  thin film.

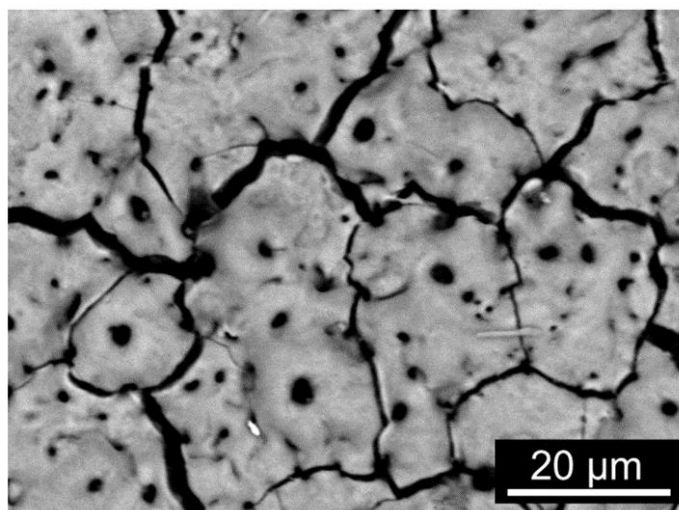


Figure S5-2. The surface morphology of  $\text{Ni}_3(\text{PO}_4)_2$  electrode after 50 cycles.

## CHAPTER 6

### Plasma-Assisted Electrolytic Deposition Synthesized Porous $\text{Ni}_3(\text{PO}_4)_2$ Thin Film: A Comparative Study of Amorphous and Crystalline $\text{Ni}_3(\text{PO}_4)_2$ Binder-Free Anodes in Lithium-Ion Batteries

#### **6.1 Introduction**

Lithium-ion battery (LIB) as an energy storage device for portable electronic products and automobile industry has attracted wide research interests.[1] Currently, graphite and silicon are most-commonly used as anode materials.[2] Much works have been carried out to improve the electrochemical performance of LIBs via advanced anode materials. Most research in the anode materials emphasizes on metal oxide and metal hydroxide, such as nano-sized  $\text{Co}_3\text{O}_4$ ,  $\text{Ni}(\text{OH})_2$  and their composites with modifications of graphene or carbon nanotubes.[3-5] Beyond these, only a few reports focus on other types of anode materials. For instance, very few papers could be found to study oxometallates and metal phosphates as active materials for LIB anodes.[6-7] The metal phosphates like  $\text{Co}_3(\text{PO}_4)_2$  and manganese phosphate have been widely investigated for applications in supercapacitors and electrocatalysts,[8-9] but they are rarely proposed to be used as anodes of LIBs. However, a few researchers still recognized that metal phosphates could be the possible candidates for LIB anodes because phosphor (P) as a spectator atom can prevent the aggregation of metal atoms during the cycling through the demonstration of Tin phosphate anode research.[10] In this research,  $\text{Ni}_3(\text{PO}_4)_2$  was selected to extend application areas of metal phosphate and provide more possible choices for anode materials of LIBs. A binder-free  $\text{Ni}_3(\text{PO}_4)_2$  porous thin film anode on a Ti foil was thus prepared using a plasma electrolytic synthesis (PES) method. Then, the crystalline  $\text{Ni}_3(\text{PO}_4)_2$  was obtained after the annealing treatment of the film which was amorphous

initially. The binder-free anodes provide a chance to clearly observe the change of electrode surface morphology before and after LIB cycles, which helps us analyze the different cycling performance between amorphous and crystalline  $\text{Ni}_3(\text{PO}_4)_2$  anodes in details based on the structural change of pores and cracks in the film. Furthermore, the rate capability and first derivative of cyclic voltammetry were also investigated to support our analysis in this comparative study.

In this work, the new plasma assisted electrolytic deposition synthesis (PAED) method was able to fabricate the porous  $\text{Ni}_3(\text{PO}_4)_2$  binder-free anodes of LIB with only 2 minutes as the synthesizing time. The high areal capacity of  $\text{Ni}_3(\text{PO}_4)_2$  indicates that the PES is a low-cost and rapid way to manufacture anodes potentially for mass production without need of those high-cost and time-consuming nanotechnologies such as sol-gel and hydrothermal methods.[11-12]

## ***6.2 Experimental section***

### ***6.2.1 Preparation of $\text{Ni}_3(\text{PO}_4)_2$ on Ti***

A Ti foil (Sigma Aldrich, thickness: 0.127mm) was immersed in an electrolyte (10-20g/L  $(\text{CH}_3\text{COO})_2\text{Ni}$  and 10-20g/L  $\text{H}_3\text{PO}_4$  in deionized water, Sigma Aldrich) held in a stainless-steel vessel. One side of the Ti foil was fully covered, and the other side was exposed to the electrolyte. Then the Ti foil and stainless-steel vessel were connected with positive and negative terminals of a power supply, respectively. Next, 3A current was applied for 2 mins to obtain an amorphous  $\text{Ni}_3(\text{PO}_4)_2$  film on Ti. Lastly, the sample was dried under 60 °C. The crystalline  $\text{Ni}_3(\text{PO}_4)_2$  sample was obtained by annealing the amorphous  $\text{Ni}_3(\text{PO}_4)_2$  film (700 °C, 3h).

### 6.2.2 Materials characterization

Phases of the films were determined by X-ray diffraction (XRD, PROTO AXRD) and X-ray photoelectron spectroscopy (XPS, Kratos Axis Nova). The microstructure observation was performed by scanning electron microscopy (SEM, Hitachi, TM 3030).

### 6.2.3 Electrochemical measurements

The  $\text{Ni}_3(\text{PO}_4)_2$  on the Ti foil served as the working electrode with lithium chip (Sigma Aldrich) as the counter electrode. Then, they were sealed into a CR2032 coin cell case (MTI Crop.) with  $\text{LiPF}_6$  electrolyte (Sigma Aldrich, EC:DMC 1:1), separator (MTI Crop.) and copper current collector (Sigma Aldrich). All the operations were completed in an Argon gas glove box (LABmaster 130). Cycling performance and rate capability were tested by a LAND battery testing system (CT2001A), and the cyclic voltammetry (CV) was performed by an electrochemical workstation (Bio-logic).

## 6.3 Results and Discussion

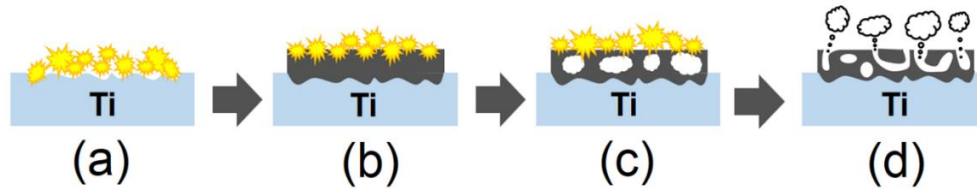
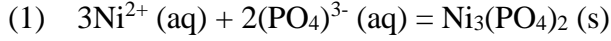


Figure 6-1. (a-d) PAED growth process of amorphous porous  $\text{Ni}_3(\text{PO}_4)_2$  thin film on Ti foil.

The PAED process for the film growth can be illustrated by Figure 6-1. Firstly, the high temperature electrical discharge sparks were generated on Ti foil and the localized surface was melted (Figure 6-1a). Then  $\text{Ni}^{2+}$  and  $(\text{PO}_4)^{3-}$  in the electrolyte gathered on the Ti surface under a bipolar power mode and reacted as follows:





At the same time, the  $\text{Ni}_3(\text{PO}_4)_2$  thin film started growing and sealed some small gas mass in the film (Figure 6-1b-c). Lastly, the gas mass spit out, leaving amorphous porous  $\text{Ni}_3(\text{PO}_4)_2$  thin film (Figure 6-1d).[13] The as-prepared sample was shown in Figure S6-1.

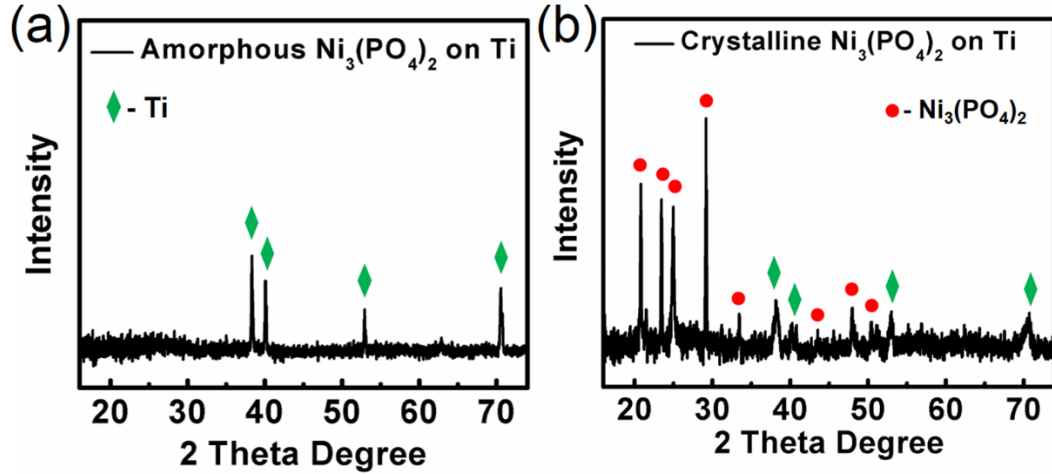


Figure 6-2. XRD pattern of (a) amorphous  $\text{Ni}_3(\text{PO}_4)_2$  and (b) crystalline  $\text{Ni}_3(\text{PO}_4)_2$ .

The XRD results of amorphous and crystalline  $\text{Ni}_3(\text{PO}_4)_2$  are shown in Figure 6-2. In Figure 6-2a, four peaks (green marks) appeared at 38°, 40°, 53° and 71° can be attributed to (002), (101), (102) and (103) crystal planes of Ti, respectively.[14] There is no peak for  $\text{Ni}_3(\text{PO}_4)_2$ , which indicates the formation of amorphous phase. XPS analysis was carried out and able to identify that the amorphous coating was  $\text{Ni}_3(\text{PO}_4)_2$  (Figure S6-2a-c). In Ni 2p spectrum (Figure S6-2a), two peaks at 856.2 eV and 873.9 eV can be explained as the splitting of  $\text{Ni}^{2+}$  on  $2p_{3/2}$  and  $2p_{1/2}$ . Two satellite peaks at 862.2 eV and 880.5 eV also indicate the presence of +2 state of Ni. In P 2p spectrum (Figure S6-2b), the peak at 133.5 eV represents the P-O interaction. Peaks at 531.2 eV and 532.9 eV in O 1s (Figure S6-2c) should be assigned to Ni-O bonding and structural water,

respectively.[15] These results reveals that the amorphous coating is  $\text{Ni}_3(\text{PO}_4)_2$ . The reason for formation of amorphous phase is similar with fast-solidification process of amorphous metal casting.[16] In Figure 6-2b, the peaks for the annealed film at  $21^\circ$ ,  $24^\circ$ ,  $25^\circ$ ,  $29^\circ$ ,  $33^\circ$ ,  $43^\circ$ ,  $49^\circ$  and  $51^\circ$  should be assigned to (110), (201), (210), (21-1), (310), (42-1), (022) and (11-3) crystal planes of  $\text{Ni}_3(\text{PO}_4)_2$ . [17] This result further illustrates that the coating on Ti is  $\text{Ni}_3(\text{PO}_4)_2$  and the crystalline phase was formed after the annealing treatment.

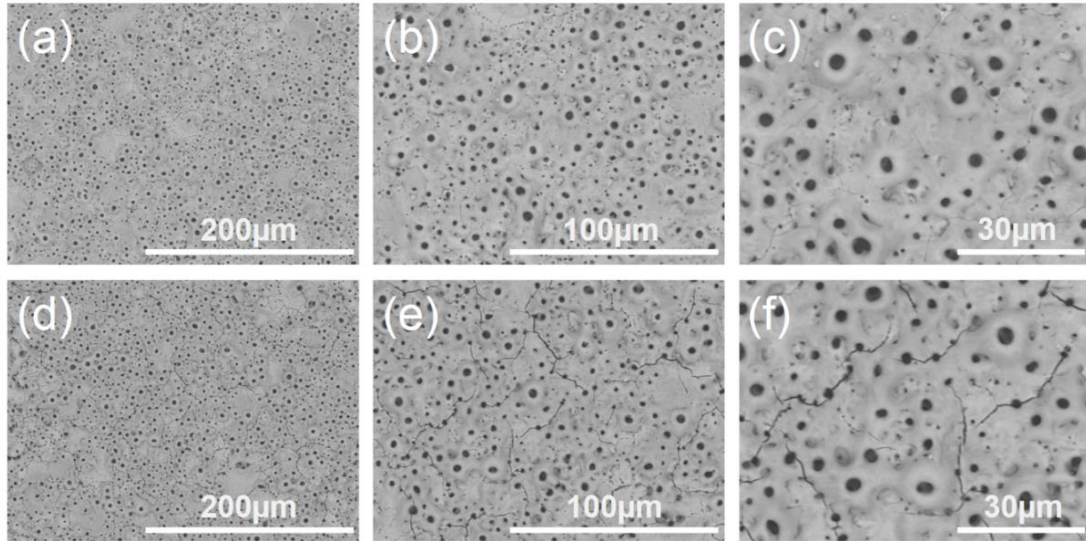


Figure 6-3. SEM images of  $\text{Ni}_3(\text{PO}_4)_2$  coatings: surface morphologies of (a-c) amorphous  $\text{Ni}_3(\text{PO}_4)_2$  coating and (d-f) crystalline  $\text{Ni}_3(\text{PO}_4)_2$  coating.

In SEM images of  $\text{Ni}_3(\text{PO}_4)_2$  coatings (Figure 6-3a-f), it can be observed that both of amorphous and crystalline  $\text{Ni}_3(\text{PO}_4)_2$  have a large quantity of pores, which are the important locations for diffusion of lithium ions in cycles of LIBs. Compared with amorphous  $\text{Ni}_3(\text{PO}_4)_2$ , the surface of crystalline  $\text{Ni}_3(\text{PO}_4)_2$  has some obvious cracks. The

formation of crack might result from the dehydration reaction in the annealing process, which can lead to the shrinkage of a ceramic film.[18]

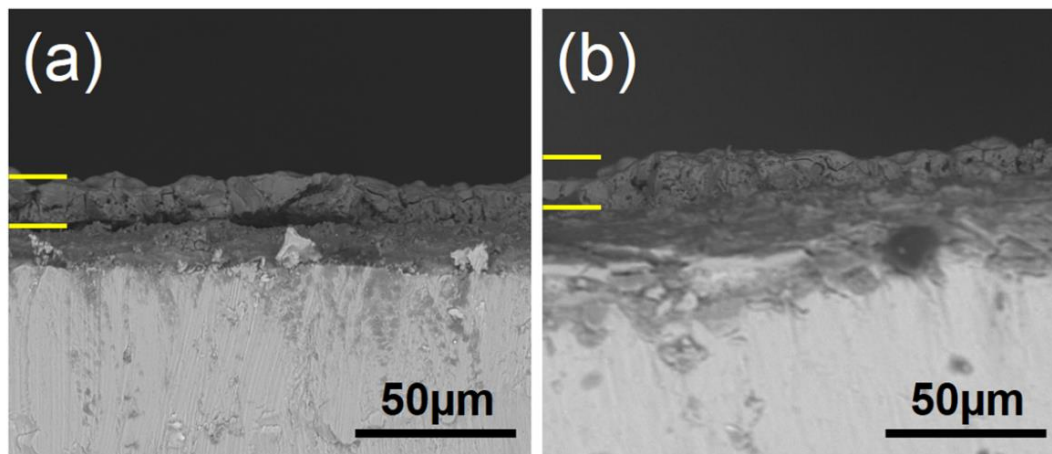


Figure 6-4. SEM images of  $\text{Ni}_3(\text{PO}_4)_2$  coatings: (a) cross-sectional morphologies of amorphous  $\text{Ni}_3(\text{PO}_4)_2$  coating and (b) crystalline  $\text{Ni}_3(\text{PO}_4)_2$  coating.

According to the cross-sectional morphology (Figure 6-4a-b), the thicknesses of both amorphous and crystalline  $\text{Ni}_3(\text{PO}_4)_2$  are approximately  $13\mu\text{m}$ . It can also be observed that there are numerous pores along the cross-sections. This phenomenon indicates that pores on  $\text{Ni}_3(\text{PO}_4)_2$  were not isolated but formed a connected channel system structure in the film. This structure is significant for high-capacity of  $\text{Ni}_3(\text{PO}_4)_2$  anodes in LIBs.

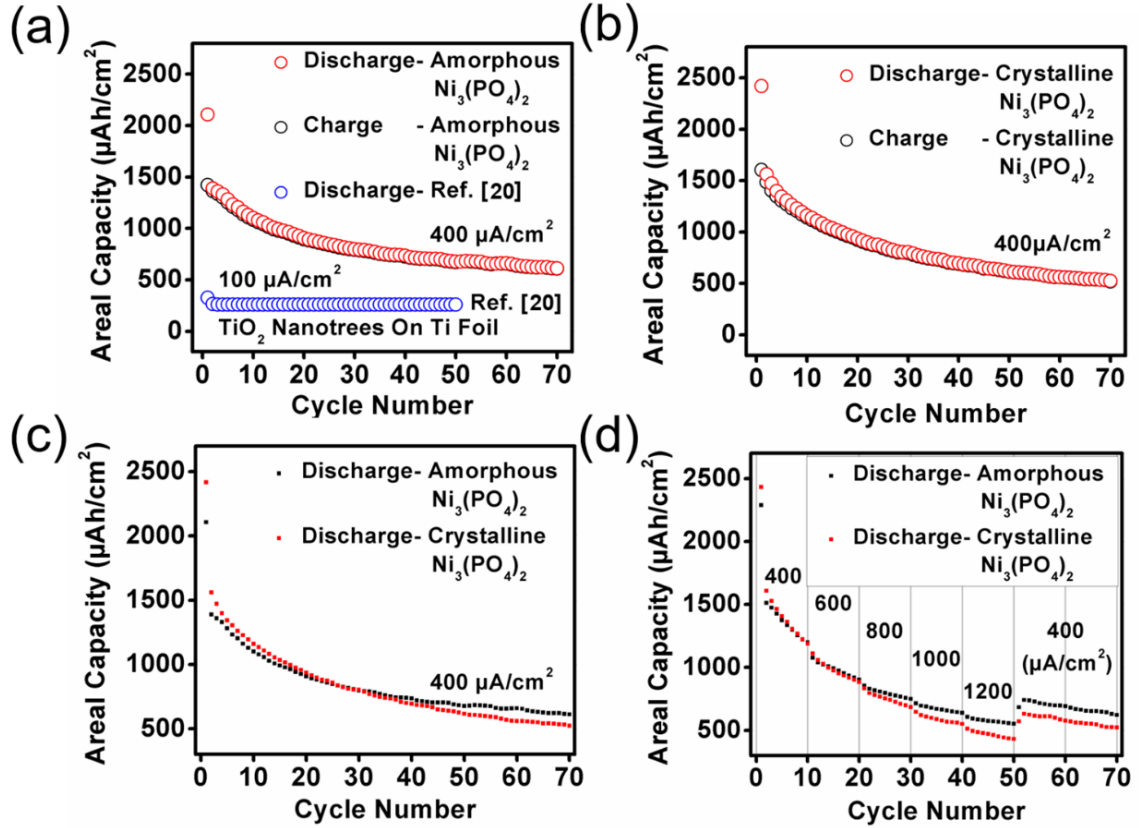


Figure 6-5. Electrochemical testing of the  $\text{Ni}_3(\text{PO}_4)_2$  anode in the LIB: (a) cycling performance (0-3V,  $400 \mu\text{A}/\text{cm}^2$ ) of amorphous  $\text{Ni}_3(\text{PO}_4)_2$  anode; (b) cycling performance (0-3V,  $400 \mu\text{A}/\text{cm}^2$ ) of crystalline  $\text{Ni}_3(\text{PO}_4)_2$  anode; (c) comparison of discharge capacity of amorphous and crystalline  $\text{Ni}_3(\text{PO}_4)_2$  anodes (0-3V,  $400 \mu\text{A}/\text{cm}^2$ ); (d) comparison of rate capability of amorphous and crystalline  $\text{Ni}_3(\text{PO}_4)_2$  anode (0-3V).

Electrochemical performance of  $\text{Ni}_3(\text{PO}_4)_2$  anodes was performed in Figure 6-5a-d. For the amorphous  $\text{Ni}_3(\text{PO}_4)_2$  anode (Figure 6-5a), the first irreversible capacity results from the formation of solid electrolyte interface (SEI).[19] In subsequent cycles, the discharge capacity started from  $1400 \mu\text{Ah}/\text{cm}^2$  and remained at  $600 \mu\text{Ah}/\text{cm}^2$  after 60 cycles. For the crystalline  $\text{Ni}_3(\text{PO}_4)_2$  anode (Figure 6-5b), the discharge capacity changed from  $1500 \mu\text{Ah}/\text{cm}^2$  to  $500 \mu\text{Ah}/\text{cm}^2$  in 70 cycles. Both of amorphous and crystalline capacity of

$\text{Ni}_3(\text{PO}_4)_2$  (current density:  $400 \mu\text{A}/\text{cm}^2$ ) are higher than the capacity (current density:  $100 \mu\text{A}/\text{cm}^2$ ) of other reported binder-free anode on Ti foil.[20] In Figure 6-5c, comparison of discharge capacity shows the capacity of crystalline  $\text{Ni}_3(\text{PO}_4)_2$  anode is higher than that of amorphous  $\text{Ni}_3(\text{PO}_4)_2$  anode at the early stage of cycles. Similar phenomena have been observed in some other reports.[21-23] In a crystalline structure, due to the ordered crystal lattice, locations for  $\text{Li}^+$  insertion are fixed. These fixed locations mean that the crystalline  $\text{Ni}_3(\text{PO}_4)_2$  is more active for  $\text{Li}^+$  insertion and is easier to obtain higher capacity in first several cycles compared with an amorphous structure.[24] Additionally, the tiny cracks on crystalline  $\text{Ni}_3(\text{PO}_4)_2$  (Figure 6-3d-f) was beneficial for  $\text{Ni}_3(\text{PO}_4)_2$  to react with electrolyte due to the increase of surface area,[25] which can also improve the capacity. However, along with the increase of cycles, the repeated insertion-extraction of  $\text{Li}^+$  started destroying the lattice structure of crystalline  $\text{Ni}_3(\text{PO}_4)_2$  due to the volume change in each cycle. Therefore, the capacity of crystalline  $\text{Ni}_3(\text{PO}_4)_2$  dropped fast and began to be lower than capacity of amorphous  $\text{Ni}_3(\text{PO}_4)_2$  in subsequent cycles. Contrarily, the capacity of amorphous  $\text{Ni}_3(\text{PO}_4)_2$  gradually intended to be stable after 50 cycles and almost remained  $600 \mu\text{Ah}/\text{cm}^2$  capacity in the last 10 cycles. This performance is to some degree higher than that of the crystalline  $\text{Ni}_3(\text{PO}_4)_2$ . Compared with the crystalline phase, the long-term disordered structure of amorphous phase provides more flexible interstitial spaces for shuttle of  $\text{Li}^+$  to sustain high stress/strain in charge and discharge process.[26] The rate capability (Figure 6-5d) further verifies this explanation. Along with the increase of current density, the gaps of capacity between amorphous and crystalline  $\text{Ni}_3(\text{PO}_4)_2$  became bigger. It is interesting to note that the capacity of amorphous anodes are usually obviously higher than crystalline anodes in

reports.[21,23] But in this work, the capacity of amorphous  $\text{Ni}_3(\text{PO}_4)_2$  is not too much higher than the crystalline  $\text{Ni}_3(\text{PO}_4)_2$  in the test condition, which should be attributed to the connected channel system in the film. The connected channel system contributes to lithium ion diffusion and alleviation of volume expansion in cycles. It indicates that the connected channel system plays a very important role for electrochemical performance. Therefore, it is possible for a crystalline anode to achieve electrochemical performance similar to its corresponding amorphous anode in LIBs by properly designing their microstructures during preparations.

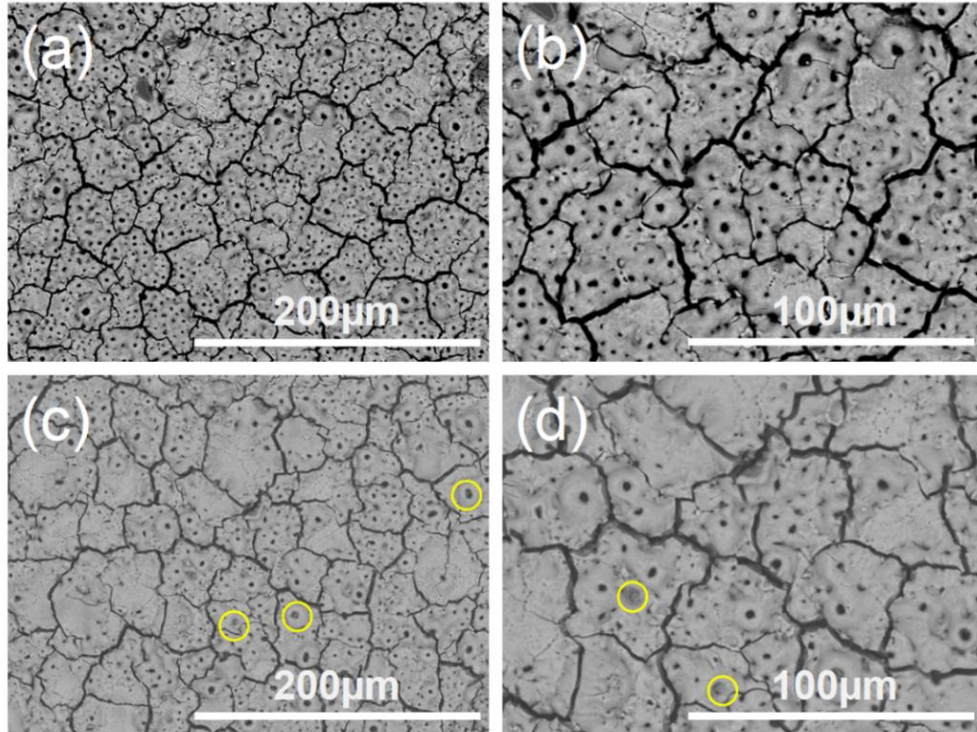


Figure 6-6. SEM images of  $\text{Ni}_3(\text{PO}_4)_2$  coatings after 70 cycles: surface morphologies of (a-b) amorphous  $\text{Ni}_3(\text{PO}_4)_2$  coating and (c-d) crystalline  $\text{Ni}_3(\text{PO}_4)_2$  coating.

Surface morphology of amorphous and crystalline  $\text{Ni}_3(\text{PO}_4)_2$  anodes after 70 cycles have been shown in Figure 6-6a-d. Cracks can be obviously seen on both of amorphous and

crystalline  $\text{Ni}_3(\text{PO}_4)_2$  anodes. The cracks might cause disconnections of the film horizontally but the films itself was still intact to the Ti substrate which contacted with the copper current collector in the LIB cell. As mentioned above, the cracks also make  $\text{Ni}_3(\text{PO}_4)_2$  have more reactive channels for ions due to the increase of surface areas.[25] Therefore, using cracks to explain the degradation of capacity may not be appropriate. The main reason of degradation of capacity is likely due to the decrease of pores' size. Compared with Figure 6-3a-f, the pores' size of both amorphous and crystalline  $\text{Ni}_3(\text{PO}_4)_2$  are obviously smaller after the test cycles. Those smaller pores partially blocked the lithium ion diffusion paths, leading to the decrease of capacity for both cases. It is necessary to point out that the reduction of pores' size cannot be explained by assuming the lattice expansion caused by permanent inserted lithium ions, because the coulombic efficiency in the cycling performance is nearly 100%. Compared with amorphous  $\text{Ni}_3(\text{PO}_4)_2$  anode after 70 cycles, the pores quantity of crystalline  $\text{Ni}_3(\text{PO}_4)_2$  anode after 70 cycles is obviously less. It is because during the charge and discharge processes in crystalline  $\text{Ni}_3(\text{PO}_4)_2$ , along with repeating insertion-extraction of lithium ions, the expansion and shrinkage of  $\text{Ni}_3(\text{PO}_4)_2$  lattice would lead to the structure collapse in lattice. The yellow-marked regions in Figure 6-6c-d show where the pores were sealed after 70 cycles. Contrarily, due to the long-term disordered structure of amorphous phase, amorphous  $\text{Ni}_3(\text{PO}_4)_2$  has more flexible interstitial spaces for shuttle of  $\text{Li}^+$  to sustain the high stress/strain of volume change. Therefore, in comparison with crystalline  $\text{Ni}_3(\text{PO}_4)_2$ , the quantity of pores in the amorphous  $\text{Ni}_3(\text{PO}_4)_2$  film after cycles is higher and the size of pores is larger. These surface morphology changes explain the reasons for capacity degradation and further support our above discussion about why the degradation rate on



capacity of crystalline  $\text{Ni}_3(\text{PO}_4)_2$  anode is higher than amorphous  $\text{Ni}_3(\text{PO}_4)_2$  anode.

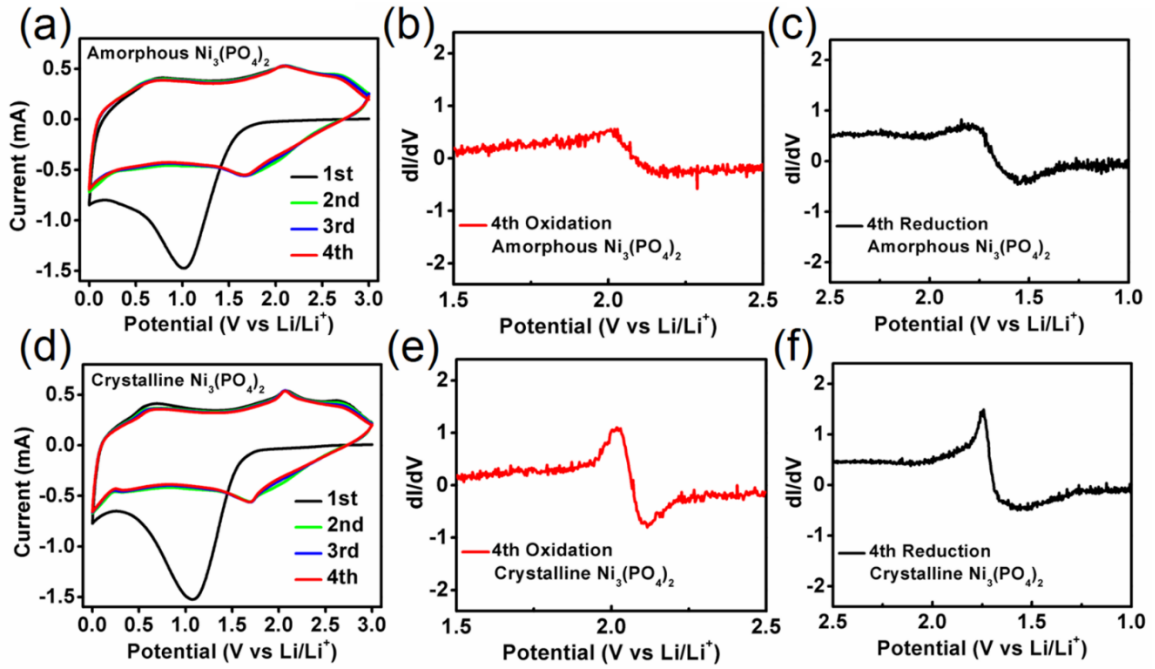
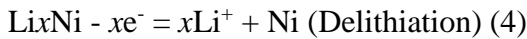
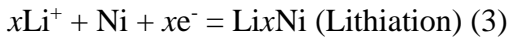
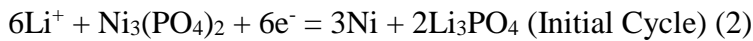


Figure 6-7. Cyclic Voltammetry (CV) (0.1mV/s) and derivative plot of 4th scanning: (a-c) amorphous  $\text{Ni}_3(\text{PO}_4)_2$ ; (d-f) crystalline  $\text{Ni}_3(\text{PO}_4)_2$ .

The cyclic Voltammetry and derivative plots of amorphous and crystalline  $\text{Ni}_3(\text{PO}_4)_2$  are shown in Figure 6-7a-f. In Figure 6-7a and Figure 6-7d, the peaks at 1.1V on reduction result from the formation of SEI.[19] Peaks at 1.7V and 2.05V are corresponding to the redox reactions of  $\text{Ni}_3(\text{PO}_4)_2$  anodes. According to the electrode reactions of  $\text{Pb}_3(\text{PO}_4)_2$  and  $\text{VPO}_4$  anodes in LIBs,[7,27] the electrode reactions of  $\text{Ni}_3(\text{PO}_4)_2$  should be written as follows:





In comparison between Figure 6-7b-c and Figure 6-7e-f, the  $dI/dV$  near redox potential of crystalline  $Ni_3(PO_4)_2$  are obviously higher than that of amorphous  $Ni_3(PO_4)_2$ . It indicates that for the crystalline anode, redox reactions were almost carried out on a fixed potential, which means the inserted locations of  $Li^+$  in crystalline  $Ni_3(PO_4)_2$  lattice were also fixed. This result supports our above discussion that the crystalline  $Ni_3(PO_4)_2$  is more active for  $Li^+$  insertion in the early stage of cycles compared with the amorphous  $Ni_3(PO_4)_2$ . However, for the amorphous  $Ni_3(PO_4)_2$ , a smaller slope of  $dI/dV$  near redox potential indicates that the redox reactions were carried out in a larger range of potential, which implies that the inserted locations of  $Li^+$  in amorphous phase are not fixed due to the long-term disordered structure. It also reflects that the amorphous phase has more flexible interstitial spaces for shuttle of  $Li^+$ . These CV analysis results further support our above discussion that the crystalline phase can be more active for  $Li^+$  insertion in the early stage of cycles and the amorphous phase can sustain higher stress/strain in cycles.

#### **6.4 Conclusions**

In this research, PAED was used to fast manufacture porous amorphous  $Ni_3(PO_4)_2$  anode of LIB. The crystalline  $Ni_3(PO_4)_2$  was obtained after an annealing treatment. From study of both amorphous and crystalline  $Ni_3(PO_4)_2$  anodes in LIBs, the change in pores morphology of the anodes suggested that the degradation of cycling performance resulted from the microstructure collapse in lattice. Compared with amorphous  $Ni_3(PO_4)_2$ , crystalline  $Ni_3(PO_4)_2$  performed with a higher capacity during the early stage of cycles is attributed to: i) the ordered crystalline structure is more active for  $Li^+$  insertion, and ii) the formation of cracks after the annealing made  $Ni_3(PO_4)_2$  offers more active channels for transportation of the electrolyte. However, the capacity of crystalline  $Ni_3(PO_4)_2$

dropped faster than amorphous  $\text{Ni}_3(\text{PO}_4)_2$  in cycles since the long-term disordered structure of amorphous  $\text{Ni}_3(\text{PO}_4)_2$  provides more flexible interstitial spaces for shuttle of  $\text{Li}^+$ , which enhances the ability to sustain stress/strain of volume change in cycles. Moreover, unlike other reports, the cycling performance of crystalline and amorphous  $\text{Ni}_3(\text{PO}_4)_2$  is generally similar. The similarity indicates that the connected channel system structure in the film plays a very important role to electrochemical performance. The connected channel system provides microscale spaces for volume expansion and diffusion paths for lithium ions. Therefore, it is possible for crystalline anodes to achieve the same electrochemical performance with amorphous anodes by properly designing their microstructures during anode preparations. The cycling performance shows that the areal capacity of amorphous  $\text{Ni}_3(\text{PO}_4)_2$  anode reached  $1400 \mu\text{Ah}/\text{cm}^2$  and remained at  $600 \mu\text{Ah}/\text{cm}^2$  after 60 cycles, which indicates that the  $\text{Ni}_3(\text{PO}_4)_2$  can be an appropriate anode material for LIB and PAED is a low-cost way to fast fabricate binder-free porous anode materials.

## REFERENCES

- [1] Armand, Michel, and J-M. Tarascon. "Building better batteries." *Nature* 451, no. 7179 (2008): 652.
- [2] Wu, Hui, Guihua Yu, Lijia Pan, Nian Liu, Matthew T. McDowell, Zhenan Bao, and Yi Cui. "Stable Li-ion battery anodes by in-situ polymerization of conducting hydrogel to conformally coat silicon nanoparticles." *Nature communications* 4 (2013): 1943.
- [3] Li, Yanguang, Bing Tan, and Yiyang Wu. "Mesoporous  $\text{Co}_3\text{O}_4$  nanowire arrays for lithium ion batteries with high capacity and rate capability." *Nano letters* 8, no. 1 (2008): 265-270.
- [4] Li, Baojun, Huaqiang Cao, Jin Shao, He Zheng, Yuexiang Lu, Jiefu Yin, and Meizhen Qu. "Improved performances of  $\beta\text{-Ni}(\text{OH})_2$ @reduced-graphene-oxide in Ni-MH and Li-ion batteries." *Chemical Communications* 47, no. 11 (2011): 3159-3161.
- [5] Huang, Gang, Feifei Zhang, Xinchuan Du, Yuling Qin, Dongming Yin, and Limin Wang. "Metal organic frameworks route to in situ insertion of multiwalled carbon nanotubes in  $\text{Co}_3\text{O}_4$  polyhedra as anode materials for lithium-ion batteries." *ACS nano* 9, no. 2 (2015): 1592-1599.
- [6] Liu, Si-Yu, Chao-Ying Fan, Han-Chi Wang, Jing-Ping Zhang, and Xing-Long Wu. "Electrochemical In Situ Formation of a Stable Ti-Based Skeleton for Improved Li-Storage Properties: A Case Study of Porous  $\text{CoTiO}_3$  Nanofibers." *Chemistry—A European Journal* 23, no. 36 (2017): 8712-8718.
- [7] Liu, Zhaolin, and Jim Yang Lee. "Electrochemical performance of  $\text{Pb}_3(\text{PO}_4)_2$  anodes in rechargeable lithium batteries." *Journal of power sources* 97 (2001): 247-250.
- [8] Li, Xin, Abdelnaby M. Elshahawy, Cao Guan, and John Wang. "Metal Phosphides and Phosphates-based Electrodes for Electrochemical Supercapacitors." *Small* 13, no. 39 (2017): 1701530.

- [9] Nam, Ki Min, Eun Ah Cheon, Won Jung Shin, and Allen J. Bard. "Improved photoelectrochemical water oxidation by the  $\text{WO}_3/\text{CuWO}_4$  composite with a manganese phosphate electrocatalyst." *Langmuir* 31, no. 39 (2015): 10897-10903.
- [10] Kim, Eunjin, Dongyeon Son, Tae-Gon Kim, Jaephil Cho, Byungwoo Park, Kwang-Sun Ryu, and Soon-Ho Chang. "A Mesoporous/Crystalline Composite Material Containing Tin Phosphate for Use as the Anode in Lithium-Ion Batteries." *Angewandte Chemie International Edition* 43, no. 44 (2004): 5987-5990.
- [11] Bao, Lin, Tao Li, Shu Chen, Chang Peng, Ling Li, Qian Xu, Yashao Chen, Encai Ou, and Weijian Xu. "3D Graphene Frameworks/ $\text{Co}_3\text{O}_4$  Composites Electrode for High-Performance Supercapacitor and Enzymeless Glucose Detection." *Small* 13, no. 5 (2017): 1602077.
- [12] Min, Liang, Tao Li, Qi Tan, Xiaoping Tan, Wu Pan, Li He, Jie Zhang, Encai Ou, and Weijian Xu. "Transcription of G-quartet supramolecular aggregates into hierarchical mesoporous silica nanotubes." *Dalton Transactions* 45, no. 18 (2016): 7912-7920.
- [13] Li, Tao, and Xueyuan Nie. "One-Step Fast-Synthesized Foamlike Amorphous  $\text{Co}(\text{OH})_2$  Flexible Film on Ti Foil by Plasma-Assisted Electrolytic Deposition as a Binder-Free Anode of a High-Capacity Lithium-Ion Battery." *ACS applied materials & interfaces* 10, no. 20 (2018): 16943-16946.
- [14] Mai, Fu-Der, Wen-Lian William Lee, Jia-Lin Chang, Shou-Ching Liu, Chia-Wei Wu, and Chiing-Chang Chen. "Fabrication of porous  $\text{TiO}_2$  film on Ti foil by hydrothermal process and its photocatalytic efficiency and mechanisms with ethyl violet dye." *Journal of hazardous materials* 177, no. 1-3 (2010): 864-875.
- [15] Padmanathan, N., Han Shao, and Kafil M. Razeeb. "Multifunctional nickel phosphate nano/microflakes 3D electrode for electrochemical energy storage, nonenzymatic glucose, and sweat pH sensors." *ACS applied materials & interfaces* 10, no. 10 (2018): 8599-8610.
- [16] Inoue, Akihisa. "Stabilization of metallic supercooled liquid and bulk amorphous alloys." *Acta materialia* 48, no. 1 (2000): 279-306.

- [17] Sharma, Pratigya, Sivaprakasam Radhakrishnan, Myung-Seob Khil, Hak-Yong Kim, and Byoung-Suhk Kim. "Simple room temperature synthesis of porous nickel phosphate foams for electrocatalytic ethanol oxidation." *Journal of Electroanalytical Chemistry* 808 (2018): 236-244.
- [18] Ko, Y. G., K. M. Lee, B. U. Lee, and D. H. Shin. "An electrochemical analysis of AZ91 Mg alloy processed by plasma electrolytic oxidation followed by static annealing." *Journal of Alloys and Compounds* 509 (2011): S468-S472.
- [19] Ni, Shibing, Xiaohu Lv, Tao Li, Xuelin Yang, and Lulu Zhang. "The investigation of Ni(OH)<sub>2</sub>/Ni as anodes for high performance Li-ion batteries." *Journal of Materials Chemistry A* 1, no. 5 (2013): 1544-1547.
- [20] Wen, Wei, Jin-Ming Wu, Yin-Zhu Jiang, Jun-Qiang Bai, and Lu-Lu Lai. "Titanium dioxide nanotrees for high-capacity lithium-ion microbatteries." *Journal of Materials Chemistry A* 4, no. 27 (2016): 10593-10600.
- [21] Zhang, Deyin, Mingli Qin, Min Huang, Haoyang Wu, Baorui Jia, Zhiwei Liu, Tingting Liu, Xuanhui Qu, and Peng Cao. "Facile synthesis of amorphous Cr<sub>2</sub>O<sub>3</sub>/N-doped carbon nanosheets and its excellent lithium storage property." *Journal of the American Ceramic Society* 101, no. 7 (2018): 3234-3243.
- [22] Hwang, Soo Min, Junsoo Kim, Yongil Kim, and Youngsik Kim. "Na-ion storage performance of amorphous Sb<sub>2</sub>S<sub>3</sub> nanoparticles: anode for Na-ion batteries and seawater flow batteries." *Journal of Materials Chemistry A* 4, no. 46 (2016): 17946-17951.
- [23] Kaspar, Jan, Magdalena Graczyk-Zajac, Stefan Lauterbach, Hans-Joachim Kleebe, and Ralf Riedel. "Silicon oxycarbide/nano-silicon composite anodes for Li-ion batteries: Considerable influence of nano-crystalline vs. nano-amorphous silicon embedment on the electrochemical properties." *Journal of Power Sources* 269 (2014): 164-172.
- [24] Pervez, Syed Atif, Doohun Kim, Umer Farooq, Adnan Yaqub, Jung-Hee Choi, You-Jin Lee, and Chil-Hoon Doh. "Comparative electrochemical analysis of crystalline and amorphous anodized iron oxide nanotube layers as negative electrode for LIB." *ACS applied materials & interfaces* 6, no. 14 (2014): 11219-11224.

- [25] He, Yu, Xiqian Yu, Yanhong Wang, Hong Li, and Xuejie Huang. "Alumina-coated patterned amorphous silicon as the anode for a lithium-ion battery with high Coulombic efficiency." *Advanced Materials* 23, no. 42 (2011): 4938-4941.
- [26] Guo, Juchen, Qing Liu, Chunsheng Wang, and Michael R. Zachariah. "Interdispersed amorphous MnO<sub>x</sub>-carbon nanocomposites with superior electrochemical performance as lithium-storage material." *Advanced Functional Materials* 22, no. 4 (2012): 803-811.
- [27] Zheng, Jun-chao, Ya-dong Han, Bao Zhang, Chao Shen, Lei Ming, Xing Ou, and Jia-feng Zhang. "Electrochemical properties of VPO<sub>4</sub>/C nanosheets and microspheres as anode materials for lithium-ion batteries." *ACS applied materials & interfaces* 6, no. 9 (2014): 6223-6226.

## SUPPORTING INFORMATION

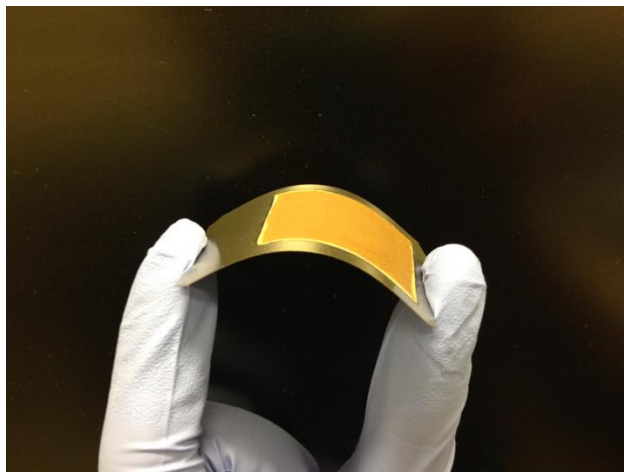


Figure S6-1. Photo of as prepared  $\text{Ni}_3(\text{PO}_4)_2$  anode.

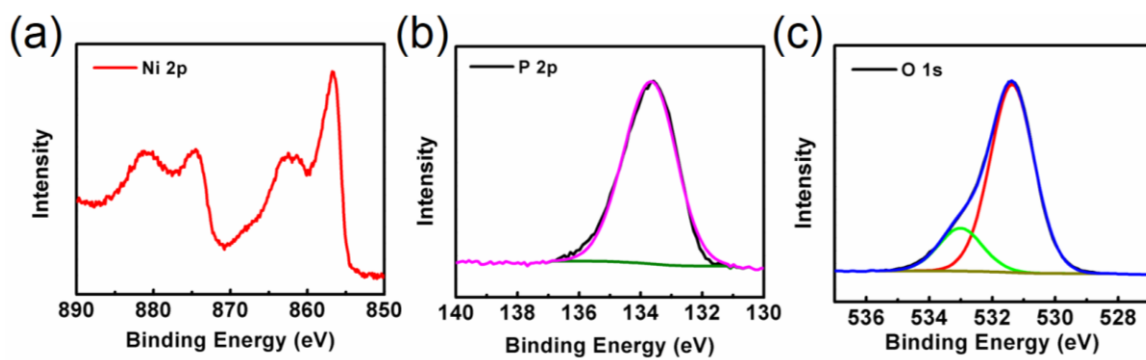


Figure S6-2. XPS spectra of amorphous  $\text{Ni}_3(\text{PO}_4)_2$  (b) Ni2p, (c) P2p and (d) O1s.

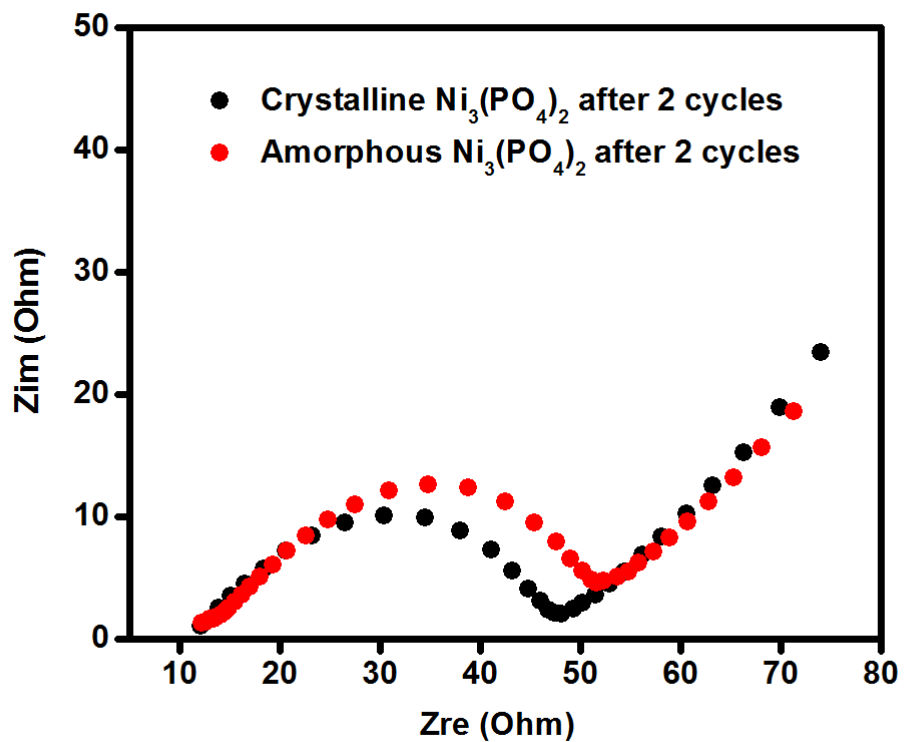


Figure S6-3. EIS of amorphous and crystalline  $\text{Ni}_3(\text{PO}_4)_2$  anodes in lithium-ion batteries.

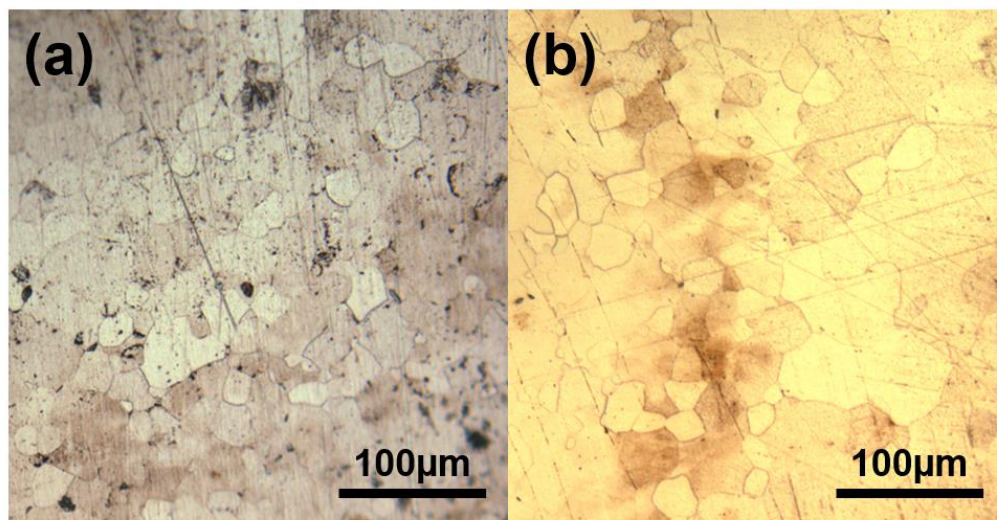


Figure S6-4. Metallography of Ti foil before (a) and after (b) annealing.



## CHAPTER 7

### Possible Methods to Improve the Electrochemical Performance of Amorphous $\text{Ni}_3(\text{PO}_4)_2$ Anode in Lithium-Ion Battery

#### **7.1 Introduction**

The amorphous  $\text{Ni}_3(\text{PO}_4)_2$  anode exhibited the high capacity in Lithium-ion battery.[1] However, the degradation of the capacity is a problem that impedes the amorphous  $\text{Ni}_3(\text{PO}_4)_2$  anode moving toward to practical application. Therefore, in this study, we provided some possible methods to improve the cycling stability and capacity of  $\text{Ni}_3(\text{PO}_4)_2$  anodes in lithium-ion batteries. Firstly, the Co-doped  $\text{Ni}_3(\text{PO}_4)_2$  anode was researched but the electrochemical performance is bad since the reduced porosity of coating in comparison with pure  $\text{Ni}_3(\text{PO}_4)_2$  coating. Then, the sputtering Au modified  $\text{Ni}_3(\text{PO}_4)_2$  anode was investigated. The cycling stability of Au coated  $\text{Ni}_3(\text{PO}_4)_2$  anode was obviously increased, which could be attributed to the remarkable conductivity of Au. Lastly, the  $\text{Ni}_3(\text{PO}_4)_2$  anodes were modified by sputtering carbon and dip coating carbon nanofibers, respectively. The electrochemical testing shows that the both capacity and cycling stability of  $\text{Ni}_3(\text{PO}_4)_2$  anode were improved by modification of sputtering carbon, which results from the contribution of carbon to conductivity and capacity. However, after dip carbon nanofibers coating, the  $\text{Ni}_3(\text{PO}_4)_2$  anode has a little improvement on capacity but no obvious improvement on cycling stability because the existence of binder blocks the efficient transfer of ions and electrons during cycling.

#### **7.2 Experimental Section**

##### **7.2.1 Co-doped $\text{Ni}_3(\text{PO}_4)_2$**

A Ti foil (Sigma Aldrich, thickness: 0.127mm) was immersed in an electrolyte (5g/L  $(\text{CH}_3\text{COO})_2\text{Co}$ , 20g/L  $(\text{CH}_3\text{COO})_2\text{Ni}$  and 17g/L  $\text{H}_3\text{PO}_4$  in deionized water, Sigma

Aldrich) held in a stainless-steel vessel. One side of the Ti foil was fully covered. Then the Ti foil and stainless-steel vessel were connected with positive and negative terminals of a power supply, respectively. Lastly, 3A current was applied for 2 mins to obtain an amorphous  $\text{Ni}_3(\text{PO}_4)_2$  film on Ti. Sample was dried under 60 °C.

#### ***7.2.2 Sputtering Au coated $\text{Ni}_3(\text{PO}_4)_2$***

Amorphous  $\text{Ni}_3(\text{PO}_4)_2$  sample was placed in the Au coater with 10 times running. The Au coater worked under the fix parameters for SEM samples.

#### ***7.2.3 Dip carbon nanofibers coated $\text{Ni}_3(\text{PO}_4)_2$***

The carbon nanofibers, PVDF (wt% 2: 1) was mixed in NMP and stir 24 hours to make slurry. Then  $\text{Ni}_3(\text{PO}_4)_2$  sample was dipped into slurry and taken out after 30s. This operation was repeated for 5 times. Subsequently, The Ti side was cleaned and the sample was vacuum dried for 12h at 80 C

#### ***7.2.4 Sputtering carbon coated $\text{Ni}_3(\text{PO}_4)_2$***

Amorphous  $\text{Ni}_3(\text{PO}_4)_2$  sample was placed in the carbon coater with 10 times running. The carbon coater worked under the fix parameters for SEM samples.

#### ***7.2.5 Materials characterization***

The microstructure observation was performed by scanning electron microscopy (SEM, Hitachi, TM 3030).

#### ***7.2.6 Electrochemical measurement***

The samples served as the working electrode with lithium chip (Sigma Aldrich) as the counter electrode. Then, they were sealed into a CR2032 coin cell case (MTI Crop.) with  $\text{LiPF}_6$  electrolyte (Sigma Aldrich, EC:DMC 1:1), separator (MTI Crop.). All the

operations were completed in an Argon gas glove box (LABmaster 130). Cycling performance was tested by a LAND battery testing system.

### 7.3 Results and Discussion

#### 7.3.1 Co-doped $\text{Ni}_3(\text{PO}_4)_2$

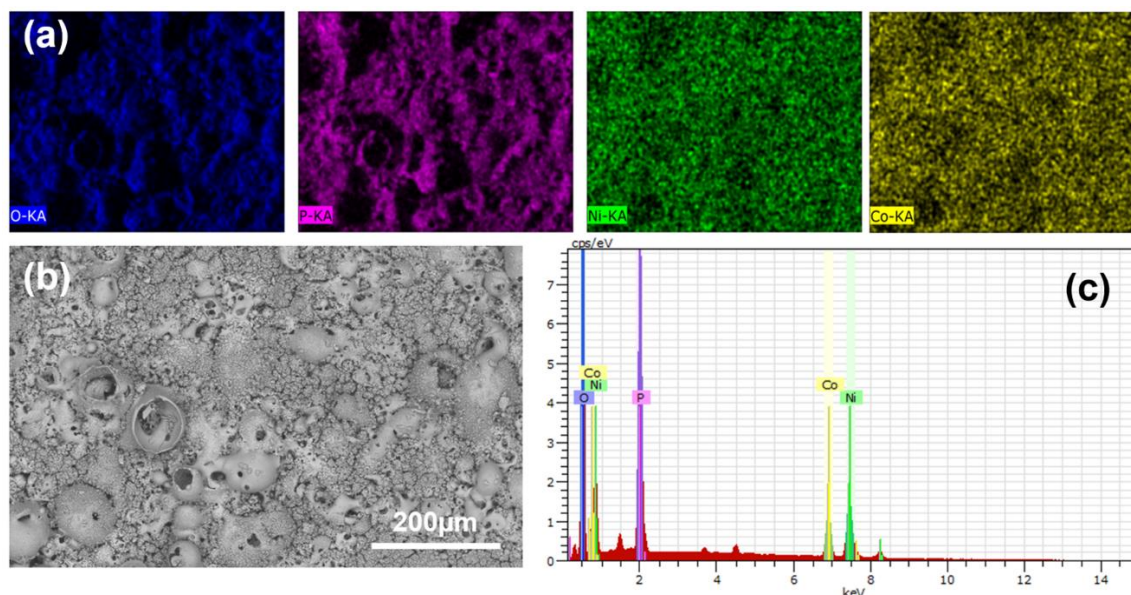


Figure 7-1. SEM characterization of Co-doped  $\text{Ni}_3(\text{PO}_4)_2$ : (a) elements mapping; (b) surface morphology; (c) EDS.

The SEM results are shown in Figure 7-1. In Figure 7-1a, the elements mapping illustrates that the contents of coating are O, P, Ni and Co. The atomic parentage of these four elements are determined by EDS analysis (Figure 7-1c). The results indicate that presence of Co in the  $\text{Ni}_3(\text{PO}_4)_2$  coating. According to the surface morphology (Figure 7-1b), the porosity of Co-doped  $\text{Ni}_3(\text{PO}_4)_2$  coating is lower than that of pure  $\text{Ni}_3(\text{PO}_4)_2$  coating, which could be attributed to the fact that adding co-containing solute changed the discharging effects of Ti foil in electrolyte. The inferior discharging leads to the formation of bulk structure coating without abundant pores. The reasons of inferior

discharging effects are unspecified. Reducing the concentration of Co-containing solute might improves the discharging capacity, which can be as the future works for group.

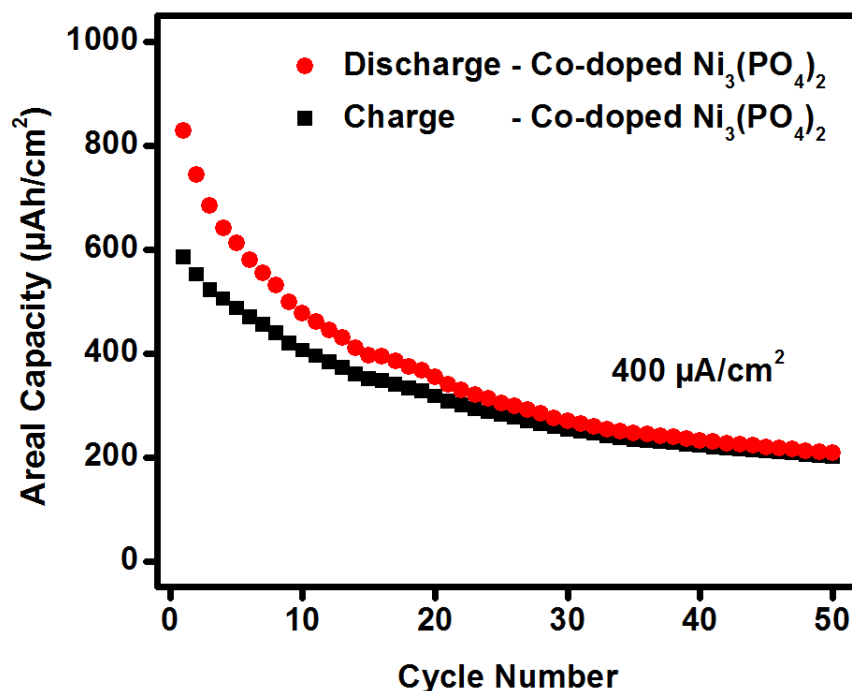


Figure 7-2. Cycling performance of Co-doped  $\text{Ni}_3(\text{PO}_4)_2$  anode.

The cycling performance of Co-doped  $\text{Ni}_3(\text{PO}_4)_2$  is shown in Figure 7-2. The capacity can reach  $810 \mu\text{Ah}/\text{cm}^2$  and only  $200 \mu\text{Ah}/\text{cm}^2$  was kept after 40 cycles. Both capacity and cycling stability are lower than that of pure  $\text{Ni}_3(\text{PO}_4)_2$  anode in LIB. It results from the reduction of porosity. The inferior discharging lead to the low porosity which means the less diffusion paths for lithium ions during the charge/discharge process. The gap between the charge and discharge capacity could be explained by the low surface area. The low surface area leads to the unstable SEI on electrode, which makes the columbic efficiency is low in cycles.[2]

### 7.3.2 Sputtering Au coated $\text{Ni}_3(\text{PO}_4)_2$

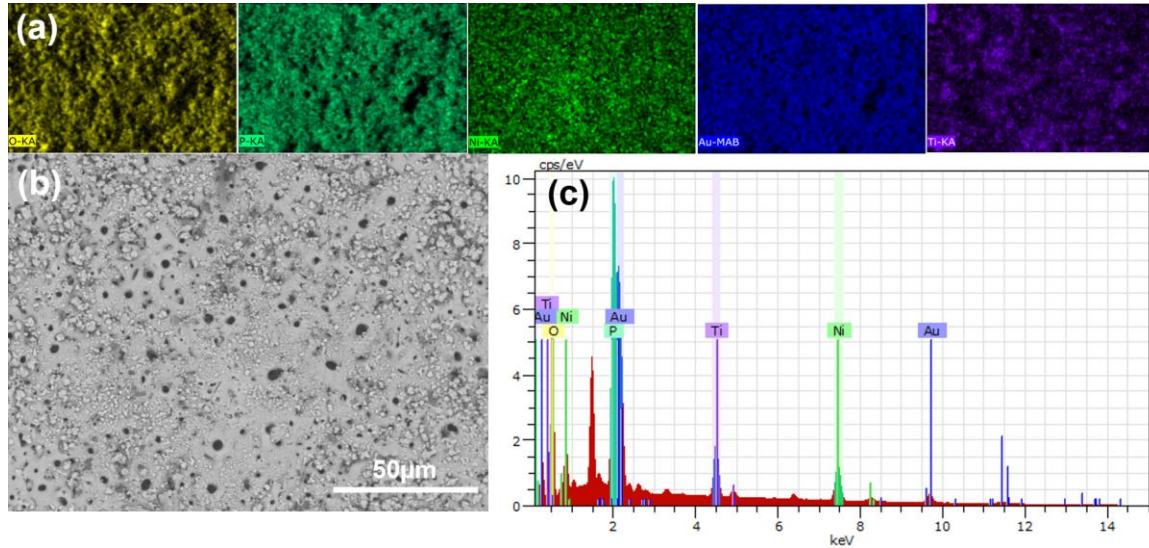


Figure 7-3. SEM characterization of  $\text{Au/Ni}_3(\text{PO}_4)_2$ : (a) elements mapping; (b) surface morphology; (c) EDS.

In Figure 7-3, the elements mapping (Figure 7-3a) and EDS (Figure 7-3c) reveal the presence of Au, Ti, Ni, O and P elements. The Ti, O, P and Ni should be attributed to the Ti substrate and  $\text{Ni}_3(\text{PO}_4)_2$  film. The Au can be assigned to the sputtering Au coating. Above results reveal the existence of Ag on  $\text{Ni}_3(\text{PO}_4)_2$  film. In Figure 7-3b, it can be observed that some cluster of Au on the surface of  $\text{Ni}_3(\text{PO}_4)_2$  film, which further identify the existence of Au.

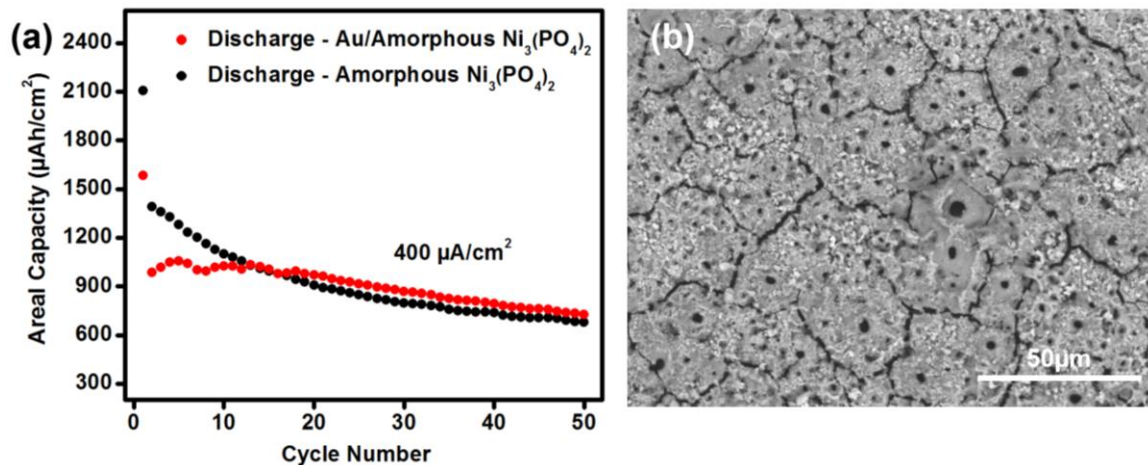


Figure 7-4. (a) Cycling performance of Au/ $\text{Ni}_3(\text{PO}_4)_2$  and  $\text{Ni}_3(\text{PO}_4)_2$ ; (b) Surface morphology of Au/ $\text{Ni}_3(\text{PO}_4)_2$  after 50 cycles.

The cycling performance of Au/ $\text{Ni}_3(\text{PO}_4)_2$  in LIB was shown in Figure 7-4a. The capacity of Au/ $\text{Ni}_3(\text{PO}_4)_2$  can reach  $1000 \mu\text{Ah}/\text{cm}^2$  and keep  $800 \mu\text{Ah}/\text{cm}^2$  after 50 cycles. Compared with  $\text{Ni}_3(\text{PO}_4)_2$ , the cycling stability of Au/ $\text{Ni}_3(\text{PO}_4)_2$  was obviously improved, which can be attributed to the high conductivity of Au.[3] The high conductivity of Au enhances the ions and electrons transfer efficiency during the cycling. However, the capacity of Au/ $\text{Ni}_3(\text{PO}_4)_2$  does not have an obvious increase. It because the Au can only contribute conductivity but not capacity. For the capacity gap between the Au/ $\text{Ni}_3(\text{PO}_4)_2$  and  $\text{Ni}_3(\text{PO}_4)_2$  in first 15 cycles, it has been observed in many reports, but the principle is still unspecified.[2-4] The surface morphology of the anode after cycling has been showed in Figure 7-4b. Compared with 7-3b, the shrink of pores can be observed, which explains the little degradation on capacity during the cycling. The effects of Au coating thickness on electrochemical performance of  $\text{Ni}_3(\text{PO}_4)_2$  anode can be as the future works for group.



### 7.3.3 Dip carbon nanofibers coated $\text{Ni}_3(\text{PO}_4)_2$

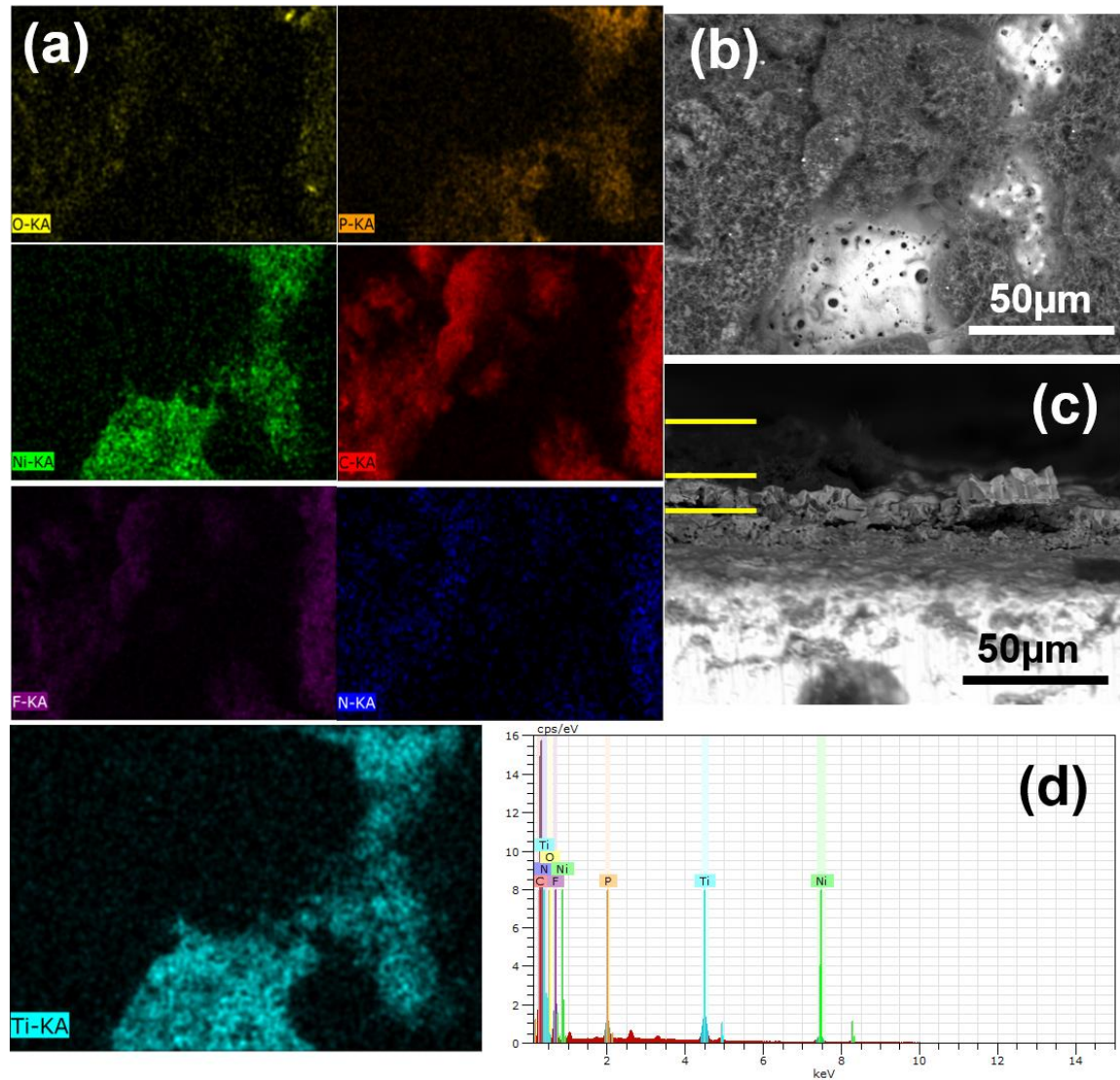


Figure 7-5. SEM characterization of carbon nanofiber/ $\text{Ni}_3(\text{PO}_4)_2$ : (a) elements mapping; (b) surface morphology; (c) cross-section; (d) EDS.

In Figure 7-5a and d, the elements mapping and EDS indicate the existence of carbon. The N and F elements come from the binder. In Figure 7-5b, it can be observed the structure of binder on  $\text{Ni}_3(\text{PO}_4)_2$  film. In the cross-sectional image, the thickness of the dip coating materials is around 30μm.

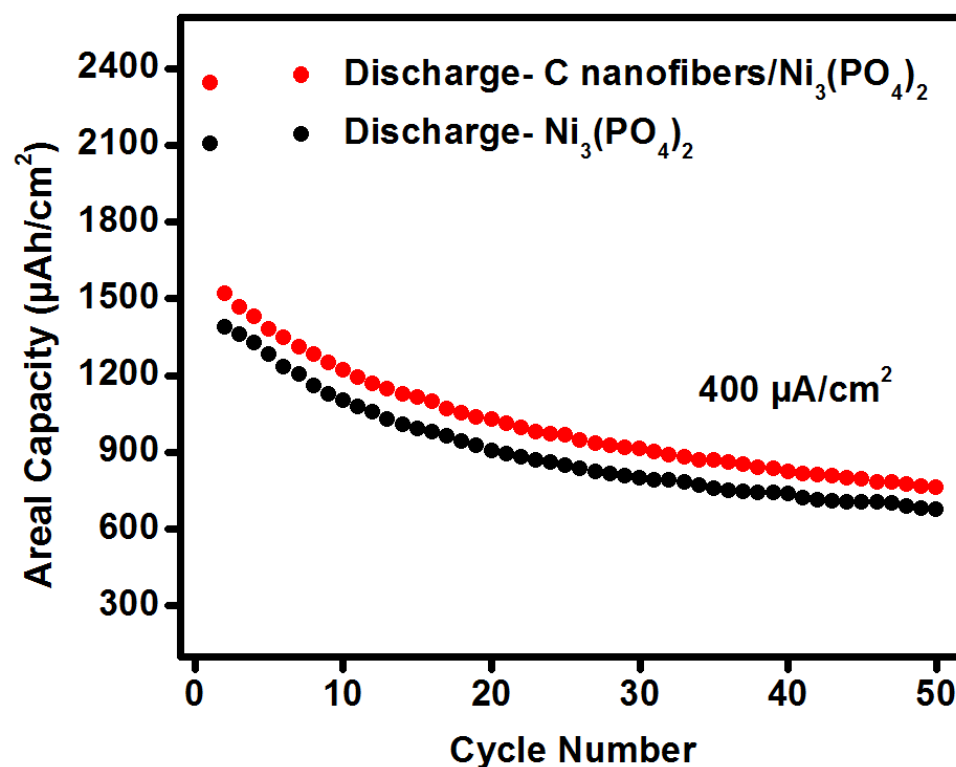


Figure 7-6. Cycling performance of carbon nanofibers/Ni<sub>3</sub>(PO<sub>4</sub>)<sub>2</sub> and Ni<sub>3</sub>(PO<sub>4</sub>)<sub>2</sub>.

The cycling performance of Carbon nanofibers/Ni<sub>3</sub>(PO<sub>4</sub>)<sub>2</sub> has been shown in Figure 7-6. After the modification of carbon nanofibers, the capacity of Ni<sub>3</sub>(PO<sub>4</sub>)<sub>2</sub> was improved due to the capacity contribution from the carbon nanofiber. The cycling stability of Ni<sub>3</sub>(PO<sub>4</sub>)<sub>2</sub> cannot be improved. However, carbon nanofibers have good conductivity, but didn't stabilize the capacity, which could be attributed to the presence of binder. The existence of binder injures the conductivity of carbon nanofiber since the formation of unconnected active materials units.[1]



### 7.3.4 Sputtering carbon coated $\text{Ni}_3(\text{PO}_4)_2$

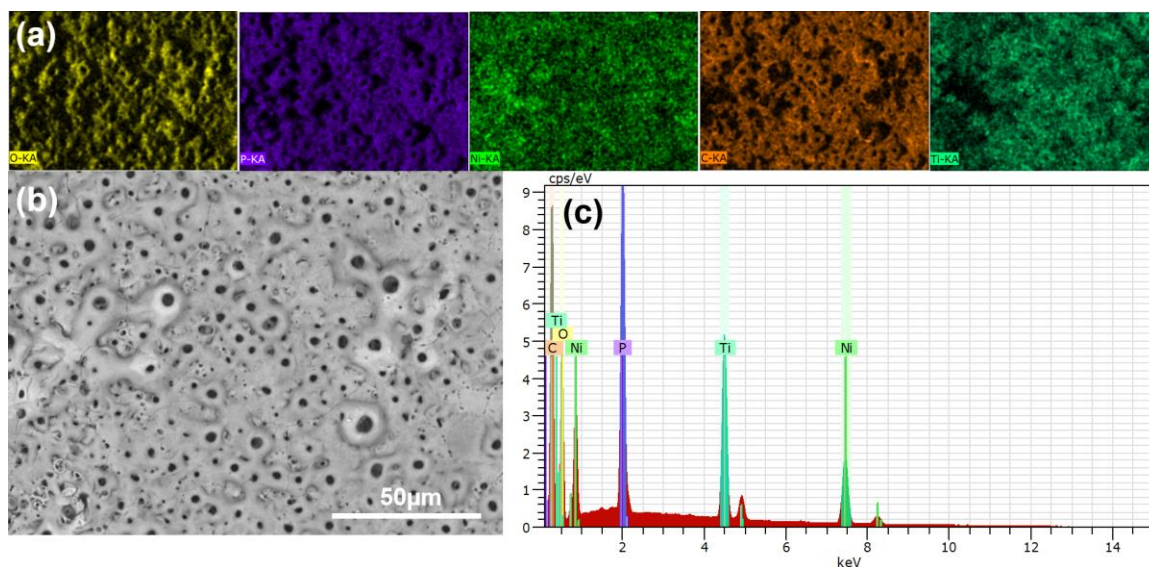


Figure 7-7. SEM characterization of  $\text{C}/\text{Ni}_3(\text{PO}_4)_2$ : (a) elements mapping; (b) surface morphology; (c) EDS.

In Figure 7-7a and c, the elements mapping and the EDS results shows the presence of C, P, O, Ni and Ti elements. The Ni, O and P elements come from the  $\text{Ni}_3(\text{PO}_4)_2$ . The Ti elements comes from the substrate. The C elements can be assigned to the sputtering carbon coating. These results indicate that the carbon coating has been on the  $\text{Ni}_3(\text{PO}_4)_2$  film after the sputtering. In Figure 7-7b, pores structure still can be observed after the carbon coating.

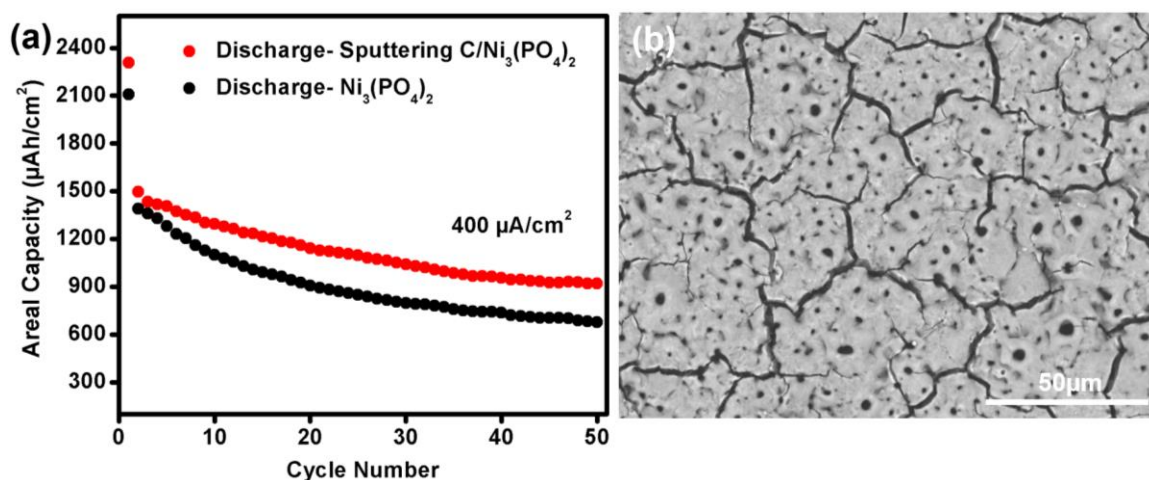


Figure 7-8. (a) Cycling performance of C/ $\text{Ni}_3(\text{PO}_4)_2$  and  $\text{Ni}_3(\text{PO}_4)_2$ ; (b) Surface morphology of C/ $\text{Ni}_3(\text{PO}_4)_2$  after 50 cycles.

The cycling performance of sputtering carbon/ $\text{Ni}_3(\text{PO}_4)_2$  anode was shown in Figure 7-8a. The capacity of carbon/ $\text{Ni}_3(\text{PO}_4)_2$  can reach  $1400 \mu\text{Ah}/\text{cm}^2$  and keep  $1000 \mu\text{Ah}/\text{cm}^2$  at 40th cycles. After the carbon coated, both capacity and cycling stability of  $\text{Ni}_3(\text{PO}_4)_2$  were increased, which results from the capacity contribution and the high conductivity from the carbon. The high conductive stabilized capacity by the highly efficient electron and ion transfer. The lithium storage capability of carbon adds capacity for  $\text{Ni}_3(\text{PO}_4)_2$ . Therefore, the sputtering carbon coated  $\text{Ni}_3(\text{PO}_4)_2$  could be the best choice for improving the electrochemical performance of  $\text{Ni}_3(\text{PO}_4)_2$  in comparison with above 2 methods. The surface morphology of the anode after cycling has been showed in Figure 7-8b. Compared with 7-7b, the shrink of pores can be observed, which explains the little degradation on capacity during the cycling. The effects of coating thickness on electrochemical performance of  $\text{Ni}_3(\text{PO}_4)_2$  anode can be as the future works for group.

#### ***7.4 Conclusions***

In this work, the possible methods for improving the electrochemical performance of  $\text{Ni}_3(\text{PO}_4)_2$  were illustrated. The Co-doping cannot improve the electrochemical performance due to the low porosity. The sputtering Au coating can only improve the cycling stability of  $\text{Ni}_3(\text{PO}_4)_2$  because the contribution of conductivity from Au. The dip carbon nanofibers coating can only improve the capacity of  $\text{Ni}_3(\text{PO}_4)_2$  because the contribution of capacity from carbon. The sputtering carbon coating not only improve the capacity but also the cycling stability, which should be attributed to the both contribution of capacity and conductivity from carbon. The effects of different coating materials and thickness on electrochemical performance of modified  $\text{Ni}_3(\text{PO}_4)_2$  anodes can be as the future works for group.

## REFERENCES

- [1] Li, Tao, Ran Cai, Xueyuan Nie, and Jimi Tjong. "Porous  $\text{Ni}_3(\text{PO}_4)_2$  thin film as a binder-free and low-cost anode of a high-capacity lithium-ion battery." *Journal of Electroanalytical Chemistry* (2019): 81-85
- [2] Yazami, Rachid. *Nanomaterials for Lithium-ion batteries: Fundamentals and Applications*. Pan Stanford, 2013.
- [3] Wang, Pan, Ling Tong, Rongfei Wang, Anran Chen, Wenzhong Fang, Kun Yue, Tao Sun, and Yu Yang. "Improved performances of lithium-ion batteries using intercalated a-Si–Ag thin film layers as electrodes." *RSC Advances* 8, no. 72 (2018): 41404-41414.
- [4] Zhang, Wei-Jun. "A review of the electrochemical performance of alloy anodes for lithium-ion batteries." *Journal of Power Sources* 196, no. 1 (2011): 13-24.

## CHAPTER 8

### Conclusions and Future Work

In this study, the plasma-assisted electrolytic deposition (PAED) was used to rapidly fabricate the amorphous  $\text{Co}(\text{OH})_2$  and  $\text{Ni}_3(\text{PO}_4)_2$  binder-free thin film anodes of lithium-ion batteries (LIBs). The short manufacture time allows us to obtain the low-cost anodes. The nature of binder-free and amorphous phase makes anodes acquire the high capacity and great rate capability in electrochemical tests. The capacity of amorphous  $\text{Co}(\text{OH})_2$  anodes can reach  $2000 \mu\text{Ah}/\text{cm}^2$  and remain at  $930 \mu\text{Ah}/\text{cm}^2$  after 45 cycles (current density:  $400 \mu\text{A}/\text{cm}^2$ ) in lithium-ion batteries. When the charge/discharge current density was increased to  $1200 \mu\text{A}/\text{cm}^2$ , the  $\text{Co}(\text{OH})_2$  still keeps capacity of  $250 \mu\text{Ah}/\text{cm}^2$ . The amorphous  $\text{Ni}_3(\text{PO}_4)_2$  anodes can reach  $1400 \mu\text{Ah}/\text{cm}^2$  and remain at  $750 \mu\text{Ah}/\text{cm}^2$  after 40 cycles (current density:  $400 \mu\text{A}/\text{cm}^2$ ). Even current density of  $1200 \mu\text{A}/\text{cm}^2$  was applied during cycling, the capacity of  $\text{Ni}_3(\text{PO}_4)_2$  still has  $600 \mu\text{Ah}/\text{cm}^2$ . The high capacity of both materials can be attributed to the pores structured films, which provide the abundant diffusion paths for lithium ions during cycling. The great rate capability of both materials results from the long-term disordered amorphous phase which has enough spaces to sustain the stress/strain in charge/discharge process. Compared with amorphous  $\text{Co}(\text{OH})_2$  coating, the amorphous  $\text{Ni}_3(\text{PO}_4)_2$  coating has the better stability and the lower thickness, which is more hopeful for industrial application. Therefore,  $\text{Ni}_3(\text{PO}_4)_2$  anode was further studied.

In comparative electrochemical study between the amorphous and crystalline  $\text{Ni}_3(\text{PO}_4)_2$ , the amorphous  $\text{Ni}_3(\text{PO}_4)_2$  showed a lower degradation rate on capacity, while the crystalline one had a higher capacity in the initial several cycles. However, both

amorphous and crystalline  $\text{Ni}_3(\text{PO}_4)_2$  shows the similar high capacity during cycling because of the high porosity of films, which reveals that the pores structure plays the most important role on acquisition of high capacity.

Lastly, the possible methods for improving the electrochemical performance of amorphous  $\text{Ni}_3(\text{PO}_4)_2$  were explored including Co-doping, sputtering Au coating, dip carbon nanofibers coating and sputtering carbon coating. According to cycling performance of modified  $\text{Ni}_3(\text{PO}_4)_2$  anodes, the sputtering Au coating can only improve the cycling stability of  $\text{Ni}_3(\text{PO}_4)_2$  because of the contribution of conductivity from Au. At the 50th cycle, the capacity of  $\text{Au/Ni}_3(\text{PO}_4)_2$  was only degraded by  $150 \mu\text{Ah}/\text{cm}^2$ , which is obviously less than the degradation on capacity of  $\text{Ni}_3(\text{PO}_4)_2$ . The dip carbon nanofibers coating can only improve the capacity of  $\text{Ni}_3(\text{PO}_4)_2$  because the contribution of capacity from carbon nanofibers. The sputtering carbon coating improved not only the capacity but also the cycling stability of  $\text{Ni}_3(\text{PO}_4)_2$ , which should be attributed to the both contribution of capacity and conductivity from carbon. The capacity of  $\text{carbon/Ni}_3(\text{PO}_4)_2$  can reach  $1400 \mu\text{Ah}/\text{cm}^2$  and keep  $1000 \mu\text{Ah}/\text{cm}^2$  after 40th cycles. Therefore, based on the consideration of electrochemical performance and fabrication cost, the sputtering carbon coating could be the best way to improve the properties of  $\text{Ni}_3(\text{PO}_4)_2$  anodes in lithium-ion batteries.

In summary, this study illustrated that the plasma-assisted electrolytic deposition (PAED) is a low-cost way to rapid manufacture the binder-free anode materials of high-capacity lithium-ion batteries. Additionally, after the reasonable surface modification, the electrochemical performance of PAED synthesized anode materials in lithium-ion batteries are hopeful to be improved.

In the future work, to further reduce the cost on manufacture, the PAED synthesized iron phosphate anodes could be obtained in the iron acetate electrolyte since the resource of Fe is more abundant than that of Co and Ni in the earth. The Ti foil substrate of anodes might be replaced by some cheaper materials such as the steel and aluminum foil. Through the reasonable current density setting and electrolyte concentration control, it is hopeful to get the metal phosphate films on aluminum or steel.

For the amorphous  $\text{Ni}_3(\text{PO}_4)_2$  anode, the effects of thickness on electrochemical performance in lithium-ion batteries is waiting to be investigated. The sputtering Au coating has been identified that it is an available way to stabilize the capacity of  $\text{Ni}_3(\text{PO}_4)_2$  anode during cycling. Therefore, it is necessary to understand the effects of Au coating thickness on electrochemical performance in future works. The other coating materials such as Ag and Si could also be investigated. Ag and Si will reduce the cost of materials in comparison to Au. For the dip carbon nanofibers coating, the properties of  $\text{Ni}_3(\text{PO}_4)_2$  anode was not obviously improved in lithium-ion battery. However, it does not mean that the dip coating is an inappropriate method. Some materials with high cycling stability like CoO or  $\text{SiO}_2$  could be used to modify  $\text{Ni}_3(\text{PO}_4)_2$  film by dip coating. The cycling performance of  $\text{Ni}_3(\text{PO}_4)_2$  might be stabilized and increased by dip CoO and  $\text{SiO}_2$  coating. According to the current progress, the sputtering carbon coating makes  $\text{Ni}_3(\text{PO}_4)_2$  anode acquire the best electrochemical performance in lithium-ion battery with the lowest cost in comparison with other 2 methods. The effects of carbon thicknesses on cycling performance of  $\text{Ni}_3(\text{PO}_4)_2$  anodes during the charge/discharge process were recommended to be studied in future work.

Lastly, to extend the applications of PAED synthesized thin film beyond the anode materials, the PAED could be considered to synthesize cathode materials. Adding lithium acetate in Fe-containing electrolyte during PAED process is possible to obtain the  $\text{LiFePO}_4$  cathode materials. The  $\text{LiNiPO}_4$  might be synthesized by annealing the as-prepared  $\text{Ni}_3(\text{PO}_4)_2$  with  $\text{Li}_2\text{CO}_3$  powder.



## APPENDICES

### Appendix A

#### CHAPTER 4



[Home](#) [Create Account](#) [Help](#) 

 **ACS Publications**  
Most Trusted. Most Cited. Most Read.

**Title:** One-Step Fast-Synthesized  
Foamlike Amorphous Co(OH)<sub>2</sub>  
Flexible Film on Ti Foil by  
Plasma-Assisted Electrolytic  
Deposition as a Binder-Free  
Anode of a High-Capacity  
Lithium-Ion Battery  
**Author:** Tao Li, Xueyuan Nie  
**Publication:** Applied Materials  
**Publisher:** American Chemical Society  
**Date:** May 1, 2018  
Copyright © 2018, American Chemical Society

**LOGIN**  
If you're a [copyright.com](#) user, you can login to RightsLink using your copyright.com credentials. Already a RightsLink user or want to [learn more?](#)

#### PERMISSION/LICENSE IS GRANTED FOR YOUR ORDER AT NO CHARGE

This type of permission/license, instead of the standard Terms & Conditions, is sent to you because no fee is being charged for your order. Please note the following:

- Permission is granted for your request in both print and electronic formats, and translations.
- If figures and/or tables were requested, they may be adapted or used in part.
- Please print this page for your records and send a copy of it to your publisher/graduate school.
- Appropriate credit for the requested material should be given as follows: "Reprinted (adapted) with permission from (COMPLETE REFERENCE CITATION). Copyright (YEAR) American Chemical Society." Insert appropriate information in place of the capitalized words.
- One-time permission is granted only for the use specified in your request. No additional uses are granted (such as derivative works or other editions). For any other uses, please submit a new request.

[BACK](#)[CLOSE WINDOW](#)

Copyright © 2019 Copyright Clearance Center, Inc. All Rights Reserved. [Privacy statement](#). [Terms and Conditions](#).  
Comments? We would like to hear from you. E-mail us at [customercare@copyright.com](mailto:customercare@copyright.com)

## CHAPTER 5



RightsLink®

Home

Create Account

Help



**Title:** Porous Ni<sub>3</sub>(PO<sub>4</sub>)<sub>2</sub> thin film as a binder-free and low-cost anode of a high-capacity lithium-ion battery

**Author:** Tao Li,Ran Cai,Xueyuan Nie,Jimi Tjong

**Publication:** Journal of Electroanalytical Chemistry

**Publisher:** Elsevier

**Date:** 15 February 2019

© 2019 Elsevier B.V. All rights reserved.

LOGIN

If you're a [copyright.com](#) user, you can login to RightsLink using your [copyright.com](#) credentials. Already a [RightsLink](#) user or want to [learn more?](#)

Please note that, as the author of this Elsevier article, you retain the right to include it in a thesis or dissertation, provided it is not published commercially. Permission is not required, but please ensure that you reference the journal as the original source. For more information on this and on your other retained rights, please visit: <https://www.elsevier.com/about/our-business/policies/copyright#Author-rights>

BACK

CLOSE WINDOW

Copyright © 2019 [Copyright Clearance Center, Inc.](#) All Rights Reserved. [Privacy statement](#). [Terms and Conditions](#).  
Comments? We would like to hear from you. E-mail us at [customercare@copyright.com](mailto:customercare@copyright.com)

## VITA AUCTORIS

NAME:	Tao Li
PLACE OF BIRTH:	Beijing, China
YEAR OF BIRTH:	1994
EDUCATION:	Yanhua Middle School Attached to Beijing Normal University, Beijing, China, 2012
	Hunan University, B.Eng., Changsha, China, 2016
	University of Windsor, M.A.Sc., Windsor, Canada, 2019